FAST ION TRANSPORT IN THE THREE-DIMENSIONAL REVERSED-FIELD PINCH

By

Phillip Bonofiglo

A DISSERTATION SUBMITTED IN PARTIAL FULFILLMENT OF THE

REQUIREMENTS FOR THE DEGREE OF

DOCTOR OF PHILOSOPHY

(PHYSICS)

at the

UNIVERSITY OF WISCONSIN – MADISON

2019

Date of final oral examination: March 26, 2019

The dissertation is approved by the following members of the Final Oral Committee:

> Jan Egedal, Professor, Physics
>
> Jay Anderson, Senior Scientist, Physics
>
> John Sarff, Professor, Physics
>
> Cary Forest, Prager Professor of Experimental Physics, Physics
>
> Chris Hegna, Harvey D. Spangler Professor, Engineering Physics

Abstract

The reversed-field pinch can spontaneously transition from an axisymmetric magnetic topology to a 3D-helical geometry. Investigations of fast ion transport associated with energetic particle driven Alfvén instabilities, tearing mode induced stochasticity, and neoclassical effects have been performed on the Madison Symmetric Torus. STELL-GAP produced shear-Alfvén continua seeded with V3Fit 3D-equilibrium reconstructions describe the response of Alfvénic bursting activity as a direct consequence of the equilibrium change on the fast ion resonance. Far infrared interferometry resolved electron density perturbations associated with the bursts provide a spatial measurement of the mode structure and support the reconstructions. Neutron measurements confirm that the bursts produce no global resonant fast ion transport, but their disappearance at high core-resonant amplitude implies other transport mechanisms at play. Neutral particle analysis and neutron signals suggest fast ion losses at sufficient core tearing mode strength, supporting the lack of Alfvénic activity. The guiding-center code OR-BIT corroborates rapid fast ion loss times in the helical state largely as a consequence of remnant tearing modes. The resulting fast ion transport scales linearly with the core tearing mode strength which is proportional to the fast ion island width but separate from Rechester-Rosenbluth diffusion. Additionally, ORBIT simulations demonstrate little neoclassical enhancement of particle transport. While superbanana orbits may exist, the RFP's well-natured guiding-center drifts result in little radial transport. Classical orbit effects dominate the macroscopic confinement properties. The growth in the core-resonant fast ion island and the associated secondary mode overlap govern the largest transport process, leading to robust fast ion losses in the helical RFP.

Acknowledgements

One of the reasons I chose to attend the University of Wisconsin for graduate school was its large breadth of plasma physics research. Over the years, I have had the pleasure to learn from and work with a large number of experts in the field. Consequently, there are almost too many people to thank.

First and foremost, I have to thank Jay Anderson for his guidance and assistance in the completion of this dissertation. It has truly been a pleasure working with you over the years. Your optimism and passion are infectious and has made my time as a graduate student a largely positive experience.

I have to thank a myriad of faculty and research staff for their expertise and knowledge they have passed on to me over the years. Carolyn Kuranz, my undergraduate advisor, for introducing me to the field of plasma physics and encouraging me to go to graduate school. My defense committee and advisors, Jan Egedal, John Sarff, Cary Forest, and Chris Hegna, for all of their brilliant insights and feedback on my work. Abdul Almagri, Karsten McCollam, Brett Chapman, John Goetz, Mark Nornberg, Lisa Reusch, and Daniel Den Hartog for all of their diagnostic and analysis wisdom as well as introducing me to MST itself. Alex Squitieri, Paul Wilhite, and Andrey Levochkin for their computational support. Peter Weix and Steve Oliva for keeping MST and the NBI up and running relatively smoothly.

Everyone, past and present, on MST also requires many thanks. From the countless operators who sat with me in the control room to the predecessors who provided a foundation from which to build, I have enjoyed working with all of you and have learned

so much.

I owe a special thanks to Marco Gobbin for teaching me the ORBIT code which constitutes a large portion of this thesis. I loved my time in Italy and enjoyed our extensive collaboration over the years. Additionally, I need to thank Don Spong for his help in installing and running STELLGAP on our servers at MST. Your expertise has proved invaluable and provided a key result in this work.

Graduate school would not have been as enjoyable had it not been for all the other graduate students. I thank all of my friends and colleagues for their help and support both in and out of the lab and always providing a place to vent frustrations: Ethan Peterson, John Boguski, Kyle Bunkers, Steph Kubala, Emily Litchko, Zach Williams, Torrin Bechtel, Jungha Kim, Anthony Xing, Patrick Vanmeter, Takashi Nishizawa, James Duff, Eli Parke, Bill Capecchi, and others who I apologize for leaving off this list.

Lastly, I would like to thank my family for their continued support and understanding. Regardless if you understand what I do, you always support me in my endeavors and push me to do better. Thank you.

List of Figures

List of Tables

Contents

Chapter 1

Introduction

1.1 Overview

Development towards a steady-state fusion power plant requires a complete under-
standing of fast ion physics. A burning fusion plasma involves self-heating from ener-
getic particles produced from the ongoing nuclear reactions. Our knowledge of fast ion
transport and confinement in magnetically confined plasmas, however, contains gaps.
Ongoing energetic particle research involves many forms of physical processes that lack
a full comprehension, such as: MHD instabilities, wave-particle resonances, convective
and diffusive transport, and non-linearities. Common in magnetic confinement schemes
and especially relevant to this thesis, one such example is the destabilization of low fre-
quency MHD modes by nonlinear energetic particle drive.[1]. Through experimentation
and numerical computation, the fusion community seeks a set of control tools to exploit
energetic particle dynamics to establish favorable plasma conditions and reduce fast ion
transport and losses.

Fast ion interactions with three-dimensional magnetic fields have become particu-
larly relevant in a variety of fusion programs. Past studies have explored the detrimental
effects of discrete-coil-induced tokamak-field ripples and unoptimized stellarator geome-
tries on the energetic particle population.[2–8] Since then, research and understanding
of the fast ion response to the 3D topology has grown considerably. Unfavorable fast

ion transport can now be suppressed un the tokamak by employing 3D-field phase-space control.[9–12] Confinement of fast ions in stellarators is expected to drastically improve by constraining coil designs.[13–15] However, the impact of 3D-fields on fast ion phase-space, neoclassical effects, and energetic particle driven instabilities remains fully unknown. The Madison Symmetric Torus can produce reversed-field pinch, tokamak, and stellarator-like plasmas, making it a perfect test bed for fast ion physics.

This thesis examines fast ion transport physics in the Madison Symmetric Torus reversed-field pinch in a special case where the plasma develops a helical core. Extensive studies have shown that the plasma can organically transition from a 2D-axisymmetric to a 3D-helical equilibrium, greatly altering the confinement properties.[16, 17] Little attention has been placed on the fast particle content, however, equally critical for fusion. Therefore, the behavior of fast ions poses a critical question for the helical state's fusion relevance and mandates a comprehensive experimental and computational investigation. This dissertation and its associated works provide the first holistic examination of the fast ion response to the the helical reversed-field pinch.

The standard reversed-field pinch possesses favorable fast ion physics while measurements and simulations herein indicate substantial fast ion losses in the helical state. This work explains these findings in regards to various fast ion transport mechanisms. Energetic particle physics in the standard reversed-field pinch will be discussed as a comparison and to provide a complete overview. The novel works in this dissertation include:

- A comprehensive study of the fast ion confinement properties in the RFP QSH state
- Substantial experimental evidence of fast ion losses in the QSH state

- ORBIT simulations of fast ion confinement, diffusion, and phase-space consistent with experimental evidence

- STELLGAP computations that describe the frequency response of Alfvénic instabilities as a direct consequence of the evolving helical equilibrium

- FIR coherence measurements with Alfvénic instabilities that directly support the STELLGAP results

- The identification of superbanana orbits in the helical RFP and an explanation for the lack of neoclassical enhancement

In this first chapter, the basics of fusion, the reversed-field pinch, the Madison Symmetric Torus, and the helical reversed-field pinch state are presented. Chapter 2 covers the diagnostic suite employed for experimental work and introduces the various codes used for numerical studies. Chapter 3 discusses the impact of tearing modes on the fast ion phase-space and confinement. Chapter 4 presents research on the evolution of Alfvénic instabilities in the helical reversed-field pinch and their effects on the fast ion population. Chapter 5 reports on any enhancement of neoclassical transport due to the helical perturbation. Lastly, this thesis concludes with a summary of the key results and presents ideas for future work.

1.2 Fusion Energy

Nuclear fusion has been a long sought-after solution to the world's ever increasing energy demand.[18] With its foundations and basic principles dating as far back as the early 1920's, fusion quickly garnered attention as a more energetically favorable alternative to fission. Once concealed in the confidential creation and advancement of atomic weapons, nuclear fusion research has progressed greatly since the 1950's towards a more humanitarian goal of energy production.

Nuclear fusion is the reaction in which two atomic nuclei combine to form different, heavier nuclei and subatomic particles. The opposite, large nuclei splitting into lighter nuclei, is fission. In the end, the mass of the products of the reaction is smaller than the mass of the reactants for both processes. The mass difference lies in the binding energy between the nuclei.[19] The binding energy represents the energy needed to disassociate the nuclei and overcome the strong nuclear force holding them together. The basis of fusion and fission revolves around the conversion of mass to a net output of energy via Einstein's famous mass-energy equivalence: $E = mc^2$.

The key difference between fusion and fission comes from the reactant's masses. Since fusion occurs from lightweight nuclei, such as hydrogen and helium, the binding energy per nucleon is higher than that of fission, which occurs for heavy elements like uranium and plutonium. Fusion can occur for atomic nuclei up to ^{56}Fe where the binding energy per nucleon reaches a maximum on the order of MeV scales, shown in Figure 1. This allows for a large energy production among the lighter elements as they fuse
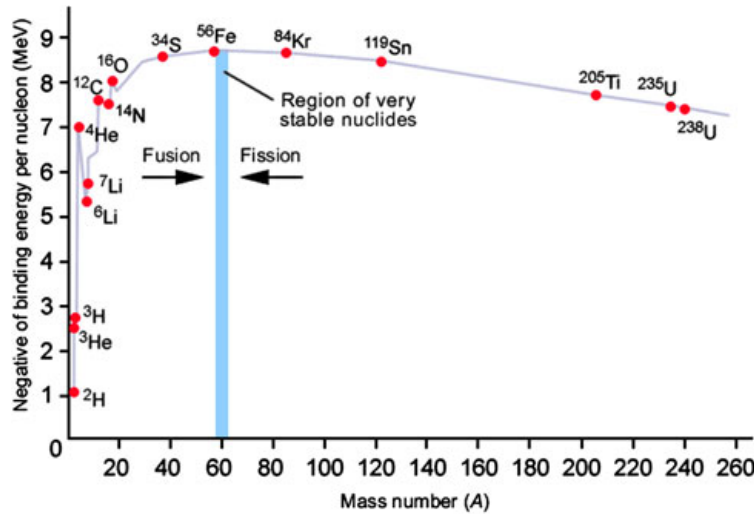
Figure 1: Binding energy per nucleon as a function of total atomic mass number with labeled fusion and fission regimes. Taken from reference [20].

to heavier nuclei and release binding energy. Beyond ^{56}Fe, fusion requires an energy input, making fission more advantageous. Fusion has become more favorable than fission since the overall energy released per atomic event is higher. Looking at Figure 1, one can see that the energy produced from fusing hydrogenic isotopes results larger energy output compared to fission events. In addition, nuclear fusion lacks the main problems of fission, namely: long-lived radioactive waste, difficulties acquiring fuel, reactor failures and meltdowns, and proliferation worries.[18] The difficulty in fusion, however, lies in the large amount of pressure and high temperatures needed for sustained reactions.

In order to realistically achieve fusion for the purposes of stable energy production, most schemes involve combining deuterium and tritium isotopes, creating the reaction shown in equation 1.1 below.

$$^{2}_{1}\text{D} + {}^{3}_{1}\text{T} \rightarrow {}^{4}_{2}\text{He}\,(3.5\,\text{MeV}) + {}^{1}_{0}\text{n}\,(14.1\,\text{MeV}) \tag{1.1}$$
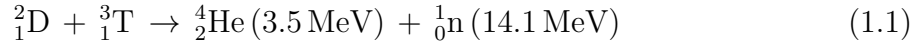
DT-fusion provides the easiest path forward for sustained fusion reactions because it requires the least extreme temperatures and pressures. One can conceptualize this physically by comparing the power produced from fusion reactions to the power lost, otherwise known as the Lawson criterion.[21] When the rate of energy production from fusion events exceeds that of environmental losses, the plasma reaches "ignition" and produces a net power output. Equation 1.2 mathematically describes this relation, where $<\sigma v>$ represents the fusion reaction rate, τ_E the energy confinement time, E_{fus} the energy of the fusion products, and n and T are the plasma density and temperature, respectively.

$$n\tau_E \geq \frac{12}{<\sigma v>}\frac{T}{E_{\text{fus}}} \tag{1.2}$$

Considering reactions of various hydrogenic isotopes, one can compose Figure 2 below. A quick inspection reveals that the DT-fusion reaction satisfies the Lawson criterion with the lowest plasma pressure and temperature, whereby density is analagous to pressure.
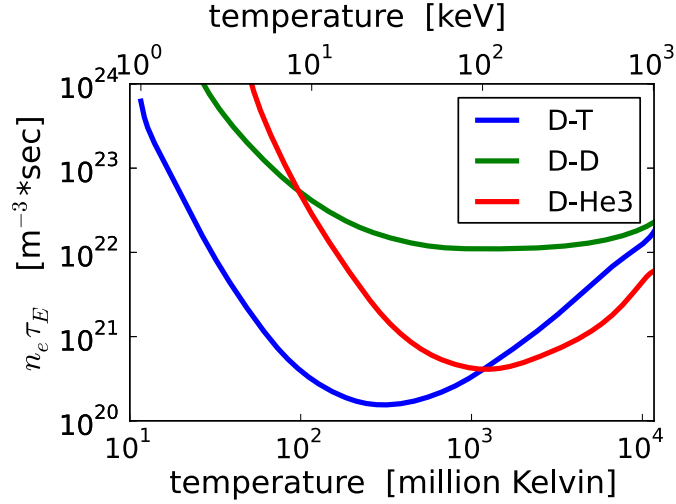
Figure 2: The Lawson Criteria - electron density $\times$ energy confinement time as a function of plasma temperature required to achieve ignition for various fusion reactions. Taken from reference [22].

Of note, the alpha particles produced in equation 1.1 form the basis for the fast ion physics discussed in this thesis. Upon "ignition," the 3.5 MeV alpha particles can "self-heat" the burning fusion plasma. That is, the energetic alpha particles can transfer their energy to the bulk, thermal plasma and drive further fusion reactions. This process forms the basis of a steady-state fusion based nuclear reactor capable of putting energy on the commercial grid. Therefore, the understanding of the confinement and transport of the energetic ion population is pivotal towards achieving a self-sustaining state.

The interior of stars, where immense amounts of gravitational pressure can compress and confine ionized nuclei to extreme pressures and temperatures, provides a natural

environment for nuclear fusion.[23, 24] On Earth, however, we do not have the advantage of millions of years of gravitational pull to compress our plasma. Two methods towards achieving sustainable fusion have primarily taken root: magnetic confinement and inertial confinement. A magnetic field can be used to confine a fusion plasma, or a ultrashort laser pulse can drive radiative compression.[25, 26] The latter is not relevant for this thesis and will not be discussed further. The most popular magnetic confinement devices include the tokamak and stellarator, of which the relevant fast ion transport physics will be discussed later. The work presented herein, however, occurred on a less-studied confinement device described in the next section.

1.3   The Reversed-Field Pinch

The reversed-field pinch (RFP) device is closest to the basic screw-pinch in terms of stability and confinement. Like most magnetic confinement devices, a RFP is a toroidal confinement device with a toroidal (B_ϕ) and poloidal (B_θ) magnetic field structure. A key feature of the RFP, however, is that almost all of the confining field is generated by electrical current flowing within the plasma as opposed to external coils. The toroidal field in a RFP reverses direction near the outer edge, lending the device its name.[27] Figure 3 depicts the RFP magnetic topology. The RFP magnetic field solution arises from energy minimization ($B^2/2\mu_0$) at a constant helicity, known as the Taylor state.[28] The Taylor state is mathematically defined in equation 1.3 in terms of Bessel functions
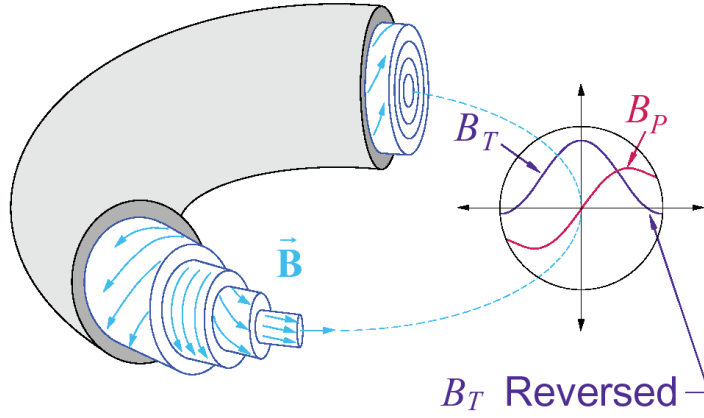
Figure 3: Representation of the RFP Magnetic Topology

where λ is a constant.

$$\vec{\nabla} \times \vec{B} = \lambda \vec{B} \tag{1.3a}$$

$$B_\phi = B_0 J_0(\lambda r), \ B_\theta = B_0 J_1(\lambda r) \tag{1.3b}$$

Equation 1.3 describes the Taylor state as a configuration in which the current is parallel to the magnetic field. For a critical value of λr, the toroidal field reverses direction near the edge. Figure 4 depicts a typical RFP equilibrium and q-profile. The q-profile, or safety factor, represents a relationship between the device geometry and the equilibrium field. The safety factor for an axisymmetric equilibrium (B_θ, B_ϕ) with geometry (r, R) is defined as:

$$q = \left\langle \frac{r B_\phi}{R B_\theta} \right\rangle \tag{1.4}$$

where $<>$ denotes an average over the flux surfaces. The safety factor provides characteristic traits of an equilibrium and takes on a unique shape for a given device. The RFP
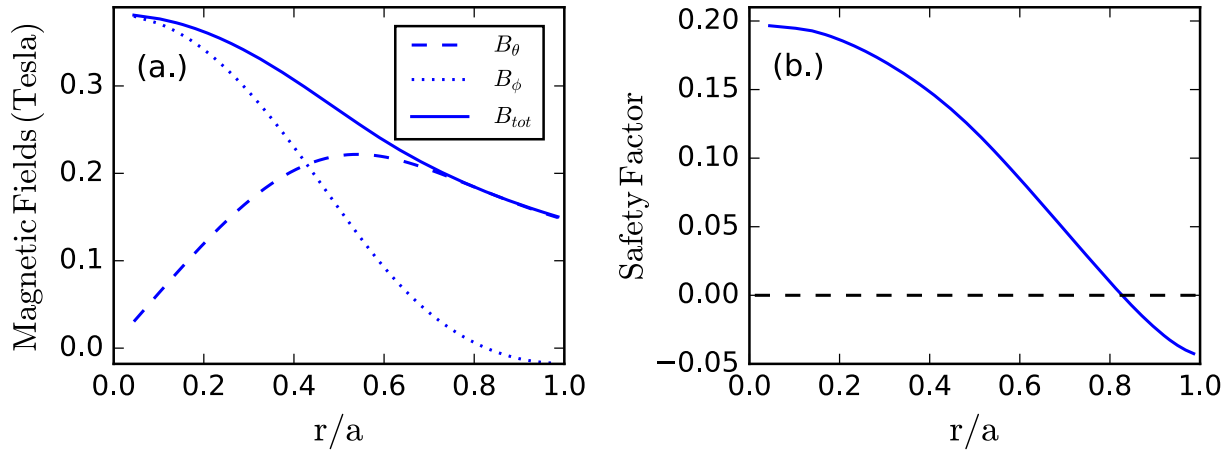
Figure 4: Equilibrium magnetic fields for a typical RFP plasma, (a.), and the corresponding q-profile, (b.).

possesses poloidal and toroidal magnetic fields of comparable amplitudes, unlike a tokamak which has a toroidal field much stronger than its poloidal component. This gives rise to a relatively low safety factor ($q < 1$) which falls to 0 as the toroidal field reverses near the plasma edge. The shape and value of the safety factor becomes particularly important when discussing resonant surfaces.

The fundamental operation of the RFP revolves around the routine relaxation of the magnetic field toward the Taylor-state equilibrium. This self-organization of the magnetic topology is commonly called the sawtooth cycle,named from the sawteeth-like shaped signals observed during the process. As a consequence of finite resistivity, magnetic field lines may tear and rejoin in a process called magnetic reconnection. The sawtooth cycle establishes itself through reconnection events driven by gradients in the parallel current density ($\vec{\nabla} J_{\parallel}$). Resonant modes in $J_{\parallel}$, known as tearing modes, induce local regions of magnetic reconnection and $\tilde{v} \times \tilde{b}$ driven electric fields that flatten out the current profile.[29] The fluctuations subside, and the gradient reestablishes itself to

start the process over again. The resonant tearing modes occur when the wave vector is perpendicular to the magnetic field ($\vec{k} \cdot \vec{B} = 0$) which leads to the relation:

$$q = \frac{m}{n} = \left\langle \frac{rB_\phi}{RB_\theta} \right\rangle \tag{1.5}$$

The variables m and n refer to the poloidal and toroidal mode numbers, respectively. The mode numbers originate from Fourier decomposing a torus along the poloidal ($\hat{\theta}$) and toroidal ($\hat{\phi}$) directions. The mode numbers take on integer values and are often presented in the form (m, n) to represent a rational surface. The RFP's safety factor results in many $m = 1$ resonances within the plasma volume and $m = 0$ resonances near the edge. Figure 5 presents a schematic representation of the typical resonance locations in the Madison Symmetric Torus (discussed in the next section) RFP.
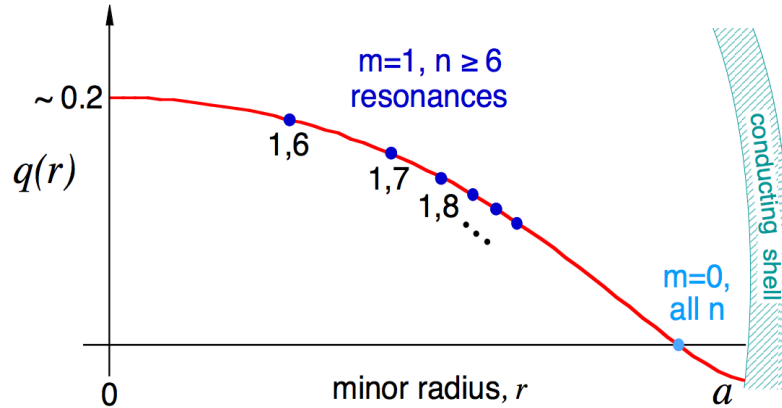
Figure 5: Typical q-profile and resonant (m,n) surfaces for the Madison Symmetric Torus RFP.

The resonant locations give rise to local reconnection events which result in the tearing and reformation of magnetic field lines. The closure of field lines creates o-points in the magnetic topology called islands. The islands have a width given by equation 1.6,

where $q' = dq/dr$, $\tilde{b}_r$ is the radial magnetic perturbation, and w_{mag} is evaluated at the rational surface location, r_s.

$$w_{\mathrm{mag}} = 4\sqrt{\left.\frac{\tilde{b}_r r}{B_\theta n |q'|}\right|_{r_s}} \qquad (1.6)$$

Depicted in Figure 6, the resonant surfaces in a RFP lie closer and closer together as q falls to zero due to the RFP's large magnetic shear. This produces significant overlap among the island boundaries and allows magnetic field lines to radially wander near the edge. This can cause drastic radial transport and losses for particles tightly bound to the field lines with substantial parallel velocity.[30] The next section introduces the machine used for this thesis and its functionality. It possesses many modes of operation which result in alterations of the q-profile and, thus, plasma performance
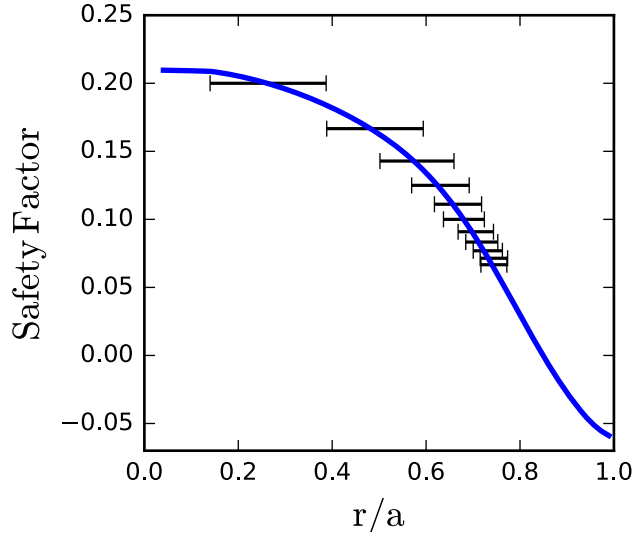
Figure 6: Representative q-profile for a RFP with $m = 1$, $n = 5 - 16$ magnetic islands. Note the significant overlap of island widths with increasing minor radius.

1.4   The Madison Symmetric Torus

The Madison Symmetric Torus (MST) is a RFP device that has been actively used to investigate fusion science since the 80's.[31] The design of MST is rather simple. Unlike a tokamak or a stellarator, the MST contains no external field coils. Instead, MST consists of a 5 cm thick aluminum shell through which currents can be driven to provide the initial magnetic field structure. The thick, conductive wall acts to stabilize MHD instabilities and balance the toroidal magnetic forces as well. The machine parameters and typical plasma values are given in Table 1.

Parameter	Denotation	Value
Major Radius	R_0	1.5 m
Minor Radius	a	0.5 m
Plasma Current	I_p	200 - 600 kA
Magnetic Field Strength	$\|B\|$	0.2 - 0.5 T
Electron Density	$\bar{n}_e$	$\sim 10^{13}$ cm^{-3}
Electron Temperature	T_e	200 - 2000 eV
Pulse Length	60 - 100 ms	
Plasma Species	Deuterium	

Table 1: MST Parameters

A transformer drives toroidal magnetic flux through a toroidal gap in the wall and provides the initial magnetic field. The toroidal magnetic field sustains itself through poloidal currents generated from the dynamo action described in the previous section. A 80-ton iron winding drives poloidal flux into the machine through a second gap poloidally cut in the wall. The MST plasma effectively acts like a single-turn secondary winding of a transformer with 20 pF windings. The poloidal field winding acts as the primary turn, and the plasma current acts as the secondary turn. The inductively driven plasma current

then produces the poloidal component of the magnetic field and ohmic heating. Figure 7 presents a CAD drawing of MST showing its conductive shell, toroidal transformer (bottom), and primary field winding.
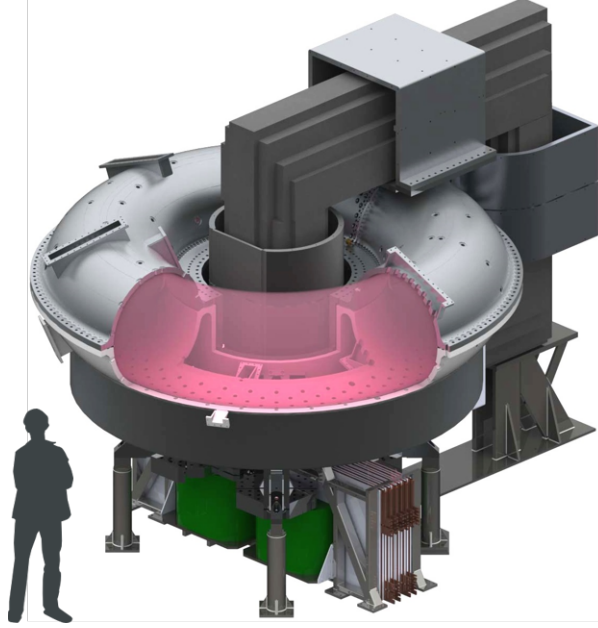
Figure 7: The Madison Symmetric Torus

MST has many modes of operation that make it unique in its study of fusion physics. Standard RFP plasmas take one of two forms: reversed or non-reversed. Reversed plasmas refer to those that naturally transition to the Taylor state and reverse B_ϕ near the edge. These plasmas possess a negative reversal parameter, $F = \frac{B_\phi(a)}{<B_\phi>}$. After reversal occurs, a crowbar bank switches in to the toroidal field circuit to further aid and sustain reversal. By leaving the toroidal field circuit open, no currents may flow and $B_\phi(a) = 0$, creating non-reversed plasmas ($F = 0$). Non-reversed plasmas force $q(a) = 0$, allowing for a $(1, 5)$ resonant surface as q shifts upward and positioning the $m = 0$ resonant surface at the conductive wall which stabilizes $m = 0$ resonant activity. This reduces nonlinear coupling between the many $m = 1$ modes in the plasma interior and $m = 0$

modes at the edge, influences sawtooth dynamics, and plays a crucial rule in establishing the helical equilibrium discussed in the next section.[32, 33]

In addition to its normal RFP operation, MST can create plasmas similar to that of tokamaks and stellarators. In recent years, programmable power supplies (PPSs) have been installed on the toroidal and poloidal field circuits of MST.[34] The PPSs provide enhanced control over existing RFP plasmas while also allowing MST to create tokamak equilibria. Digital waveforms to the PPSs grant precise control of $B_\phi(a)$ and I_p, giving way to tokamak plasmas with $q(a) < 2$ and I_p as low as 50 kA. Fast ion physics in MST tokamak plasmas remains relatively unexplored. In certain scenarios, the RFP can acquire a helical core which bears some resemblance to the stellarator but with fundamental differences, such as the q-profile shape. This dissertation focuses on the fast ion transport associated with this state; therefore, due to its relative importance, the next section is dedicated to explaining the helical RFP in detail.

1.5 Quasi-Single Helicity

The RFP provides a unique environment to study fast ion confinement and transport in both axisymmetric and helical geometries. Under proper conditions, MST equilibria have been observed to self-organize from a 2D-axisymmetric equilibrium to a 3D-helical equilibrium. RFP plasmas normally possess a broad spectrum of long wavelength tearing modes characterized mostly by the $m = 1$ poloidal mode number due to the low safety factor ($q < 1$). This standard RFP mode configuration may be called the multiple helicity (MH) state. A quasi-single helical (QSH) state forms when the MH state condenses down to a spectrum dominated by a single $m = 1$ mode like that depicted in Figure 8. The
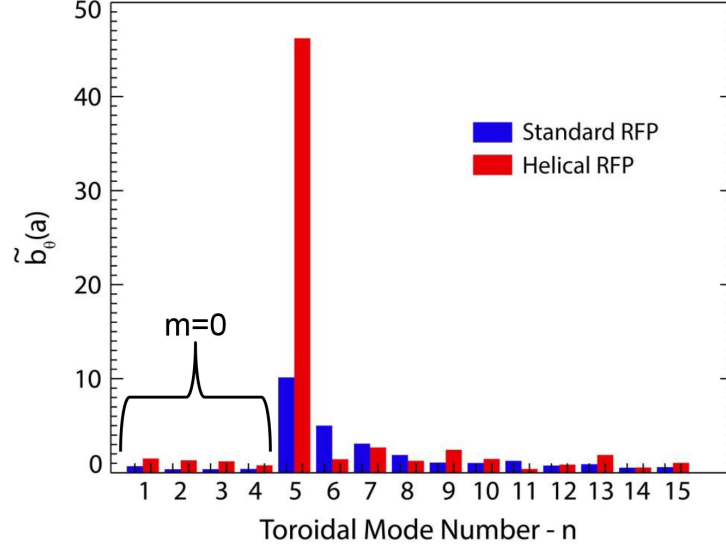
Figure 8: Spectrum of poloidal tearing mode amplitudes for $m = 0$, $n = 1 - 4$ and $m = 1$, $n = 5 - 15$ modes in a standard RFP plasma (blue) and helical RFP plasma (red).

tearing mode spectrum for a representative MH state (blue) contains $m = 1$ modes of comparable amplitudes. The QSH state (red) is dominated by a single mode ($n = 5$ in this case). The $m = 0$ modes are considerably weaker than the $m = 1$ modes because they lie near the edge of the plasma, close to the conductive boundary.

A helical axis forms when the innermost resonant tearing mode grows and envelops the magnetic axis while the subdominant modes maintain, or decrease, their amplitudes. The X-point of the dominant magnetic island merges with the standard axis, eliminating the two, and establishing a helical axis at the island's former O-point. Figure 9 represents this transition pictorially with magnetic flux surfaces. The helical core is actually very well ordered. The decoupling of the subdominant modes creates a local reduction in the magnetic stochasticity and has a substantial impact on particle confinement. Figure 10 presents magnetic Poincaré plots for MH and QSH states, reflecting the magnetic structures attributed with each state.
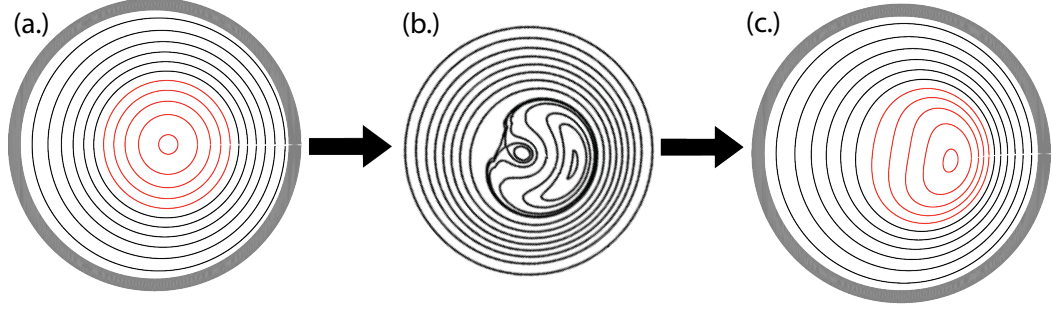
Figure 9: Magnetic flux surfaces depicting the transition from MH to QSH. An axisymmetric topology, (a.), experiences a growth in the core-resonant island until it envelops the magnetic axis, (b.), forming a helical axis at the former island O-point, (c.). See Figure 12 for a 3D rendering of the QSH flux surfaces.
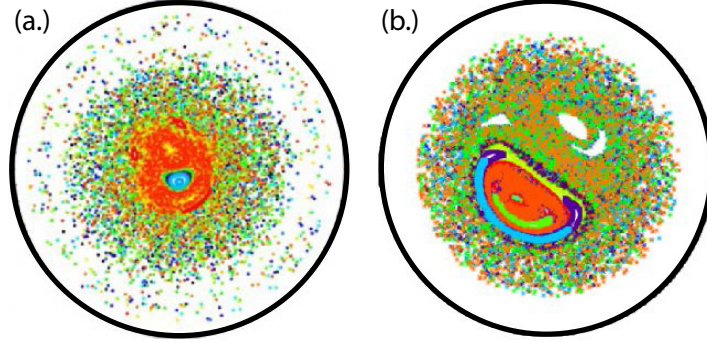
Figure 10: Magnetic Poincaré plots in a MH state, (a.), and a QSH state, (b.). Figures were taken from reference [35].

The QSH state readily presents itself in RFP plasmas but its origin and transport physics are not fully understood.[36–43] The breaking of the nonlinear coupling among the poloidal tearing modes, however, seems pivotal to the transition process.[44] In the standard RFP, the $m = 1$ tearing modes nonlinear couple through the $m = 0$ modes.[32, 33, 45] Breaking this coupling mechanism allows for the core-resonant mode to grow in amplitude without transferring its energy nonlinearly to the other $m = 1$ modes and a collapse of the mode spectrum to the single core-resonant $m = 1$ mode occurs. Mentioned previously, non-reversed plasmas in the MST most readily produce the QSH state. The

forcing of $q(a) = 0$ restricts the $m = 0$ surfaces to the edge-conducting boundary, thereby aiding in the decoupling of the $m = 1$ modes and the growth of the $(1, 5)$ mode.

Computational modeling has provided insight into this transition but experimental observations account for the bulk of our understanding.[46–48] Empirically, the likelihood of transitioning to a QSH state has been observed to increase at high Lundquist number $(S > 10^6)$ which scales as equation 1.7 in the RFP where L is the system size, v_A the Alfven velocity, and η the plasma resistivity.

$$S = \frac{L v_A}{\eta} \sim \frac{I_p T_e^{3/2}}{\sqrt{n_e}} \tag{1.7}$$

MST plasmas transition to the QSH state in non-reversed discharges $(q(a) = 0)$ at modest I_p $(> 350\,\text{kA})$ and low density $(\bar{n}_e < 0.5 \times 10^{13}\ \text{cm}^{-3})$ with $m = 1$, $n = 5$ as the dominant perturbation. This means a 5-fold toroidal periodicity defines the helical equilbrium. The spectral index, N_s, provides a useful parameter to help identify this state, where $\tilde{b}_n$ denotes the tearing mode amplitudes and $N_s \lesssim 1.2$ represents the QSH state.

$$N_s = \left[\sum_n \left(\frac{\tilde{b}_n^2}{\sum_n \tilde{b}_n^2} \right)^2 \right]^{-1} \tag{1.8}$$

Depending on plasma conditions, QSH plasmas in MST saturate at $\frac{\tilde{b}_5}{|B(a)|} \sim 5 - 8\%$ with subdominant tearing mode amplitudes in total around 0.5-2%. Figure 11 shows the tearing mode amplitudes for a typical QSH discharge in MST. The divergence of the $n = 5$ tearing from the other mode amplitudes is the formation of the QSH state. One may note that the plasma crashes out of the QSH state back to the MH state around 33 ms before the $n = 5$ tearing mode climbs back up in amplitude. The QSH
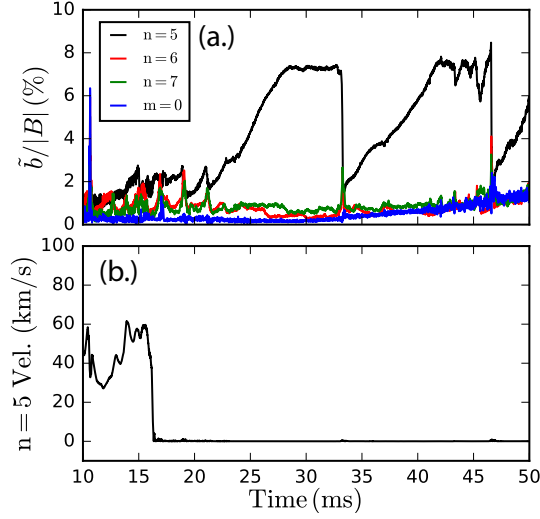
Figure 11: Example of QSH magnetic signals showing the dominant $(1,5)$ and subdominant $(0,4)$, $(1,6)$, and $(1,7)$ tearing mode amplitudes, (a.), and the $(1,5)$ mode velocity, (b.). The marked growth in the $n = 5$ mode corresponds to the QSH transition.

rise time, saturation, and crashes vary shot to shot and may greatly depend on machine conditioning for the run day. From an operational standpoint, we have little control over the QSH transition in MST. The machine operator can make conditions favorable where the natural transition occurs more frequently (i.e. non-reversed discharge, low gas puffing, applying resonant magnetic perturbations), but the exact control of the tearing modes is impossible.

Looking at Figure 11, the $n = 5$ velocity drops, and remains, at zero just as the $n = 5$ amplitude begins to rise. The growth in the $n = 5$ perturbation drives eddy currents in the shell which create their own magnetic perturbation at the mode resonance. This induces a torque against the mode rotation and slows the plasma.[49] The imposed torque will reduce until torques from error fields become the dominant force at which point the plasma will lock to the error field.[50] Although many error fields exist, QSH plasmas have preferential locking phases. An error field correction system may be used

to externally control the error field coupling and QSH phase locking.
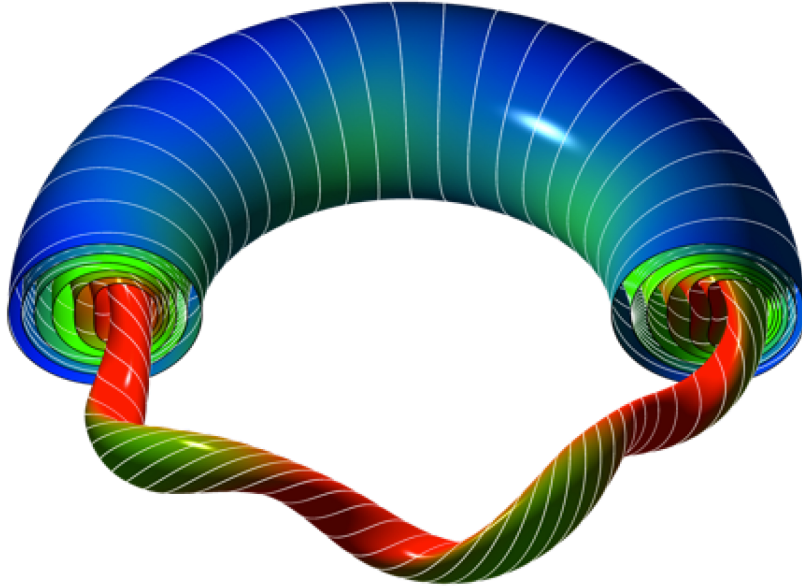
Figure 12: A 3D rendering of the QSH state flux surfaces.

Chapter 2

Experimental and Computational Tools

2.1   Diagnostics

In this next section, key diagnostics used in this work will be introduced. While only those relevant to this thesis are presented, MST maintains a large diagnostic suite, including: soft x-ray tomography, charge-exchange and Doppler spectroscopy, Thomson scattering, and various insertable probes.

Mirnov Coils

Commonly referred to as the edge coils, MST contains multiple arrays of Mirnov coils, one toroidal and three poloidal. Time varying magnetic fluctuations, $\tilde{b}$, will induce small measurable voltages in the coils via Faraday's law of induction. The number of coil turns, effective coil area, and integrating circuit determine the calibration, and the amplitude of the magnetic fluctuation is measured. The edge coils consist of sets of three orthogonal coils at each location so that $\tilde{b}_r$, $\tilde{b}_\theta$, and $\tilde{b}_\phi$ amplitudes can be simultaneously measured.

With an array of coils distributed toroidally around the edge of the machine, one can perform a spatial Fourier decomposition on the measured magnetic flucuations.[51] That is, for a given component (r, θ, or ϕ) the measured amplitude can be expressed in

series form shown in equation 2.1. In this work, the relevant fluctuations are captured in the toroidal array, and n corresponds to the toroidal mode number. With $N_{coils} = 64$ measurements, the mode amplitude, c_n, and mode phase. δ_n, can be determined for $N_{coils}/2 = 32$ modes.

$$\tilde{b} = \sum_{n=0}^{N_{coils}} c_n cos(n\phi - \delta_n) \tag{2.1}$$

The spatial decomposition provides a critical analysis tool by providing mode amplitudes, phases, and velocities. Similarly, the poloidal array is composed of 16 coils at fixed toroidal angle and gives poloidal mode number information. In practice, however, the q-profile shape and resulting resonances only make the $m = 0, 1$ and $n = 1 - 12$ modes of relevant importance.

Resonant Magnetic Perturbations

Resonant magnetic perturbations (RMPs) provide a useful tool when studying QSH plasmas and have garnered increasing use in tokamaks and stellarators, as well.[10–12] In the context of MST QSH plasmas, RMPs allow for phase control of the helical state which can aid in diagnostic capabilities.[35, 52] For example, the helical core can be locked across the Thomson scattering viewing chord or charge-exchange recombination spectroscopy lines of sight.

The poloidal gap in MST's thick conducting shell (through which flux is injected for plasma sustainment) permits localized radial magnetic fields. To combat this radial-field error, a system of 32 saddle pick-up coils and 38 correction coils are installed around the poloidal gap as shown in Figure 13. An active-feedback system between the pick-up coils and sensing coils counteracts the field error in real time, minimizing any radial field

effects.
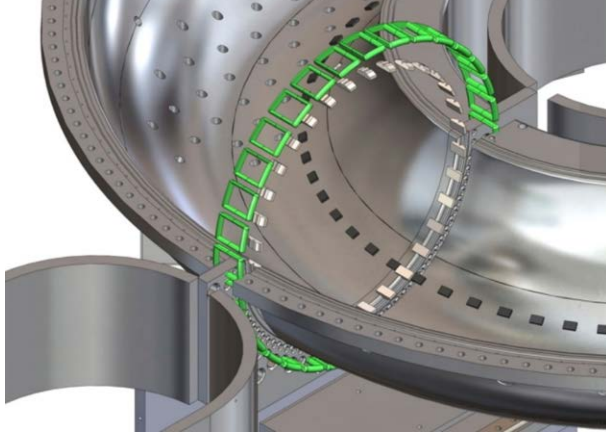
Figure 13: CAD drawing depicting the saddle pick-up coils (green) and error correction coils (white) used for RMP control at the poloidal gap in MST.

Alternatively, the feedback system can be used to generate a prescribed field error. The growth in the core-resonant tearing mode causes QSH plasmas to lock to the radial-field errors produced from the poloidal gap. Using the active feedback correction system, a radial field distribution can be created with a pre-selected mode spectrum. Since the coils are poloidally localized, the n spectrum is broad but will be dominant at the resonant modes. Applying an $m = 1$ RMP will, therefore, act strongest on the core-resonant mode and allow for poloidal control of its phase. The applied waveform consists of $m = 1$ sine (s) and cosine (c) components, so the desired locking phase is simply $\delta = \arctan(s/c)$. Adjusting the amplitude of the sine and cosine components allows control of the QSH phase from 0 - 2π radians. Setting the phase at the toroidal RMP location, the $m = 1$, $n = 5$ periodicity can be followed around the device to map the helical phase at any toroidal coordinate. This control tool is helpful in obtaining full diagnostic coverage for 3D-equilibrium reconstruction and for positioning the helical plasma for experiments with neutral beam injection.

Advanced Neutral Particle Analyzer

The advanced neutral particle analyzer (ANPA) on MST measures the fast ion energy distribution by detecting fast neutrals created when fast ions charge exchange with background neutrals and exit the machine uninhibited.[53] Fast neutrals that lie within the viewing angle of the ANPA will be stripped by a 10 nm, biased, carbon foil. The now-stripped ions pass through an electrostatic lens for focusing, followed by a permanent magnetic field to separate the ions by energy, and an electric field to separate the particles by mass. Twenty detectors (10 each for hydrogen and deuterium) measure particles with energies between 8 - 40 keV.[54] Figure 14 presents a schematic of the ANPA and its key components.
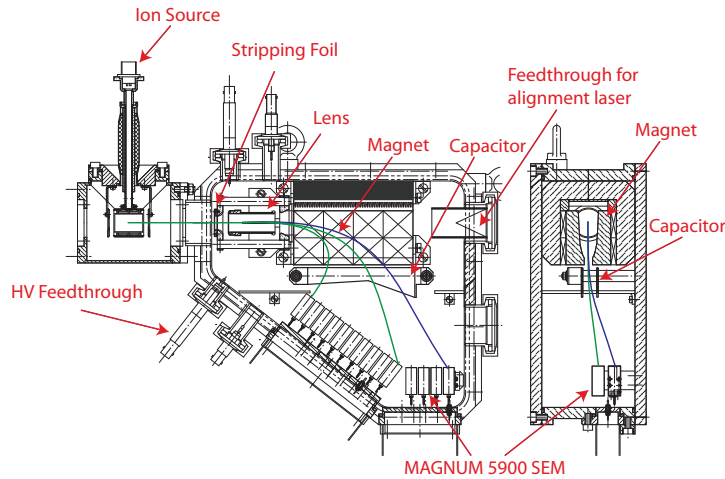
Figure 14: Schematic of the ANPA and its key components.

The ANPA measured particle flux, Γ_{ANPA}, in equation 2.2 is a line average signal across the sight line, L, that depends on the neutral density, n_0, fast ion density, n_{fi}, the charge-exchange reaction rate, $< \sigma v >_{cx}$, reionization fraction, f_r, and particle pitch,

$$\gamma = \frac{v_\parallel}{v}.$$

$$\Gamma_{\text{ANPA}} = \int_L n_0 n_{fi} <\sigma v>_{cx} \delta(\gamma - \gamma_c)(1 - f_r)dl d\gamma \tag{2.2}$$

Of note, the signal is highly dependent on a critical pitch, γ_c, defined by the ANPA viewing chord and magnetic topology. Equilibrium reconstructions can find the parameters f_r and γ_c while D_α-emission measurements constrain n_0 via equation 2.3.

$$\gamma_{D_\alpha} = n_e n_0 <\sigma v>_{excitation} \tag{2.3}$$

D_α emission occurs when excited neutral deuterium relaxes to a lower energy state and emits a photon. The neutral density may then be found from the recorded photon signal, γ_{D_α}, electron density, n_e, found from a standard CO2 interferometer, and the excitation reaction rate, $<\sigma v>_{excitation}$.

The ANPA views either a "radial" or "tangential" view based on how it is mounted to MST. The "radial view" will look across a poloidal cut of the machine, making the ANPA sensitive to fast ions with a perpendicular pitch. The "tangential view" toroidally spans the core and edges of the machine and will, therefore, be sensitive to a combination of both high-pitch and low-pitch fast ions at differing positions along the chord. Since the ANPA signal is a line-integrated measurement and highly pitch dependent, the interpretation of the signal can be quite difficult. Without ab absolute calibration, the ANPA is most useful in detecting changes in the fast ion distribution.

Neutron Detectors

Neutrons in MST originate from beam-born deuterium ions fusing with background plasma deuterons. The DD-fusion events result in two possible reactions, shown in equations 2.4, with equal probability and half of the reactions produce a 2.45 MeV neutron.

$$_1^2\mathrm{D} + {}_1^2\mathrm{D} \rightarrow {}_1^3\mathrm{T}\,(1.01\,\mathrm{MeV}) + {}_1^1\mathrm{p}\,(3.01\,\mathrm{MeV}) \qquad 50\% \qquad (2.4\mathrm{a})$$

$$_1^2\mathrm{D} + {}_1^2\mathrm{D} \rightarrow {}_2^3\mathrm{He}\,(0.82\,\mathrm{MeV}) + {}_0^1\mathrm{n}\,(2.45\,\mathrm{MeV}) \qquad 50\% \qquad (2.4\mathrm{b})$$
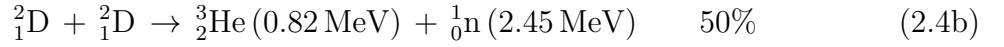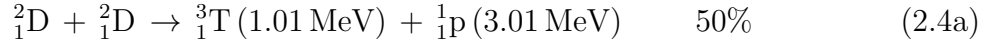
The 1 MeV triton in equation 2.4a is promptly lost, so the rate of 14.4 MeV DT neutrons is negligible. The isotropically produced neutrons freely exit MST for detection. The total neutron flux is given by the integral equation 2.5:

$$\Gamma_{\mathrm{neut}}(t) = \int n_{fi}(t)n_D(t) < \sigma_{DD}(E_{fi}(t))v_{fi}(t) > dV \qquad (2.5)$$

where n_{fi} is the fast ion density, n_D is the thermal deuteron density, σ_{DD} is the DD-fusion cross-section which is a function of the fast ion energy, E_{fi}, and v_{fi} is the fast ion velocity.[55]

MST has two scintillator-PMT neutron detectors to measure the global neutron flux.[56] A neutron entering the scintillator may impart some of its energy by colliding with the scintillator nuclei. The nuclei recoil and transfer the energy to the surrounding scintillator material, exciting fluorescent molecules and emitting photons. A photomultiplier collects the light and turns it into an electrical signal which is amplified for measurement. Fast neutrons more favorably scatter off of hydrogen nuclei, so the detectors

use plastic scintillators and have two different sensitivities. The larger scintillator size and operational voltage of the PMT make one detector more sensitive to the 2.45 MeV neutron's mean-free path and was used for all neutron measurements presented in this thesis. Both detectors are covered with thin metal shielding to protect against magnetic fluctuations, a $\frac{1}{4}$" steel enclosure for electrostatic shielding, and 4" of lead for gamma radiation shielding. The detectors lie several feet outside the vacuum vessel with a large viewing angle and measure a neutron flux proportional to the total volume-integrated fusion rate.

Far-Infrared Interferometry

The far-infrared (FIR) laser system on MST can perform interferometry or polarimetry measurements, either individually or simultaneously.[57] The system consists of 11 vertical viewing chords that record measurements continuously throughout a shot at radial locations spread roughly 8 cm apart from 1.1 m to 1.9 m in major radius. The interferometer was solely used in this thesis to measure line integrated equilibrium and fluctuation density.

Interferometry works on the fundamental principle that light travels at different speeds in different indices of refraction.[58] For a plasma, the index of refraction is related to the electron density by $n^2 \sim 1 - \frac{\omega_{pe}^2}{\omega^2}$ where $\omega_{pe}^2 = \frac{n_e e^2}{m_e \epsilon_0}$ is the plasma frequency. The relative phase shift between a probing beam and a reference beam through vacuum, defined in equation 2.6 where λ is the laser wavelength and c is the speed of light in

vacuum, yields the line-integrated electron density.

$$\Phi = \frac{-\lambda e^2}{4\pi m_e \epsilon_0 c^2} \int n_e(r)dz \qquad (2.6)$$

The radial profile, $n_e(r)$, may be obtained by Abel inversion on the line-integrated value above.[59]
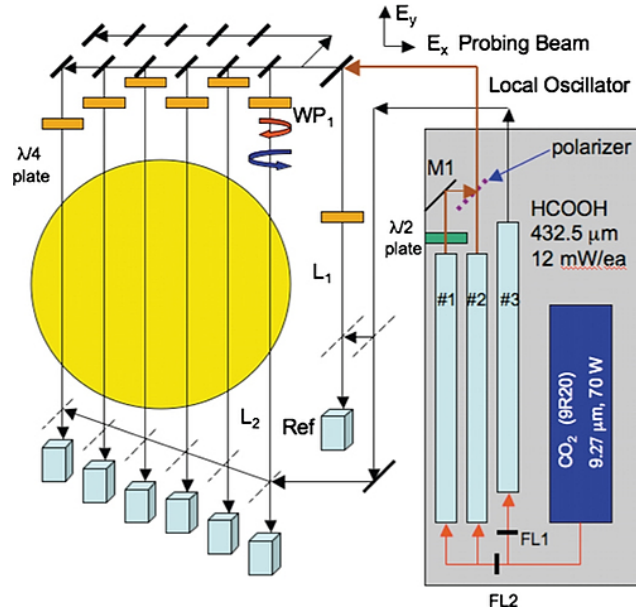
Figure 15: Schematic of the FIR interferometer-polarimeter system on MST.

Density fluctuations provide essential information about the spatial distribution of fast ion driven instabilities and are used heavily in this thesis. The time resolution of the diagnostic is $\sim$1 MHz, very adequate for the energetic-ion-driven fluctuations of modest frequency $\sim$60-200 kHz.[60]

Fast Ion Loss Detector

A fast ion loss detector (FILD) for the RFP is unique in providing a direct measure of fast ion orbit losses. This can be quite useful in the study of equilibrium and fluctuation driven losses and complements indirect measures through ANPA signal and neutron flux reductions. FILDs are widely used in fast ion physics research in both stellarators and tokamaks, though challenges presented by the RFP geometry and its close-fitting conducting shell require refinements in both detector design and signal interpretation.[61–65] This section describes the first successful FILD implemented in the RFP geometry.[66] The short distance between the last closed flux surface and conducting shell combined with localized magnetic field errors in portholes mandated an insertable probe that detects fast ions in their Larmor orbit prior to loss on the outboard limiter of MST.

In MST, the distance from the wall to the last closed flux surface is ∼1 cm. Therefore, to minimize plasma perturbation, a compact, probe-like design capable of being inserted through one of MST's standard 40 mm portholes was utilized. The probe can be fully retracted from the plasma and is capable of being rotated a full 360° along its axis. The FILD was toroidally displaced 180° from the neutral beam so as to not be sensitive to prompt losses.

A Faraday cup type design capable of measuring high-pitch fast ions in MST allowed for the simplest functionality while meeting measurement limitations. It consists of two 5 μm thick Ni foils that act as current collectors for the fast ions. The FILD is inserted ∼3-4 cm past the wall, so only ions at the "top" of their helical trajectory heading "down" may pass through the 3 mm circular aperture and be captured. The aperture size, depth, and plate locations are such that only particles with a pitch of 0.8-0.95

are collected. Figure 16 gives a representation of how the FILD functions. A grounded aluminum shell, to eliminate electrostatic coupling to the plasma, and a boron-nitride shielding, to provide thermal protection, house the foils in a cylindrical probe end.
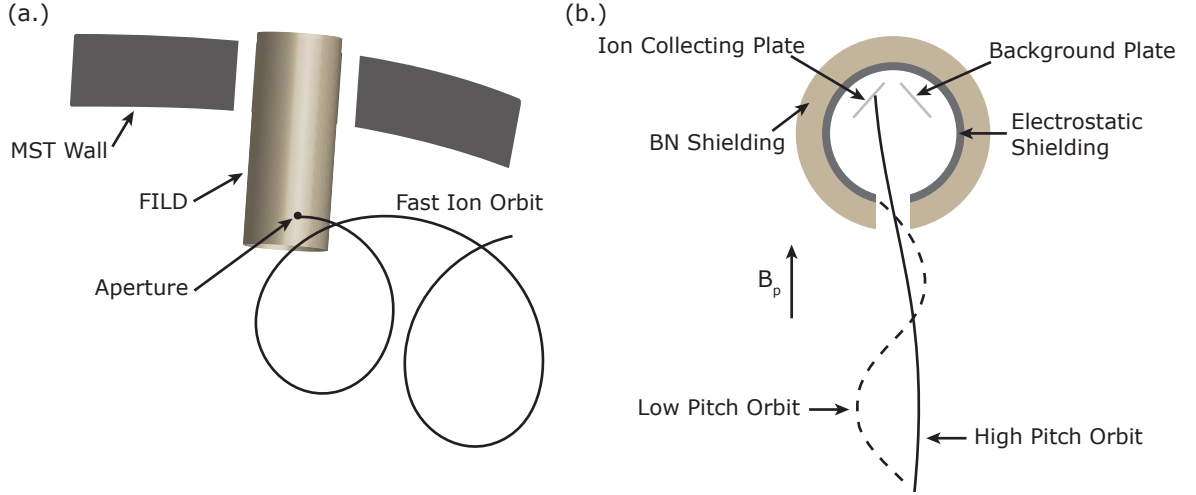
Figure 16: Representative schematic of the high-pitch FILD. (a.) Poloidal crosscut view of the FILD through a MST porthole and an arbitrary fast ion orbit. (b.) Top view along the axis of the FILD showing a rejected low-pitch orbit, an accepted high-pitch orbit, and the symmetrical plate design. Taken from reference [66].

By design, one of the collecting plates remains inaccessible to possible fast ion orbits and, therefore, measures only background noise. Assuming both collecting plates have equal background contributions, a differential amplifier removes the pure background signal from the combined fast ion and background signal. An angular scan of the FILD found that the optimal operating point exists when the aperture aligns with the edge magnetic field-line pitch, $\frac{B_\phi(a)}{B_\theta(a)}$, shown in Figure 17.

Collected electrons appear to dominate the background signal based on the observation that the ideal orientation of the probe lies along the magnetic field pitch. The FILD has an aperture size of 3 mm, allowing electrons tightly tied to the field lines
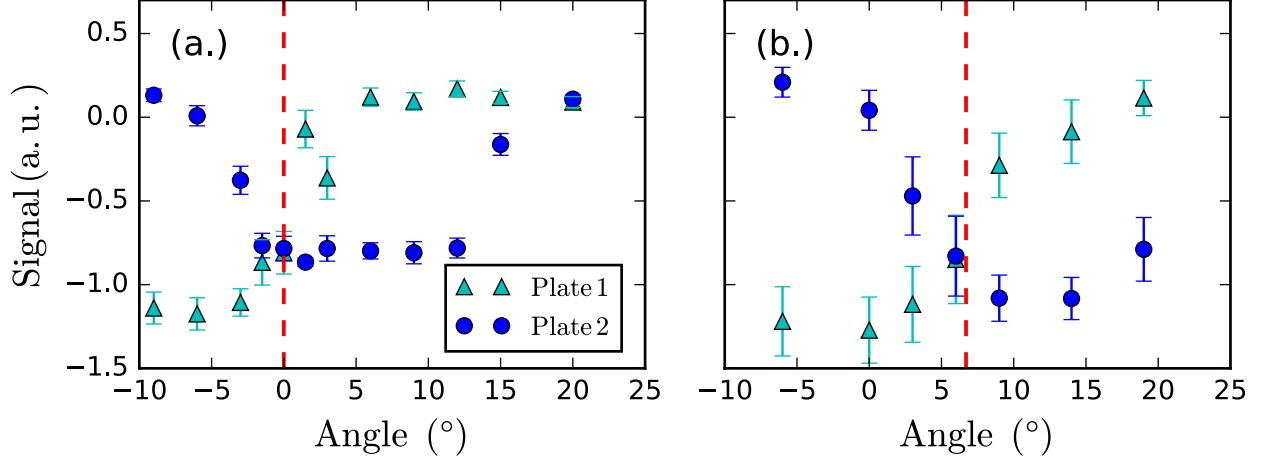
Figure 17: Rotational scan of the FILD probe as a function of angle relative to the poloidal cross-section: (a.) $F = 0$ plasma (b.) $F = -0.2$ plasma. The dashed vertical lines denote the equilibrium magnetic field line pitch at the wall. Taken from reference [66].

(gyroradius < 1 mm) to enter. Resistive tearing modes and porthole field error, however, result in a not well known edge magnetic field and electron response. Additionally, negative voltage measurements provide further indication of captured electrons. Overall, several possible contributors to the background noise exist: electron collection due to parallel motion along fluctuating field lines, photoelectric effect, and/or secondary electron emission from direct impact.

The FILD provides evidence of the strong fast ion confinement in standard RFP plasmas. The FILD detects pitch-sensitive fast ions near the wall of MST. The FILD was rotated to the magnetic field line pitch and data was recorded in $F = -0.2$ plasmas with full power hydrogen fueled NBI. The neutral beam was alternated every other shot so that a comparison between FILD signals could be made. Measurements in standard RFP discharges with and without significant fast ion populations revealed a noticeable

difference between the signals during the duration of fast particle injection. The results are shown in Figure 18. A noticeable difference is discernible between the "NBI" and
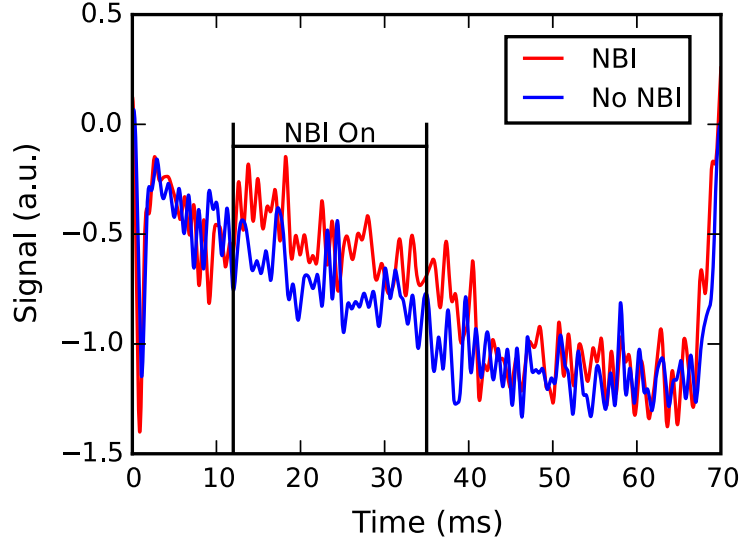
Figure 18: Shot ensembled FILD signal with and without NBI in standard RFP plasmas. The area denoted by the vertical bars is the time frame in which the neutral beam is fired. Taken from reference [66].

"No NBI" signals during the duration of the neutral beam. Changes in ambient plasma parameters and fast electrons were ruled out as sources for this change by examining n_e, bolometer, and soft x-ray signals. Past work has also confirmed that NBI has little to no effect on the electron population.[67] The NBI signal persists after the duration of the neutral beam due to the well confined nature of fast ions in MST. While the observed difference between "NBI" and "No NBI" signals is noticeable, the overall signal gain could be much larger. In addition, these results have been smoothed over to less than 1 kHz using fast Fourier transforms in order to highlight the difference between each case. The recorded fast ion loss signal just surpasses the electron noise.

Assuming the 40 kA of neutrals injected into the MST are fully converted into 40 kA of ions and that all of the fast ions are eventually lost uniformly over the surface of MST, then a 3 mm aperture should collect about 9 μA of lost fast ion current. Our difference in FILD signal between the two datasets is of order 100 mV, so a 10^6 V/A amplifier gain corresponds to 0.1 μA of current collected or about 1% of the total expected lost fast ion current. One certainly cannot expect to collect all 9 μA, and a substantial number of lost fast ions may charge exchange with neutrals near the wall to further lessen the signal. Concerning the well-confined nature of the fast ions, the measurement appears to be on the order of the expected fast ion density current to the edge. All in all, the relative amplitude of the FILD signal demonstrates that the overwhelming majority of beam-born ions remain confined to the plasma and avoid detection.

Irnoically, the novel FILD data are not used in the primary analysis herein: the most interesting energetic ion physics in this thesis are accessible only with a transition to the QSH state which occurs in high current, low density discharges with parameters not conducive to edge probing. The FILD is successful in lower current discharges where edge probes have a finite lifetime and where some residual impurity sourcing does not destroy the target plasma conditions. The FILD for the RFP will benefit from a continued development effort, including a better understanding and mitigation of electron background signal. This remains a future experimental goal.

2.2   Neutral Beam Injection

In order to study the physics that may become important with a high fast ion concentration in a burning fusion plasma, fast ions must be externally injected into today's

experiments. The two most common methods are external heating through electromagnetic wave coupling and particle beams. Electromagnetic wave cutoffs in the plasma make the heating of core ions difficult.[68] The complex magnetic fields of fusion devices make the direct sourcing of fast ions a challenge as well. Neutral particle beams have become one of the preferred methods for fast ion production in fusion research.

Neutral beam injection (NBI) provides auxiliary heating to MST and acts as a source of fast ions. The NBI operating parameters may be found in Table 2, and the NBI is shown in Figure 19. The NBI functions much like any other particle beam.[69] Arc
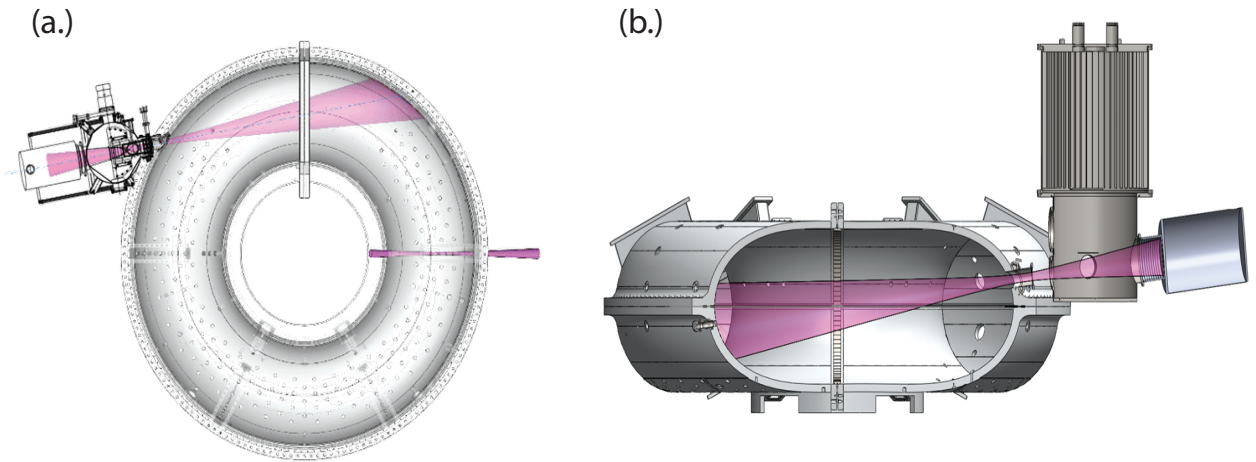
Figure 19: CAD renderings of the neutral beam injector on MST with beam path highlighted in purple for an above view, (a.), and side view, (b.).

discharges create a small ionized plasma of a chosen working gas. High voltage grids and permanent magnets then accelerate and focus the ions into a beam. The beam passes through a chamber of neutral gas where the now fast ions charge-exchange with the neutrals, producing a beam of high energy neutrals. The fast neutrals continue, unimpeded by electric and magnetic fields, into the plasma where they charge-exchange,

yet again, with thermal ions and produce fast ions in the plasma. To be more precise, the injected neutrals can produce fast ions via ion charge-exchange, ion impact, or electron impact, but ion charge-exchange dominates the interactions in MST.[67, 69]

Parameter	Value
Energy	10 - 25 keV
Maximum Power	1 MW
Pulse Length	20 ms
Composition	95% H, 5% D or 100% D
Energy Fraction (E:E/2:E/3:E/18)	86%:10%:2%:2%

Table 2: MST's NBI Parameters

Of particular importance, the choice of beam fuel (hydrogen, deuterium, or 50/50 mix) has substantial effects on the fast ion physics. Namely, the mass difference between ion species produces considerable differences in ion velocity, leading to different resonances with the plasmas MHD activity. Deuterium fast ions can easily be used to track the fast ion population through the fusion-produced neutron flux. Depending on the experimental goal, the desire for a certain beam fuel may exist.

The NBI has a tangential injection geometry, depositing most of the fast ions in the core of the plasma with high pitch, $\frac{v_\parallel}{v}$, where direction is respect to the magnetic field. Figure 20 provides an illustration of the NBI guiding-center deposition across MST. Around 90% of injected neutrals convert to fast ions with little prompt losses. Typically, the NBI operates at full power, injecting 25 keV hydrogen or deuterium ions into MST near the plasma core. The plasma density profile combined with the good confinement of fast ions in the standard RFP creates a distribution of fast ions peaked at the core. The
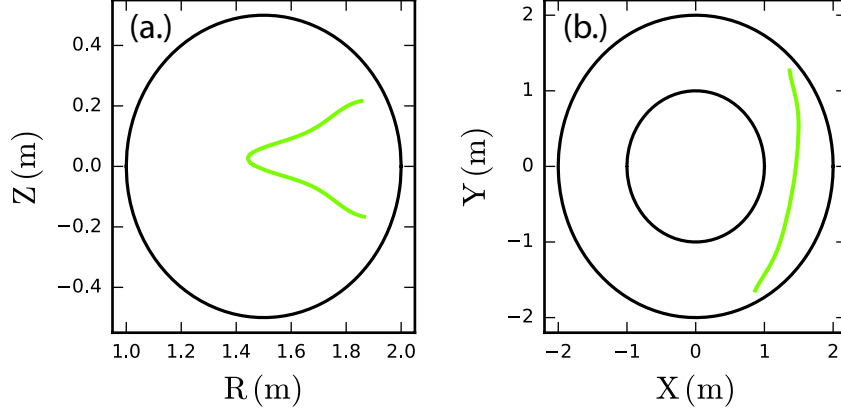
Figure 20: The line-of-sight fast ion guiding-center deposition (green) for the MST NBI in the poloidal plane, (a.), and toroidal plane, (b.).

particle transport code TRANSP has modeled the NBI deposition and produced the fast ion profile shown in Figure 21.[70–72] The TRANSP modeling only considers classical transport and does not accommodate for any re-distribution associated with anomalous or resonant transport discussed later. The TRANSP results depict a core-localized, high pitch, super Alfvénic population consistent with expectations.
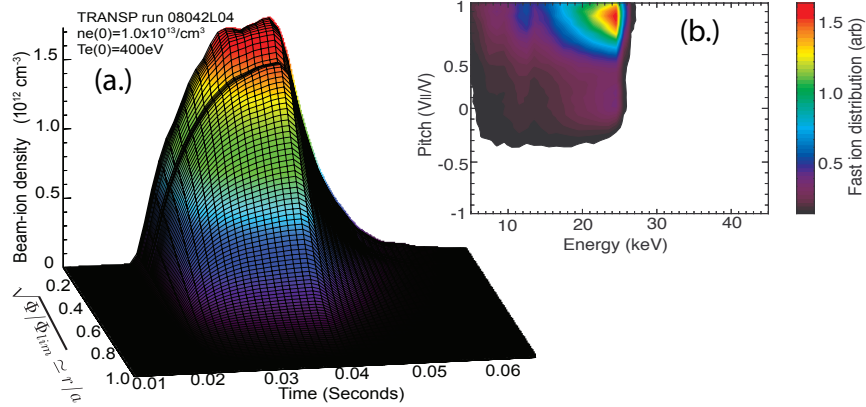
Figure 21: A TRANSP simulation showing initial localized core deposition, (a.), and pitch and energy distribution, (b.) of injected fast ions during the beam pulse ($\sim$20-40 ms). Taken from reference [70].

The MST and NBI act as a test bed for fusion relevant fast ion physics. Shown in Table 3, the MST and NBI produce fast ion parameters of relevant scales to a hypothetical RFP fusion reactor.[73] The fast ions in MST are super-Alfvénic ($v_{fi} > v_A$), have suffi-

Parameter	MST	RFP Fusion Reactor
R (m)	1.5	4.9
I_p (MA)	0.5	18
B (T)	0.5	9
T_i (keV)	0.3	10
n_e (10^{19}m^{-3})	1.0	30
ρ_{fi}/a	~ 0.1	~ 0.07
v_{fi}/v_{th}	$\sim 5\text{-}10$	~ 13
v_{fi}/v_A	$\sim 0.7\text{-}1.25$	~ 7
n_{fi}/n_e	5%	1%
β_{fi}	2%	1-2%

Table 3: Comparison of Fast Ion Parameters for MST and a Hypothetical RFP Fusion Reactor. The RFP reactor values were taken from refernce [73].

cient pressure ($\beta_{fi} = \frac{p_{fi}}{p_{mag}}$), and are of relevant energy when compared to the thermal population. The relative difference in v_{fi}/v_A arises from the much larger alpha particle energy (3.5 MeV) relative to the field strength in the RFP reactor (9 T) compared to the 25 keV beam ions in MST (0.5 T). Due to the fixed directionality of the NBI in the MST, the fast ion distribution is skewed toward the high-pitch portion of the isotropic alpha distribution in a hypothetical reactor. Figure 22 illustrates this localization. The high-pitch of the NBI born ions determines what orbits they follow. This can have a significant impact on the transport physics. Combining the many operating regimes of MST with the NBI, MST provides the opportunity to examine energetic particle physics across many fusion scenarios.
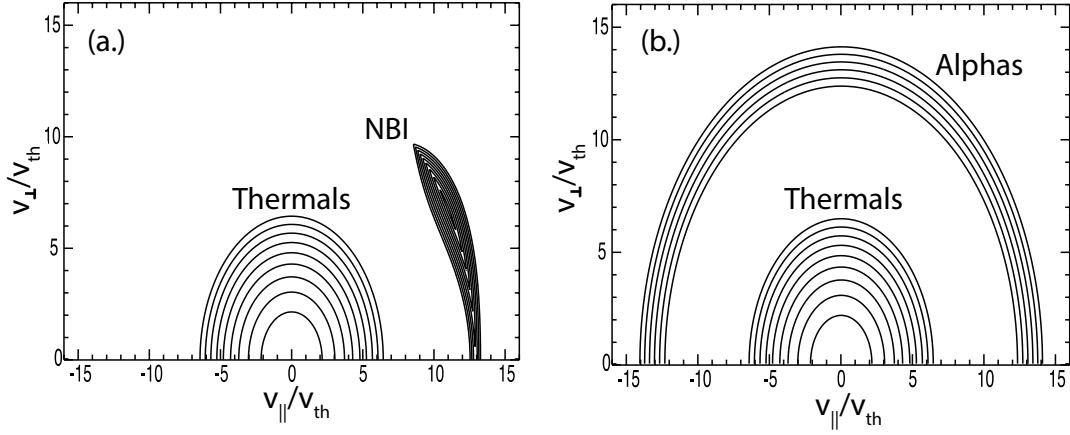
Figure 22: Velocity distributions for the initial NBI deposition, (a.), and the hypothetical alpha population in a RFP fusion reactor based on the values in reference [73], (b.).

2.3 The Beam-Blip Technique

The beam-blip technique is an experimental method that provides an estimate of the fast ion confinement time from the neutron flux produced from short pulses of deuterium fueled NBI.[74] The short time period of the NBI ensures a sufficient test population of fast ions to produce DD-fusion neutrons while avoiding any detrimental effects of energetic particle induced instabilities. Upon termination of the NBI, the fast ion confinement time can be inferred from the decaying neutron flux. The measured neutron flux strongly depends on two physical properties: the fast ion confinement which sets the accumulated total fast ion density (n_{fi}) and the fast ion slowing through the rapidly changing fusion cross-section as a function of deuteron energy ($< \sigma_{DD}(E_{fi}(t))v_{fi}(t) >$). The decay rate of the measured neutron flux, τ_{meas}, should approximately follow as:

$$\frac{1}{\tau_{meas}} \approx \frac{1}{\tau_{fi}} + \frac{1}{\tau_{slow}}$$

(2.7)

where τ_{fi} is the fast ion loss time and τ_{slow} is the classical slowing time of the fast ions.[75] Therefore, by measuring the decay in the global neutron flux and plasma parameters needed to compute classical slowing upon beam turn off, the fast ion confinement time is determined.

The neutron signal beyond the beam cutoff provides a direct point to the confinement nature of the fast ions. In MST, the beam-blip technique is performed by firing the deuterium fueled NBI for approximately 5 ms, establishing a fast ion population sufficient for neutron production without driving energetic particle instabilities. Upon termination of the neutral beam, the beam-born fast ions experience only effects associated with the magnetic topology and collisions. Using Thomson scattering to measure the electron temperature, interferometry to find the electron density, and the beam parameters, the classical fast ion slowing time can be calculated. An exponential decay curve is fitted to the neutron flux upon beam shut-off from which τ_{meas} is computed. Lastly, an estimate for τ_{fi} is found by utilizing equation 2.7.

A decaying neutron signal from a beam-blip in a standard MST RFP plasma is shown below in Figure 23. The various colored lines represent the fitted decay curves that correspond to their labeled τ_{fi}. Rather intuitively, the faster the decay the smaller τ_{fi} and vice-versa. Figure 23 indicates that the fast ion confinement time in the standard RFP appears to be classical. This is often the case and is discussed in great detail in the next chapter.
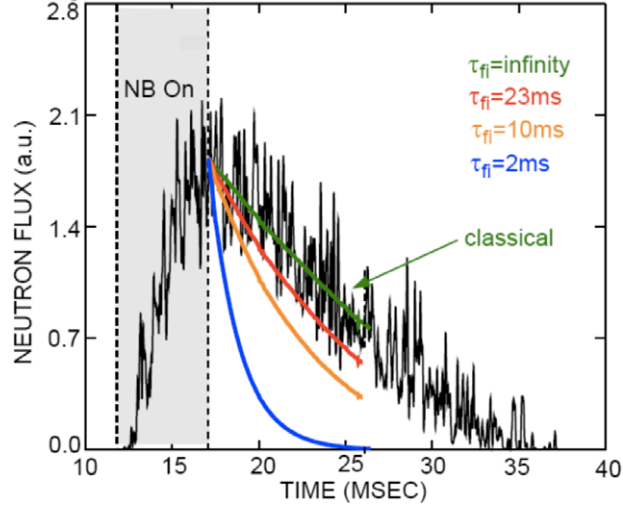
Figure 23: Decaying neutron flux from a deuterium fueled beam-blip in a standard RFP plasma. The dashed-vertical lines denote the short NBI pulse. Several decay curves are featured for a variety of τ_{fi}. Taken from reference [75].

2.4 ORBIT

This dissertation relies heavily on the particle tracking Hamiltonian guiding-center code ORBIT.[76] ORBIT provides a means to explore the fast ion response to parameters outside of experimental control. Developed by R. White at Princeton, the code integrates the particle motion using a 4th order Runga-Kutta method and Hamiltonian mechanics. The Hamiltonian of a particle in a magnetic field and electrostatic potential, Φ, is given in equation 2.8 where $\rho_\| = v_\|/v$ and $\mu = mv_\perp^2/2B$. Please note, the work in this thesis does not contain any electrostatics.

$$H = \rho_\|^2 B^2/2 + \mu B + \Phi \qquad (2.8)$$

The equations of motion are then described by Hamilton's equations (equations 2.9) with the canonical momentums, P_θ and P_ϕ, and coordinates θ and ϕ as variables. The

guiding-center motion is then found by solving equations 2.9.

$$\dot{\theta} = \frac{\partial H}{\partial P_\theta}, \quad \dot{P_\theta} = -\frac{\partial H}{\partial \theta} \tag{2.9a}$$

$$\dot{\phi} = \frac{\partial H}{\partial P_\phi}, \quad \dot{P_\phi} = -\frac{\partial H}{\partial \phi} \tag{2.9b}$$

References [76–78] provide a full derivation for the equations of motion and variable definitions.

The equilibrium and eigenfunctions used as input to ORBIT are solved in a toroidal geometry from the linearized, ideal MHD, zero pressure force balance equations coupled with Ampere's law. The equilibrium field is calculated from the zeroth order force balance equation (equation 2.10a), and the perturbations are derived from the first order contribution (equation 2.10b).

$$\mu_o \vec{J}_0 = \sigma \vec{B}_0 \tag{2.10a}$$

$$\vec{J}_0 \times \vec{b} + \vec{j} \times \vec{B}_0 = 0 \tag{2.10b}$$

$$\sigma(r) = \frac{2\Theta_0}{a} \left[1 - \left(\frac{r}{a} \right)^\gamma \right] \tag{2.10c}$$

The parameter Θ_0 corresponds to the on-axis value of the magnetic safety factor, $q(0)$, a is the minor radius, and γ is simply a variable that describes the shape of the λ profiles (λ is the Taylor parameter from equation 1.3). The values for Θ_0 and γ were simply found from trial and error until a suitable equilibrium was obtained with the desired form. The perturbations are solved via Newcomb's analysis in a toroidal geometry with MST's edge coil measurements supplying the boundary conditions.[28, 79] The full derivation of the magnetic equilibrium and perturbations may be found in references [46, 79].

An important feature of the equilibrium is that it must be axisymmetric. ORBIT assumes that the toroidal variation is constant. That is, for any equilibrium function, f, then $\partial_\phi f = 0$. This is not ideal for the QSH state which contains a helical core. VMEC equilibria (described later) may be used as input to ORBIT but only if they describe the standard, axisymmetric RFP. The QSH state is modeled in ORBIT by the 2D-equilibrium with a large $m = 1$, $n = 5$ perturbation. In this regard, ORBIT uses a 3D-field constructed from the axisymmetric equilibrium plus the perturbations which carry a dependence on the toroidal angle.[77]

Since the ORBIT equilibria are two-dimensional, the difference between the MH and QSH states lies in the $n = 5$ perturbation. Figure 24 presents example radial eigenfunctions for a MH ($\tilde{b}_5/|B| = 0.8\%$) and a QSH ($\tilde{b}_5/|B| = 7.2\%$) states. The eigenfunctions
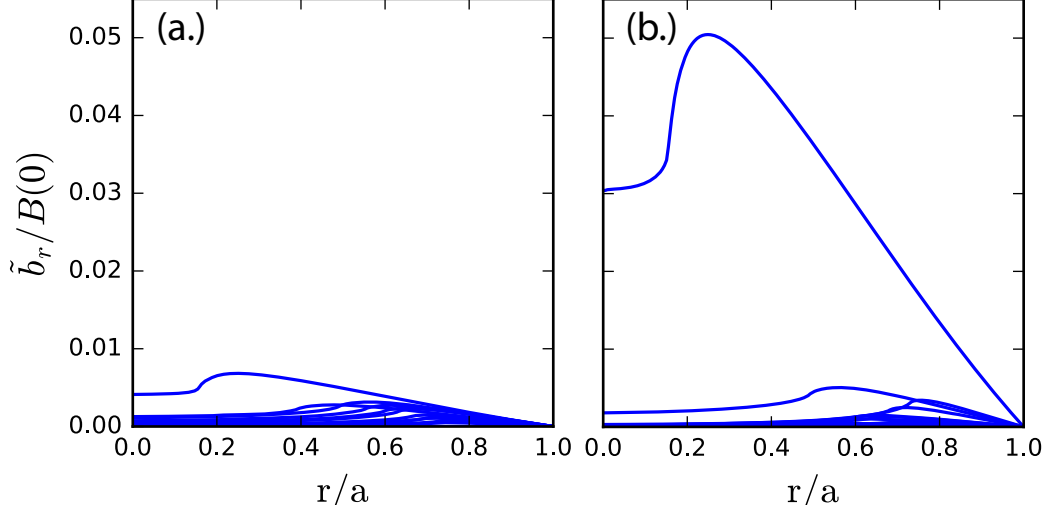
Figure 24: The radial eigenfunctions for the $m = 1$, $n = 5 - 16$ tearing modes for MH, (a.), and QSH, (b.), states.

are peaked at the corresponding rational surface locations (q-profiles not shown) and decrease in amplitude with mode number. The largest perturbation is the $n = 5$ mode.

The QSH case has an amplitude much larger than that of the MH case while the sub-dominant modes are of the same magnitude, creating the desired mode spectra. The relatively broad spectrum of the tearing modes validates the guiding-center description of the fast ions. The fast ion gyromotion may be neglected due to its spatial scales ($\sim$0.1-0.2 r/a) being much smaller than the perturbations.

Running ORBIT itself is rather quick and simple. The only required inputs for the equilibrium reconstruction are Θ_0, γ, and the plasma current. The perturbations require the $\tilde{b}(a)$ values found from MST's edge coils and the corresponding mode numbers. The simulation itself takes the particle information (number, mass, charge, and energy) and the particles' initial conditions. The number and amplitude of the perturbations may be changed as well as the particle collisionalities. The length of the simulation is set by the toroidal transit time of the particles, $\tau_{\text{tor}} = 2\pi R_0/v$, and typically ranges in value from 10 to a few thousand. Depending on the type of ORBIT run, the output can be as simple as the particles' starting and ending statistics or information may be stored at every time step. Discussed in Chapter 5, the helical flux, χ, can be used for ORBIT simulations involving a strong core-resonant mode. A quick reference guide with key ORBIT features is provided in Table 4 for the reader's benefit.

Feature	Characteristics
Equilibrium	Axisymmetric; Toroidal Geometry
Magnetic Perturbations	$m = 1, n = 5 - 16$ and $m = 0, n = 1 - 4$
Run Time	Instant - few days
Number of Particles	1 - few thousand
Collisions	Slowing, Pitch-angle/Classical
Free Variables	Particle mass, charge, and energy
Initial Conditions	(ψ_p, θ, ζ) or χ-surface and pitch
Run Types	Initial and Final Info., Particle Tracking, Helical Flux

Table 4: ORBIT Quick Reference Guide

2.5 VMEC and V3Fit

The Variational Moments Equilibrium Code (VMEC) code can create 3D-equilibria for stellarators, tokamaks, and RFPs.[80–82] VMEC finds an equilibrium that satisfies the ideal MHD force-balance equations constrained by Ampére's law and the necessity for the magnetic divergence to vanish everywhere:

$$\vec{J} \times \vec{B} = \vec{\nabla} p \tag{2.11a}$$

$$\vec{\nabla} \times \vec{B} = \mu_0 \vec{J} \tag{2.11b}$$

$$\vec{\nabla} \cdot \vec{B} = 0 \tag{2.11c}$$

VMEC solves equations 2.11 by minimizing the total energy of the plasma given in equation 2.12.[83]

$$W = \int \left(\frac{B^2}{2\mu_0} + p \right) dV \tag{2.12}$$

The energy minimization process is performed by altering the spectral components that describe the flux surfaces until a minimal energy state has been found. Equations 2.13

present the flux surface coordinates (R_ψ, Z_ψ), where λ_ψ represents a normalization function used to truncate the Fourier series.

$$R_\psi = \sum_{m,n} R_{m,n} \cos(m\theta - n\phi) \tag{2.13a}$$

$$Z_\psi = \sum_{m,n} Z_{m,n} \sin(m\theta - n\phi) \tag{2.13b}$$

$$\lambda_\psi = \sum_{m,n} \lambda_{m,n} \sin(m\theta - n\phi) \tag{2.13c}$$

Once the spectral components of equations 2.13 have been altered to produce a minimum energy state that satisfy equations 2.11, an equilibrium has been achieved.

As inputs, VMEC requires an initial safety factor profile, pressure profile, total magnetic flux, and device geometry. VMEC numerically solves an equilibrium solution based on these standard inputs without constraints from experimental diagnostics. VMEC equilibria can be optimized with the V3Fit reconstruction code which can contain experimental diagnostic constraints for the VMEC flux surface calculations.[84, 85] V3Fit will initialize VMEC and perform χ^2 minimization iterations until a convergence is reached between synthetic and measured signals.

2.6 STELLGAP

STELLGAP is a code developed by D. A. Spong at Oak Ridge National Laboratories which numerically calculates the shear-Alfvén continuum using a VMEC equilibrium as input.[86] STELLGAP follows the mathematical framework of Salat and Tataronis from

which the shear-Alfvén continuum in toroidal, low-pressure plasmas can be written as:

$$\mu_o \rho \omega^2 \frac{|\vec{\nabla}\psi|^2}{B^2} E_\psi + \vec{B} \cdot \vec{\nabla} \left[\frac{|\vec{\nabla}\psi|^2}{B^2} (\vec{B} \cdot \vec{\nabla}) E_\psi \right] = 0 \tag{2.14}$$

where ρ is the ion mass density, ψ the toroidal flux, and E_ψ the covariant ψ component of the electric field vector.[87] Of particular importance, for the RFP, STELLGAP and VMEC use the poloidal flux, ψ_p, instead of the toroidal flux to eliminate divergence issues when $1/q \to \infty$. The electric field of equation 2.14 is simplified by Fourier expansion to equation 2.15.

$$E_\psi = \sum_{n,m} E_\psi^{m,n} \cos(n\phi - m\theta) \tag{2.15}$$

By transforming to Boozer coordinates, equation 2.14 can be recast as the symmetric matrix eigenvalue equation:

$$\omega^2 \mathbf{A}\vec{x} = \mathbf{B}\vec{x} \tag{2.16}$$

where $\vec{x} = [E_\psi^{m_1,n_1}, E_\psi^{m_2,n_2}, E_\psi^{m_3,n_3}, ...]$. This eigenvalue equation is solved by diagonalizing the matrix and finding the eigenvalues (ω^2's). This is repeated at a range of ψ locations for varying (m, n) modes, allowing the Alfvén continuum to be constructed.

STELLGAP requires two input files along with the Boozer transformed VMEC equilibrium. The first file defines plasma characteristics such as ion mass and density profile. The second file contains the mode numbers of interest, the field periodicity, and mesh data. The routine XBOOZ_XFORM converts the VMEC output to Boozer coordinates and the XMETRIC routine prepares matrix elements from the Boozer coordinates. These codes are apart of the VMEC suite and must be run on the VMEC equilibria in order to have the correct input for STELLGAP. Thus, in summary, one can obtain a STELLGAP

calculated shear-Alfvén continuum by: acquiring a 3D-equilibrium with VMEC/V3Fit, transforming the equilibrium to Boozer coordinates with the XBOOZ_XFORM routine, converting the newly created Boozer coordinate equilibrium to usable matrix elements with the XMETRIC routine, and, lastly, using the transformed VMEC equilibrium as input to STELLGAP (along with associated plasma and Fourier mode files).

Chapter 3

Tearing Mode Induced Transport

3.1 Basic Fast Ion Physics

Fast ions interact with the thermal electron and ion populations via collisions. In a fusion reactor, the energetic alphas must impart their energy to the bulk plasma in order to self-heat the reactor through Coulomb collisions. Taking a test particle species denoted by superscript α traveling through a Maxwellian background species denoted by superscript β, one may derive the Coulomb collision frequencies shown in equation 3.1.[88]

$$\nu_s^{\alpha\backslash\beta} = (1 + m_\alpha/m_\beta)\Psi(x)\nu_0^{\alpha\backslash\beta} \tag{3.1a}$$

$$\nu_\perp^{\alpha\backslash\beta} = 2[(1 - 1/2x)\Psi(x) + \Psi'(x)]\nu_0^{\alpha\backslash\beta} \tag{3.1b}$$

$$\nu_\parallel^{\alpha\backslash\beta} = [\Psi(x)/x]\nu_0^{\alpha\backslash\beta} \tag{3.1c}$$

$$\nu_\epsilon^{\alpha\backslash\beta} = 2[(m_\alpha/m_\beta)\Psi(x) - \Psi'(x)]\nu_0^{\alpha\backslash\beta} \tag{3.1d}$$

$$\nu_0^{\alpha\backslash\beta} = \frac{4\pi n_\beta e_\alpha^2 e_\beta^2 \ln\Lambda_{\alpha\beta}}{(4\pi\epsilon_0)^2 m_\alpha^2 v_\alpha^3} \tag{3.1e}$$

$$\tag{3.1f}$$

Equations 3.1 make use of the Maxwell integral shown in equations 3.2a-3.2b and the Coulomb logarithm in equation 3.2c, where $\lambda_D = \sum_j \sqrt{\frac{\epsilon_0 k T_j}{n_j e_j^2}}$ denotes the plasma Debye

length. In a kinetic treatment, the bulk plasma ions and electrons possess Maxwellian distributions and act as the background species while the fast ions can be treated as the test particles. In practice, Taylor expanding the Maxwell integral and taking the appropriate limits for electron and ion backgrounds results in simplified equations for a fast ion test species. While equations 3.1 provide the exact solutions, please see reference [88] for the expanded, approximate forms.

$$\Psi(x) = \frac{2}{\sqrt{2\pi}} \int_0^x \sqrt{t}e^{-t}dt; \ \ \Psi'(x) = \frac{d\Psi}{dx} \tag{3.2a}$$

$$x \equiv x^{\alpha \backslash \beta} = \frac{m_\beta v_\alpha^2}{2kT_\beta} \tag{3.2b}$$

$$\ln\Lambda_{\alpha\beta} \approx \ln\left(\frac{\lambda_D}{\frac{e_\alpha e_\beta}{4\pi\epsilon_0(T_\alpha+T_\beta)/2}}\right) \approx \text{const} \tag{3.2c}$$

The collision frequencies in equations 3.1 correspond to momentum loss, perpendicular diffusion (deflection or pitch-angle scattering), parallel (speed) diffusion, energy loss, and a collisional reference frequency, respectively. Naturally, the slowing (equation 3.1a) and energy transfer (equation 3.1d) collisions are the most relevant in regards to the fast ions thermalizing with the bulk plasma. Pitch-angle scattering (equation 3.1b) becomes important when considering pitch-sensitive particle orbits.

Calculating the thermalization of the fast ions is relatively straight forward using the above equations. The energy loss rate for the fast ions is simply given by:

$$\frac{1}{E_f}\frac{dE_f}{dt} = -(\nu_\epsilon^{f\backslash i} + \nu_\epsilon^{f\backslash e}) \tag{3.3}$$

where both the ion and electron terms are included. By comparing the ion and energy terms in equation 3.3, one can determine the critical fast ion energy at which the electrons

or ions dominate the fast ion energy loss. The dominant energy transfer rate between the ions or electrons can be found in terms of a critical energy, E_c. The fast ions primarily lose their energy to the background electrons when $E_f > E_c$ and to the background ions when $E_f < E_c$. In MST, $E_c \sim 15\,\mathrm{T_e}$ and $\sim 7\,\mathrm{T_e}$ for 25 keV hydrogen and deuterium ions, respectively. For $T_e \sim 200 - 2000$ eV, the fast ions almost always impart their energy predominantly to the electrons. This likewise holds true for the slowing of the fast ions, i.e. ν_s. Pitch-angle scattering collisions occur mostly on the ions, however, as the more massive fast ions ignore deflections from the light electrons. The total time it will take for the fast ions to equilibrate to the thermal population can be calculated from:

$$\tau_{slow} = \frac{1}{\nu_s^{f\backslash i} + \nu_s^{f\backslash e}} \tag{3.4}$$

Using typical MST plasma parameters found in table 1, the fast ion slowing down time in MST calculates to about 21 ms. Slowing with impurity ions was neglected because the impurity population is relatively low in the core of MST where the fast ion content is high.

Upon entering the plasma, Lorentz forces act on the NBI deposited fast ions. This causes the ions to gyrate around the magnetic field lines with a Larmor radius given by equation 3.5, where e here denotes particle charge and $v_\perp$ represents the perpendicular particle velocity with respect to the magnetic field. Of note, the Larmor radius is also referred to as the gyroradius because it is a measure of the gyromotion of the particle around a field line.

$$r_L = \frac{mv_\perp}{eB} \tag{3.5}$$

The Larmor radius depends heavily on the particle pitch and, thus, deposition location

for the fast ions. For 25 keV ions in the MST, the typical Larmor radius is around 3-10 cm. This large disparance in radii is a consequence of the beam deposition across the major radius of the MST and the resulting fast ion pitch. Particles deposited near the core, i.e. high $v_\parallel$ and low $v_\perp$ possess a small gyroradius compared to ions deposited closer to the edge with higher $v_\perp$. Comparing to the bulk plasma, the thermal ions have a Larmor radius from a few millimeters to a couple centimeters while the electrons possess a gyroradius that is sub-millimeter. The relatively weak magnetic field of MST renders a fast ion population with large Larmor radius relative to device size. Even more striking, the fast ion gyroradii for other fusion devices such as the DIII-D tokamak and Joint European Torus, which possess much higher field strengths (order of a few Tesla), are all sub-centimeter. All in all, when considering particle beam energy, magnetic field strength, and device size, the energetic ions in MST maintain relatively large gyroradii. In terms of temporal scales, the frequency at which the particle revolves around the fieldline is given by the cyclotron frequency, or gyrofrequency, shown in equation 3.6.

$$\Omega_c = \frac{eB}{m} \tag{3.6}$$

Inserting typical values for MST plasmas, particles gyrate around the field lines on the order of MHz frequencies. This is quite fast and more rapid than almost all other plasma time scales of interest.

In addition to the gyromotion induced by Lorentz forces, the fast ions also experience perpendicular forces as a result of the nonhomogeneity of the magnetic field. Since the magnetic field is nonuniform, transverse gradients in the magnetic field strength exist and will result in variations of the instantaneous radius of curvature for the particle motion.

Similarly, the natural curvature from the toroidal shaping of the magnetic topology will also displace the particle trajectory due to the associated centrifugal forces. These outside forces can be expressed as drifts on the guiding-center particle motion. The grad-B and curvature drifts are given, respectively, by equation 3.7 where w_{perp} and $w_{\parallel}$ are the energy of the particle in the perpendicular and parallel directions, q is the particle charge, and $\vec{R}_c = \hat{B} \cdot \vec{\nabla}\hat{B}$ is the radius of curvature of the magnetic field.

$$\vec{v}_{\nabla B} = \frac{w_{\perp}}{qB} \left[\frac{\hat{B} \times \vec{\nabla}B}{B} \right] \tag{3.7a}$$

$$\vec{v}_{R_c} = \frac{2w_{\parallel}}{qB} \left[\frac{\hat{B} \times \hat{R}_c}{R_c} \right] \tag{3.7b}$$

As a quick aside, 1-2 kV/m radial electric fields produced by magnetic stochasticity and preferential loss of mobile electrons will impose an additional drift. The resulting $\vec{E} \times \vec{B}$ drift, however, is an order of magnitude smaller than the grad-B and curvature drifts for fast ions and may be ignored. Since equations 3.7 are proportional to the particle energy, the drift effects for fast ions can be quite severe.

3.2   Fast Ion Safety Factor

Introduced in Chapter 1, the safety factor strongly resembles the field line pitch around the machine. An analagous fast ion safety factor can be created by replacing the magnetic field components with the particle guiding-center velocities shown in equation 3.8.

$$q_{fi} = \frac{rv_{\phi}}{Rv_{\theta}} \tag{3.8}$$

The grad-B and curvature drifts must be included in the guiding-center velocities. Inserting equations 3.7 into equation 3.8, one finds:

$$q_{fi} \approx q_{mag} + \frac{s_\parallel}{B_\theta^2} r_L \frac{2(1 - \mu\Omega_c)B_\theta^2 - r\mu B^2 \Omega_c'}{2R\sqrt{1 - \mu\Omega_c}} \tag{3.9}$$

where q_{mag} is the magnetic safety factor, r_L is the fast ion Larmor radius, $\mu = \frac{v_\perp^2}{v_0^2 \Omega_c}$ where Ω_c denotes the fast ion gyrofrequency and $\Omega' = \frac{e}{m}\frac{dB}{dr}$ its radial derivative, and $s_\parallel = \frac{\vec{v} \cdot \vec{B}}{|\vec{v} \cdot \vec{B}|}$ represents the guiding-center pitch.[69]

While equation 3.9 appears quite complex at first, the root of the transformation from equation 3.8 to 3.9 lies in the guiding-center drifts. In a more simplistic thinking, one can recast equation 3.9 as:

$$q_{fi} \approx q_{mag} + \mathrm{Drift\,Terms} \tag{3.10}$$

The above equation simply states that the fast ion safety factor profile deviates from the magnetic safety factor profile due to guiding-center drifts. The presence of the grad-B and curvature drifts, which become substantial for fast ions, shifts the fast ion safety factor off the magnetic safety factor, decoupling the fast ion guiding-center motion from the magnetics. As it turns out, this has a significant impact on fast ion confinement in the standard RFP.

Just like the magnetic safety factor, the fast ion safety factor also contains resonant surfaces. While the fast ions possess a different pitch than the field lines, the fast ions respond to radial perturbations in a similar manner. Following the same logic, the fast

ions should have an analogous resonant condition that varies with the radial perturbations of the guiding-center velocity. That is, the fast ions possess an equivalent island structure similar to that of the magnetics in equation 1.6. The fast ion guiding-center islands will feel a radial velocity perturbation, $\tilde{v}_r$, that will result in a resonant island width given by:

$$w_{fi} = 4\sqrt{\left.\frac{\tilde{v}_r r_s}{V_\theta n |q'_{fi}|}\right|_{r_{s,fi}}} \approx 4\sqrt{\left.\frac{\tilde{b}_r r_s}{B_\theta n |q'_{fi}|}\right|_{r_{s,fi}}} \tag{3.11}$$

where V_θ is the poloidal-guiding center velocity, q'_{fi} is the gradient of the fast ion safety factor, and $r_{s,fi}$ is the fast ion rational surface. The right side of equation 3.11 makes use of the fact that $\tilde{v}_r/V_\theta \approx \tilde{b}_r/B_\theta$ in the RFP.[69] This demonstrates that localized island formation occurs in fast ion phase-space as a response to the radial magnetic perturbations. Unlike the magnetic islands, however, the fast ion guiding center islands experience the radial magnetic perturbation at the location of the fast ion resonance, $r_{s,fi}$. Due to the large shift in the fast ion safety factor from the drifts, the difference in island location can be quite significant. Figure 3.11 presents a magnetic and fast ion safety factors for a $F < 0$ RFP.

The upward displacement of the fast ion safety factor is a result of the guiding-center drifts. The shift in safety factor may add fast ion phase-space resonances that do not exist in the magnetic topology. In the case of Figure 25, the $m = 1, n = 5$ rational surface does not exist in the magnetics but does in fast ion phase-space. Another observation is that the corresponding islands between the two safety factor profiles have different widths. This stems from the fast ion guiding-center islands experiencing the radial magnetic perturbations at the location of the shifted fast ion resonances. The radial magnetic eigenfunctions are maximum at the magnetic resonance locations, so
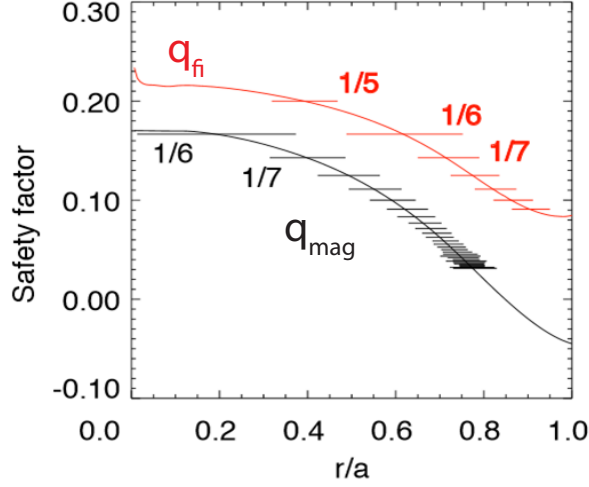
Figure 25: Fast ion safety factor (red) plotted with the magnetic safety factor (black) for a standard RFP. Taken from reference [89].

the $\tilde{b}_r$ values evaluated at the fast ion resonances will be smaller, resulting in reduced guiding-center islands widths. The altered fast ion resonances play a critical role in fast ion confinement in the standard RFP.

3.3 Fast Ion Confinement in the Standard RFP

The topology of the standard RFP gives rise to a q-profile with many rational surfaces where tearing instabilities occur that produce regions of magnetic reconnection and island formation. The RFP's large magnetic shear places the islands relatively close together (especially near the edge) where the island boundaries overlap. This establishes a very stochastic magnetic topology as magnetic field lines can transition from island to island, wandering across the plasma radius. An example of the magnetic stochasticity can be seen in the Poincaré plot of Figure 26 (a.) for a field line initially near the core.

Thermal particles do not experience large drifts due to their low energies. Consequently, thermal particles' guiding-center trajectories follow that of the magnetic safety factor and fall prey to the tearing mode induced stochasticity.[30, 90] This field line wandering becomes the dominant transport mechanism for the thermal particles and results in confinement times of around a few ms, much shorter than the plasma lifetime.[91–93] NBI heating studies on MST found that little to no injected power transferred to the electrons due to their poor confinement. A change in T_e was only found in an enhanced confinement operating regime that weakens the effects of the tearing instabilities and lowers the electron heat conductivity.[94–98]
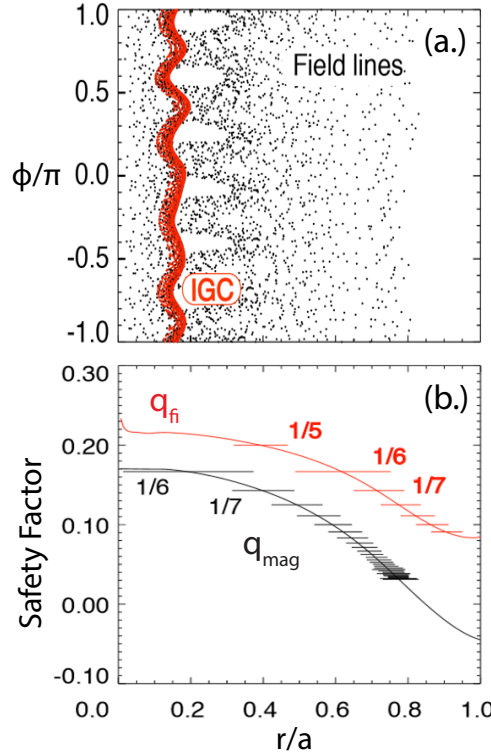
Figure 26: Poincaré plots, (a.), of the magnetic field structure (black) and 20 keV hydrogen ion guiding-center motion (red) with reference to their respective q-profiles in (b.) Taken from reference [89].

The fast ions decouple from the magnetic topology and, thus, experience drastically different transport physics. The shift in the fast ion safety factor leads to its own resonances with reduced ion guiding-center widths. Furthermore, since the fast ion safety factor shifts upward, the resonance locations fall farther out in radius. This leaves a large area near the core absent of $m = 1$ islands where fast ions should simply traverse at the prescribed helicity. Fast ion islands appear around mid-radius and experience significant overlap only near the edge, creating a large, stochastic-free region in fast ion phase-space. Fast ions deposited near the core experience little to no perturbations of their guiding-center velocity and maintain good confinement properties.[89] This can be seen in Figure 26 (a.) where the fast ion guiding center-motion remains near the core and completely ignores the magnetic stochasticity.

Shown in Figure 27, monitoring the fast ion position as a function of its slowing provides a great illustration of the motion across the islands. Initially, the fast ion lives
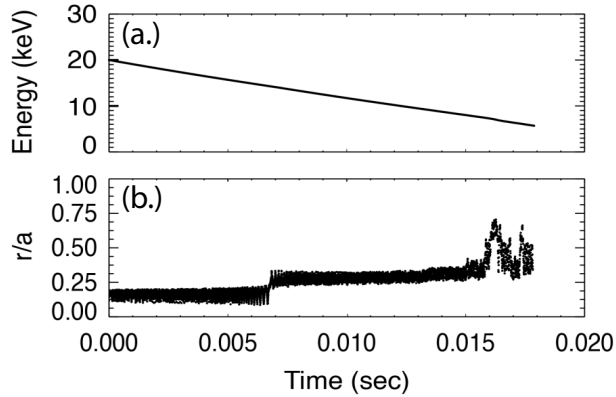
Figure 27: The classical slowing of an initial 20 keV hydrogen ion in the core, (a.), with its corresponding guiding center location, (b.). Taken from reference [89].

near the core and its location remains relatively fixed. As the ion slows, the guiding-center drifts become smaller and the fast ion safety factor approaches the magnetic

safety factor. At around 7 ms, the fast ion jumps in position and becomes trapped in the $n = 5$ fast ion island. Eventually, the velocity of the ion slows enough that it starts to experience the magnetic stochasticity and wander radially at around 15 ms.

Experimentally, the effect of the fast ion resonances on the confinement properties can be observed with the beam-blip technique for co and counter-injected NBI. Normally, the NBI injects particles in the co-going direction of the plasma current. By reversing the transmission lines on MST, the plasma current direction is reversed to flow against the fast ion injection. Mathematically, this induces a sign flip in equations 3.7 and 3.8 and leads to the fast ion safety factor shifting down instead of up, as shown in Figure 28. For the counter-injection case, the fast ion resonant surfaces shift radially inward and lie closer together. The fast ion guiding-center islands (not shown) overlap more
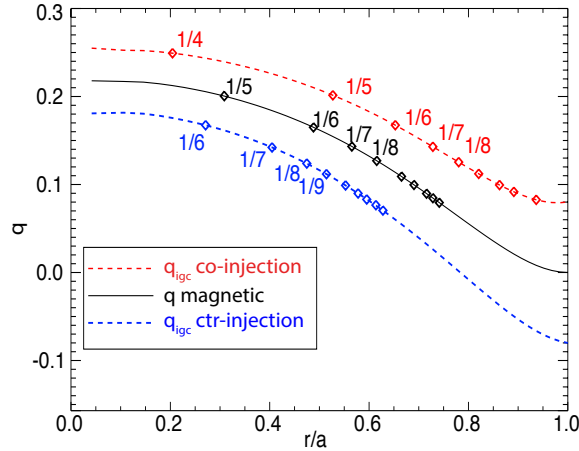
Figure 28: The magnetic (black), co-injected fast ion (red), and counter-injected fast ion (blue) safety factors and their corresponding resonant locations in a $F = 0$ RFP discharge. Taken from reference [99].

and extend closer to the core. This produces a stochastic fast ion phase-space which will have a greater impact on the core-deposited ions. The counter-injection case should result in fast ion confinement and transport similar to that of the thermal population.

Figure 29 presents two neutron signals for co and counter-injected deuterium NBI in standard RFP plasmas. The co-injected NBI produces substantially more neutron
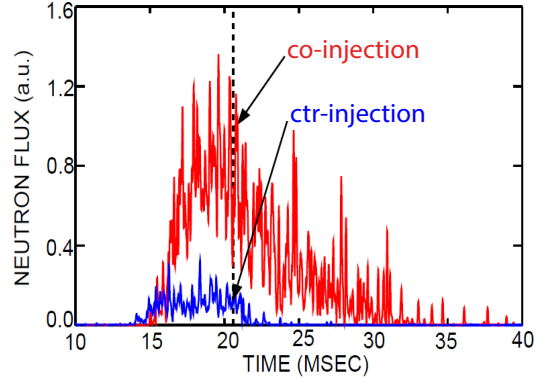
Figure 29: Global neutron flux measurements for co-injected (red) and counteri-injected (blue) NBI based on measurments taken in reference [99]. The dashed vertical line denotes the beam cutoff.

flux compared to the counter-injected case which is indicative of better confinement. The counter-injected NBI neutron flux has a steep drop off after the beam terminates while the co-injected signal lasts upwards of 10 ms. Referring back to Figure 23, the calculated fast ion confinement time for the co-injection case appears to be classical while the counter-injection case is around 1 ms. Thus, these measurements provide direct verification of two key points: 1. the fast ion safety factor and guiding-center resonances provide an apt description of the fast ion confinement in the standard RFP and 2. fast ion confinement in the standard RFP is on the order of the classical slowing.

3.4   Fast Ion Suppression of the Core Tearing Mode

The fast ions also impact the core-resonant tearing mode itself and the transition to the QSH state.[70] The amplitude of the dominant tearing mode decreases with beam injection. A series of shots with hydrogen NBI in $F = 0$ plasmas were ensembled together to produce Figure 30. The mode suppression factor is defined as the normalized change
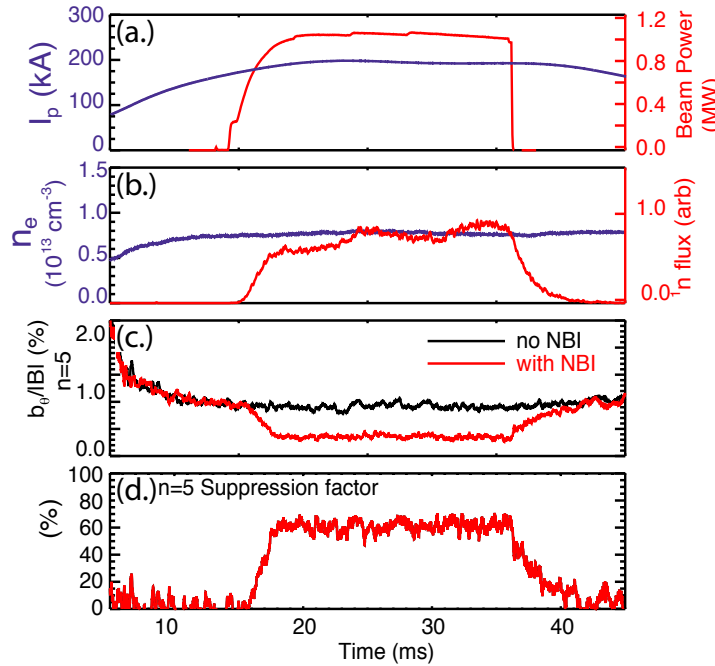
Figure 30: NBI induced suppression of the $n = 5$ tearing mode. Panel (a.) gives the plasma current and beam power, (b.) shows the line-averaged electron density and global neutron flux from the 5% fuel doping, (c.) presents the $n = 5$ tearing mode amplitude normalized to the equilibrium field strength, and (d.) is the suppression factor. Taken from reference [70].

in the edge-measured fluctuation amplitude relative to the non-NBI discharges. Figure 30 shows that the NBI suppresses the $n = 5$ tearing mode by up to 60% of its typical value. The sub-dominant tearing modes (i.e. $n = 6, 7, ...$ in the above case) demonstrate no change with the injected fast ions. This experiment has been replicated for deeply

reversed plasmas, where the $n = 6$ mode becomes dominant, and the same trend followed with suppression of the $n = 6$ mode and no change in the others. Moreover, while the core-resonant tearing mode amplitude decreases, no apparent change occurred in the respective magnetic island widths. Since the fast ions ignore the island-induced stochasticity, the fast ion confinement remains unchanged. The NBI may inject on-axis current, however, which can flatten the q-profile near the core.[70, 100]

This fast ion induced tearing mode suppression becomes noticeable in the RFP's transition to the helical state. The QSH state establishes itself when the core-resonant tearing mode decouples from the sub-dominant modes and grows in value. The NBI can combat this growth and dampen the transition. From an operational standpoint, it has been found that going to lower density is often necessary in order to achieve the QSH state for a given shot with NBI than without NBI. The exact physics behind the fast ion driven tearing mode suppression are not fully understood. The decrease in density follows mainly from the empirically driven observation that the helical transition occurs more readily at high Lundquist number ($S \sim 1/\sqrt{n}$). While an entire thesis may be devoted to the causes of the helical transition and the stabilizing effects of fast ions, it is sufficient to state that the fast ions have a small, but non-negligible, impact on the magnetic topology in the QSH state.

3.5 Thermal Transport in the Helical RFP

While thermal particles are not the focus of this thesis, it is important that their response to the QSH topology be addressed. If one may recall, the QSH state forms

a localized core region of reduced magnetic stochasticity. The decoupling of the core-resonant tearing mode from the subdominant modes establishes a well-ordered helical core where thermal particles no longer experience rapid transport. Since the thermal particles in the RFP tightly follow the field lines, it follows that they react to the chaotic healing with increased confinement.[101, 102] The subdominant tearing mode stabilization translates to a strong thermal transport barrier.[103] In short, extensive work on the MST and RFX-Mod RFPs have discovered that the thermal particle confinement improves drastically in the helical state.[35, 104, 105]

Experimentally, the improved thermal confinement in the QSH state most readily presents itself in measurements of the election population, such as electron density, temperature, and bremsstrahlung radiation. Figure 31 presents such measurements from QSH plasmas in RFX-Mod. The sharp rise in electron temperature, density, and x-ray
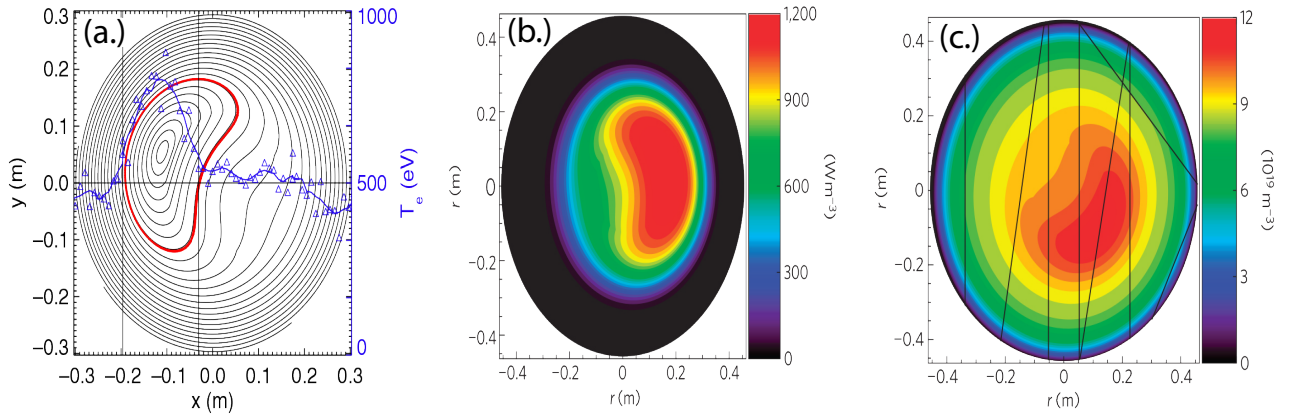
Figure 31: Measurements from RFX-Mod showing strong thermal confinement in QSH: (a.) Thomson scattering electron temperature measurements (blue) across flux surfaces rise in the helical core (red), (b.) 2D-reconstructed SXR emissivity measurements peak in the helical core, and (c.) 2D-reconstructed line-averaged electron density measurements (black lines) peak in the helical core. Note: The measurements occurred at different phases. Figures were taken from references [16, 103].

emissivity across the helical core demonstrate the transport barrier. While ion measurements are lacking, simulations have shown similarly improved confinement. [106–109]

Interestingly, some have argued that this presents a possible avenue for a new magnetic confinement fusion scheme.[16] The standard RFP is plagued by poor stability that gives rise to poor thermal confinement properties, but the QSH state overcomes this disadvantage. Currents within the RFP create the toroidal field via the dynamo effect and present enormous advantages for a RFP fusion reactor concept. Namely, the viability for a purely ohmically heated plasma.

3.6 ANPA Measurements

Probing the fast ion population within the plasma by NPA has reproducibly shown a stark drop in signal in the helical state.[99] More QSH shots were taken with ANPA data for both hydrogen and deuterium fueled NBI and tangential and radial viewing geometries. Both lines of site for both beam species show distinct decreases with the growth in the $n = 5$ helical perturbation. Figures 32 and 33 show representative shots for the radial and tangential sight lines, respectively. Both viewing geometries show the distinct disappearance of beam signal during large $n = 5$ amplitude.

In order to examine larger trends among the dominant perturbation and the sub-dominant modes, an ensemble was constructed from hundreds of discharges with the radial ANPA view. For a given shot, the time domain was split into 250 μs windows during the beam injection. For each time window, the tearing mode amplitudes were found from edge magnetic coils and averaged to single values for the dominant and sub-dominant modes. The rate of change of the 25 keV ANPA signal was then calculated
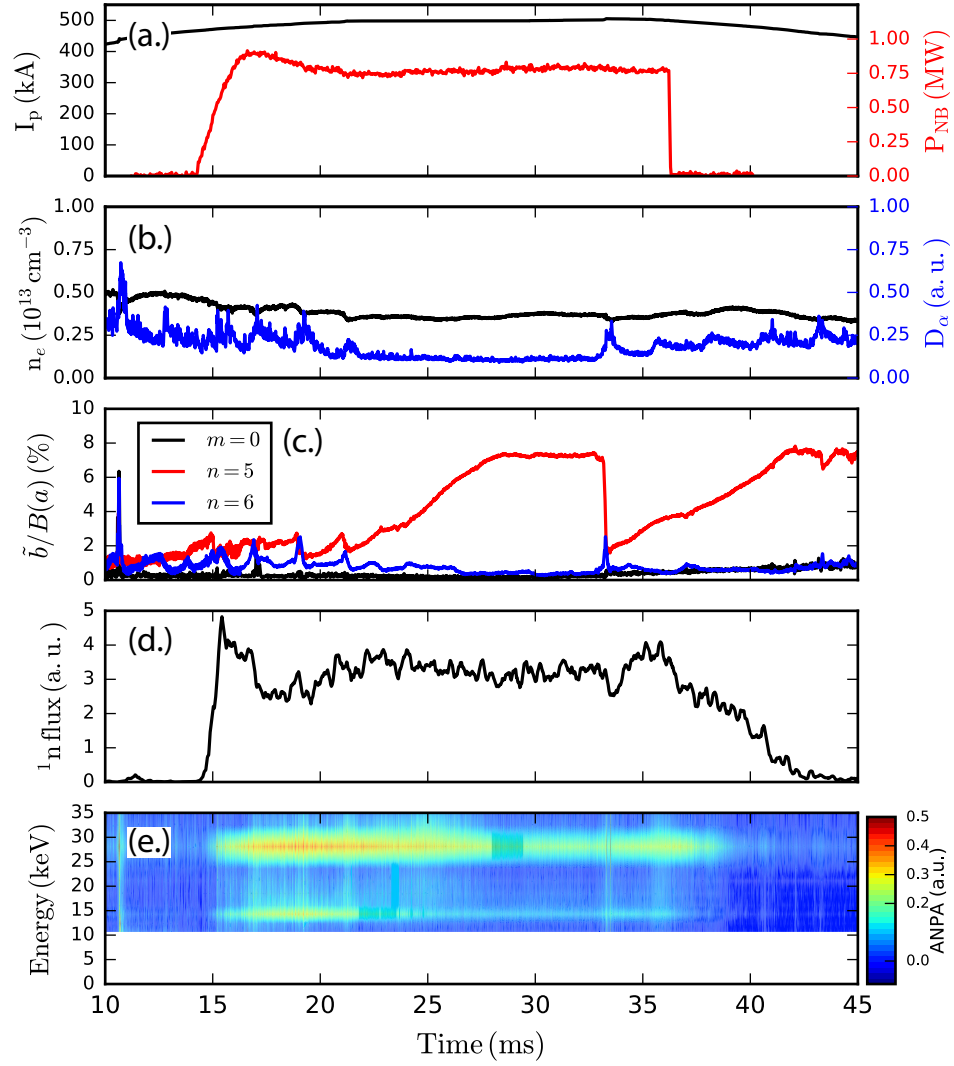
Figure 32: Radially oriented ANPA measurement, (e.), for deuterium fueled NBI with plasma current and beam power, (a.), electron density and D_α emission, (b.), normalized tearing mode amplitudes, (c.), and global neutron flux, (d.).
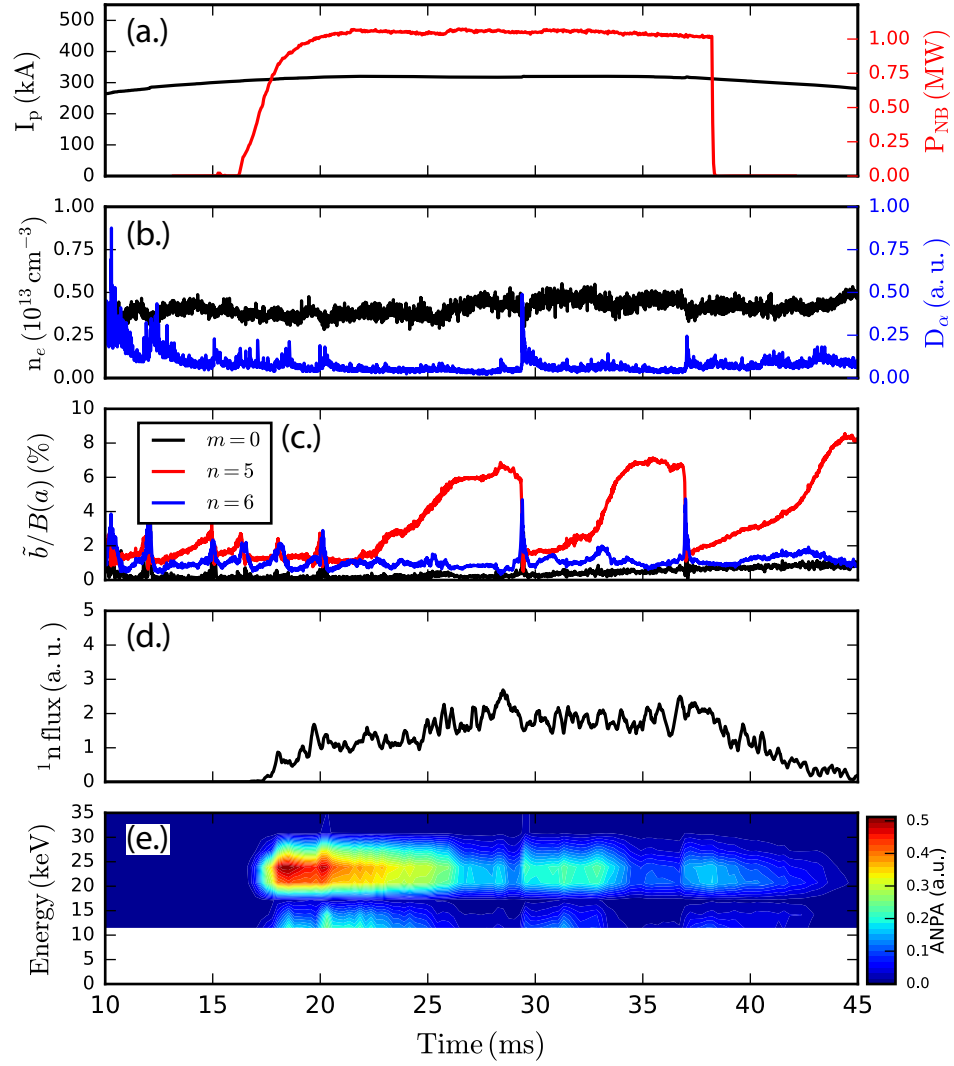
Figure 33: Tangentially oriented ANPA measurement, (e.), for hydrogen fueled NBI with plasma current and beam power, (a.), electron density and D_α emission, (b.), normalized tearing mode amplitudes, (c.), and global neutron flux, (d.).

for each window, normalized to the window center, and binned according to the respective tearing mode amplitudes. This process was repeated for hundreds of shots with the radial ANPA view and averaged together to produce Figure 34.
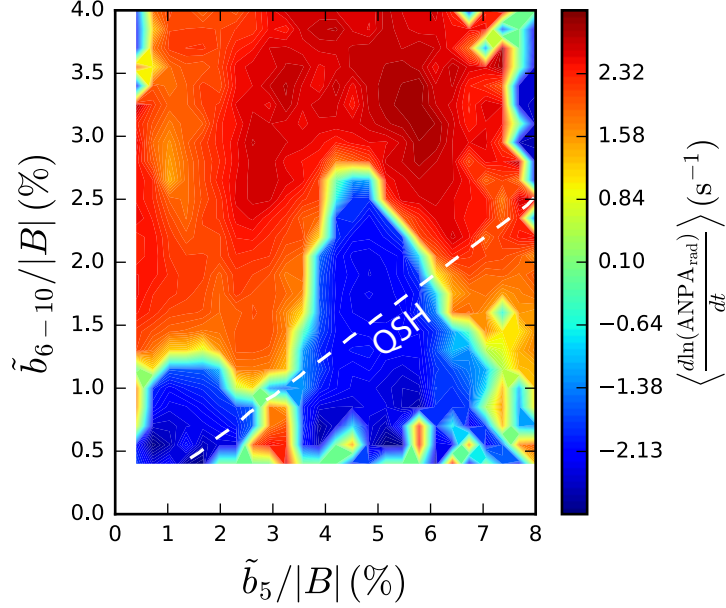
Figure 34: Ensemble average of the normalized rate of change of the radial ANPA signal with the dashed area representing the QSH regime of $N_s < 1.2$.

The measurements do not show a perfect trend, but the rate of change of the ANPA signal generally decreases in the QSH region and increases outside of it (i.e. in the MH state). This is consistent with the characteristic drop in signal observed in a shot-to-shot analysis such as that shown in Figure 32. In general, it appears that at low subdominant amplitudes the ANPA signal decreases and increases at high amplitudes. This is roughly consistent with the labeld QSH regime except for the feature at $\tilde{b}_5 \sim 4.5\%$ that protrudes across the boundary. The helical geometry, however, greatly skews any interpretation of the ANPA measurements.

The neutral particle analyzer signal is a line-averaged measurement highly sensitive

to particle pitch and neutral density. Since the D_α measurements remain relatively fixed throughout the discharges, the drop in ANPA signal cannot be attributed to a sudden change in the neutral population. The detector's pitch sensitivity, however, makes for difficult inferences in the helical RFP where the core has shifted. Shown in Figure 35, the helical core shifts out of the tangential ANPA sight line near the geometric center. The tangential view will sample parts of the helical core across its near and far lines of
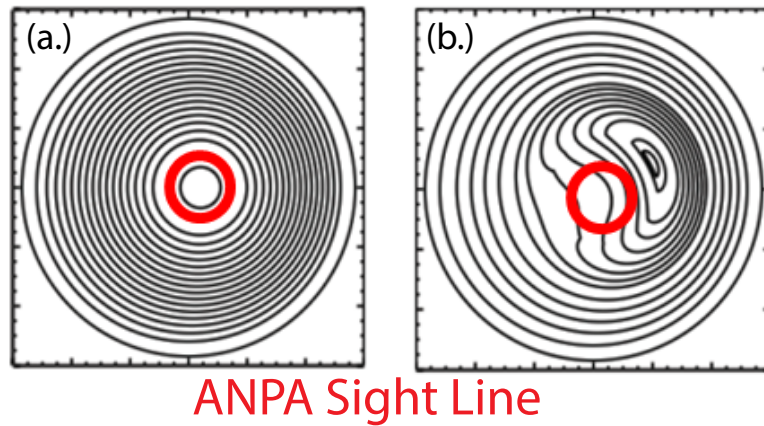
Figure 35: Tangential view for the ANPA line of sight in standard RFP, (a.), and QSH plasmas, (b.).

sight. Thus, the tangential view of the ANPA becomes rather complicated in the QSH state.

The radial ANPA view provides a more useful interpretation in the QSH state where RMPs can lock the helical core across the ANPA sight line. The viewing chord still samples parts inside and outside the helical core, however, so the measurement is still a convolution of plasma position. Phase control was used to perform a full scan of all locking phases across the radial ANPA sight line but no phase dependence was observed. All in all, while one may presume that the decrease in the ANPA signal during large $n = 5$ tearing mode amplitude could be associated with fast ion losses, one cannot simply

rule out the pitch sensitivity of the detector or limit its scope in the plasma volume. Further evidence provided in this chapter strongly indicates that the fast ions undergo drastic losses in the QSH state, making the ANPA data circumstantial at best.

3.7 Neutron Measurements

The response of the fast ion content throughout the transitioning equilibrium was monitored with neutron flux measurements produced from DD-fusion events. The neutron signals support the notion of fast ion losses in the QSH state. Figure 36 portrays a representative QSH transition with deuterium fueled NBI and the corresponding neutron flux. During the growth in the $n = 5$ amplitude, characteristic of the QSH state, the neutron flux starts to fall. All other pertinent plasma parameters remain relatively fixed, so the change in the neutron signal may be attributed to the fast ion content. When the QSH state crashes back to a MH state around 22-23 ms, the neutron flux begins to grow again until about 20 ms where $\tilde{b}_5$ climbs again. The neutron flux starts decreasing again untitl the beam shuts off. So, it appears that whenever the QSH state occurs a drop in the neutron signal follows which may be inferred as fast ion losses.

A second example can illustrate other typical characteristics of neutron behavior at the QSH transition. Figure 37 presents a rather prolonged QSH state where the neutron flux remains at a constant level throughout. This does not necessarily mean that losses are not occurring. It simply implies that the fast ion losses balance the sourcing from the neutral beam. Equation 3.12 describes the rate of change of the fast ion density, n_{fi}, as a relation between the NBI sourcing, S_{NBI} which is proportional to the beam current,
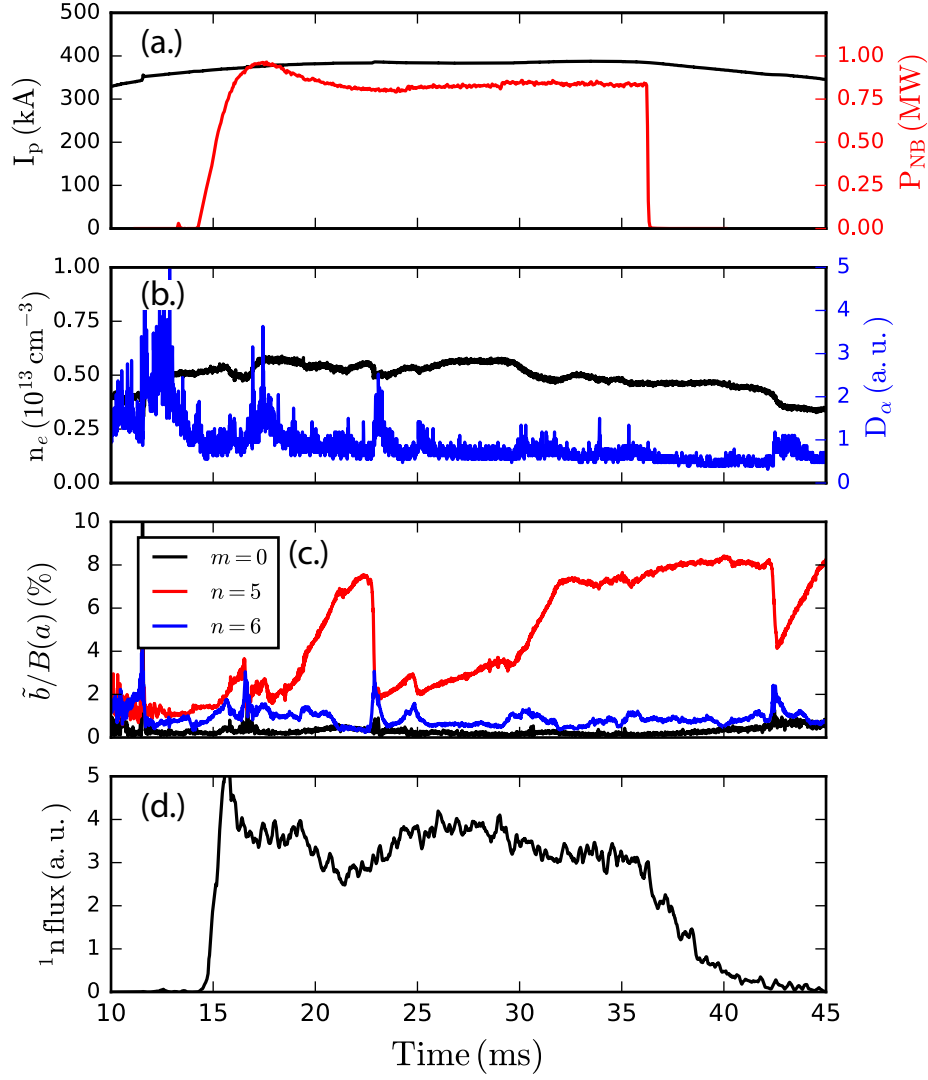
Figure 36: Decreasing global neutron flux measurement, (d.), in the QSH state with plasma current and beam power, (a.), electron density and D_α emission, (b.), and normalized tearing mode amplitudes, (c.).
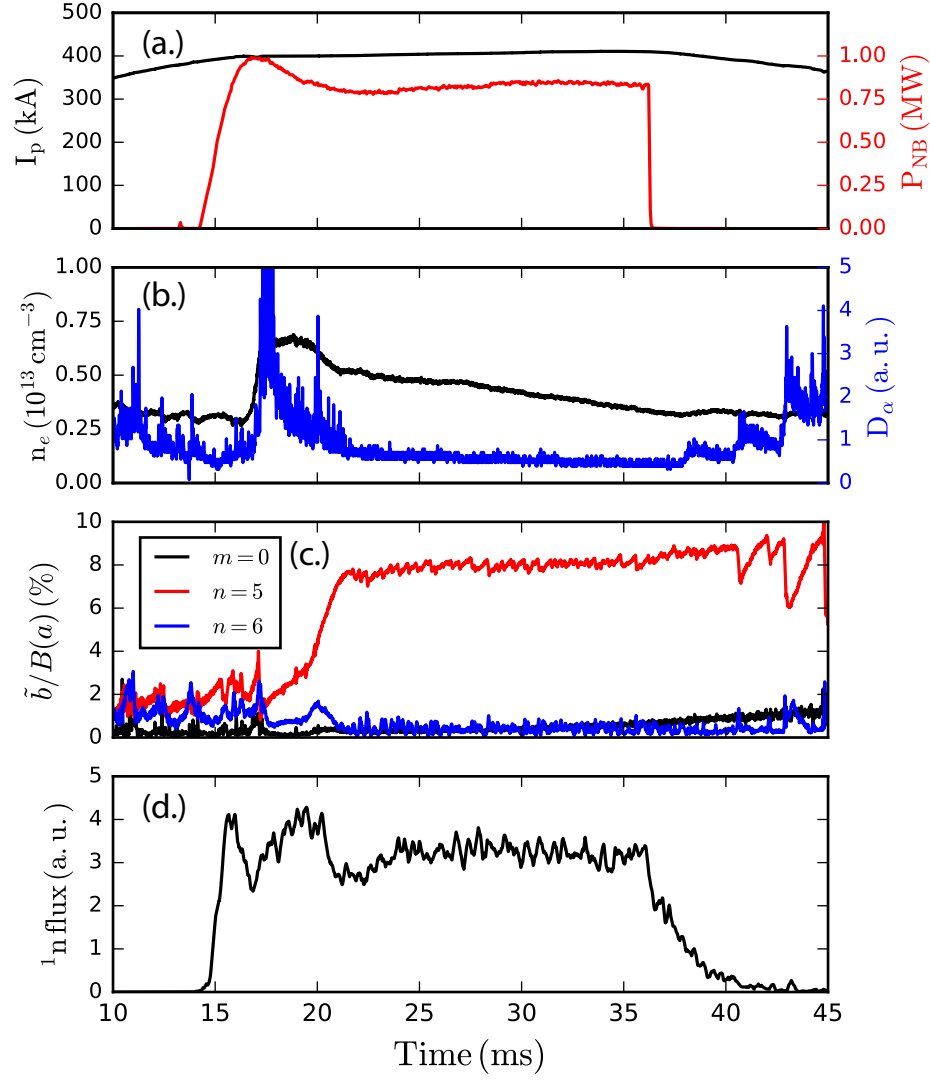
Figure 37: Constant global neutron flux measurement, (e.), in the QSH state with plasma current and beam power, (a.), electron density and D_α emission, (b.), and normalized tearing mode amplitudes, (c.).

and a loss term that is inversely proportional to the fast ion confinement time, τ_{fi}.

$$\frac{dn_{fi}}{dt} = S_{\text{NBI}} - \frac{n_{fi}}{\tau_{fi}} \tag{3.12}$$

Since $dn_{fi}/dt \sim 0$, equation 3.12 provides a manner in which to estimate the fast ion confinement time. The difficulty, however, lies in knowing the fast ion density at any moment in time. At present, this is not experimentally possible on MST. The beam at full power produces a sourcing term of approximately $1.5 \times 10^{19}\,\text{m}^{-3}\text{s}^{-1}$. Collimated neutron measurements indicate a core fast ion density around $0.3 \times 10^{18}\,\text{m}^{-3}$ for a high current discharge.[110] The neutron flux in Figure 37 saturates at a level that is about 0.6 of the neutron flux in a standard RFP. If one were to assume the measurements held in the QSH state and scale the core neutron density appropriately, then the fast ion confinement time will be approximately 12 ms. This is much less than classical predictions and implies that other transport mechanisms are at play.

In an analysis of fast ion loss rate as a function of magnetic mode amplitudes, the same ensembling procedure performed with the ANPA signals was duplicated with the neutron flux to produce Figure 38 (a.). Part (b.) is the normalized rate of change shown in (a.) at two fixed core-resonant amplitudes: 1.7% and 6.7%. Examining part (a.), the fast ion driven neutron flux decreases with large core-resonant mode and weak secondary modes. Additionally, part (b.) shows that the neutron flux decreases more rapidly in the presence of subdominant tearing modes in the QSH regime than the MH regime. This suggests that the remnant tearing modes might play a more important role in the helical RFP than the standard RFP. Since the neutron flux is proportional to the fast ion density and the thermal deuterium population is kept relatively fixed by gas puffing, the

neutron flux provides a direct measure of the fast ion content. Yet again, measurements have indicated an extreme reduction of the fast ion population in the QSH state.
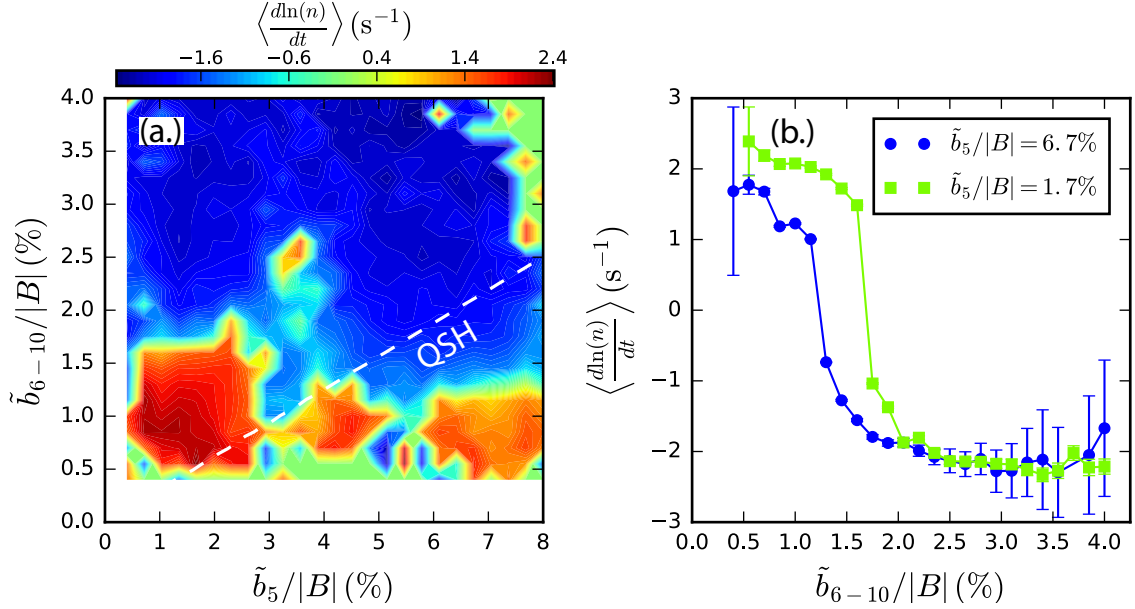
Figure 38: (a.) Ensemble average of the normalized rate of change of the global neutron flux with the dashed area representing the QSH regime of $N_s < 1.2$. (b.) Line cuts of the ensembled neutron flux rate as a function of normalized subdominant tearing mode amplitude for the QSH ($\tilde{b}_5/|B| = 6.7\%$) and MH ($\tilde{b}_5/|B| = 1.7\%$) states.

3.8   Fast Ion Confinement Time Studies

The fast ion confinement time, τ_{fi}, was directly measured on MST with the beam-blip technique [74], via the associated neutron flux decay, throughout the QSH transition. The results are plotted as a function of normalized core-resonant amplitude in Figure 39. The fast ion confinement time shows a marked decrease with the increase in the $n = 5$ tearing mode amplitude. The confinement falls from classical expectations to only a few ms.
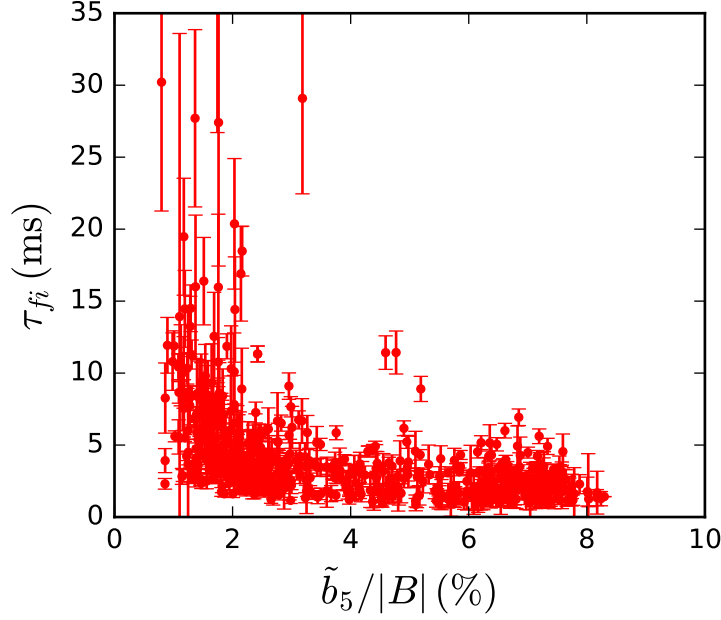
Figure 39: Fast ion confinement times found via the beam-blip technique as a function of the core-resonant tearing mode amplitude. This is an expansion of the dataset presented in reference [99].

Comparison studies were performed with the ORBIT code.[76] The ORBIT simulated loss times were calculated by depositing 600 fast ions in the plasma core with random pitch ($v_\parallel/v$) from 0 to 1. A particle was considered lost when it reached the wall boundary at which point its lost time was recorded.[108] The plotted loss times were calculated as the mean of all the lost times with varied tearing mode amplitudes. The simulations included both pitch-angle and slowing collisions.

Figure 40 (a.) shows the simulated fast ion loss times as a function of the core-resonant amplitude in settings that come as close as possible to mimicking the experiment within ORBIT parameters. The simulated fast ion loss times corroborate those measured and show a marked decrease with the transition from the MH state to the QSH state. Figure 40 (b.) plots τ_{fi} under the same constraints but with only the dominant $m = 1$, $n = 5$ mode active. Compared to the previous case where all tearing modes were present,
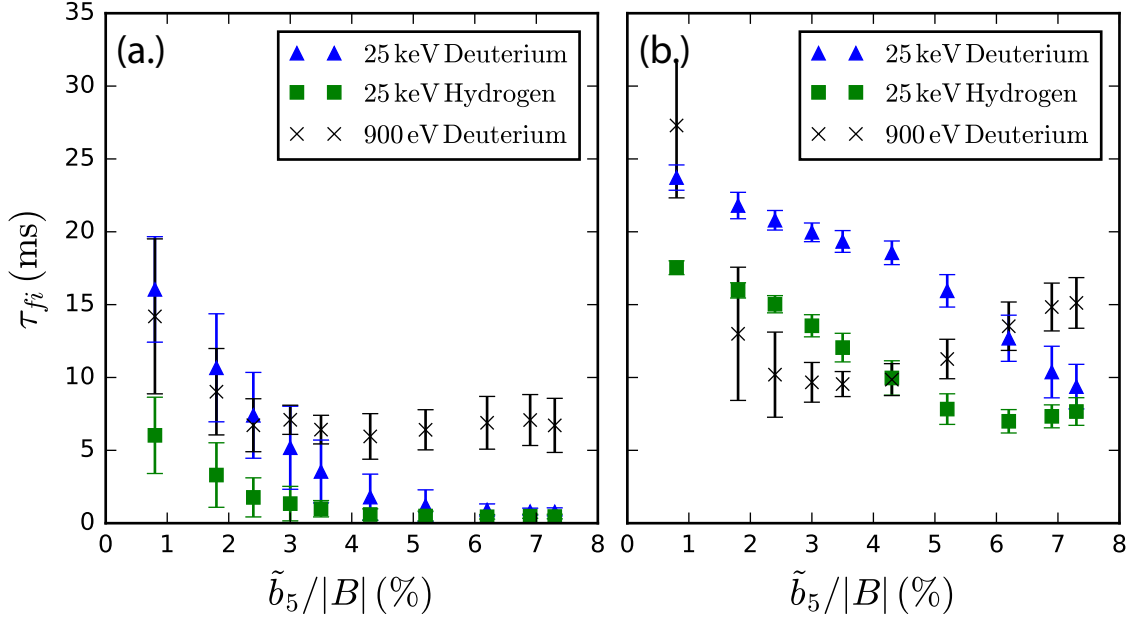
Figure 40: ORBIT computed τ_{fi} with $m = 1$, $n = 5 - 16$ and $m = 0$, $n = 1 - 4$ modes active, (a.), and with only the $m = 1$, $n = 5$ mode active, (b.).

the simulated fast ion confinement drastically improves when only in the presence of the $n = 5$ mode. This indicates that the subdominant modes are instrumental in fast ion confinement and transport in the QSH state. Additionally, the confinement time for 900 eV thermal deuterons was calculated for comparison to the RFX-Mod device. After an initial decrease, the thermal particle confinement starts to improve at high $\tilde{b}_5$ amplitude. This is indicative of the chaotic healing observed by the thermal population and the establishment of a transport barrier.

Figure 41 presents ORBIT calculated τ_{fi} as a function of scaled subdominant mode amplitudes at a fixed normalized core-resonant amplitude of 7.3%. This represents a transition from the far right of Figure 40 (b.) to the far right of Figure 40 (a.) and serves to quantify the degree at which the subdominant modes dictate global confinement. The rapid convergence to QSH-like loss times demonstrates that even the slightest presence
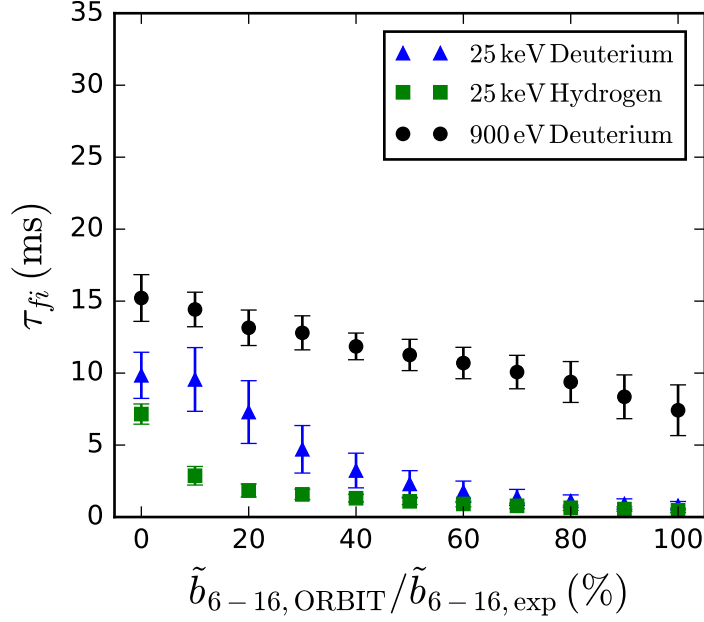
Figure 41: ORBIT computed τ_{fi} as a function of scaled subdominant mode amplitudes with $\tilde{b}_5/|B| \approx 7.3\%$.

of subdominant tearing modes ($\sim 30\%$ their experimental values) leads to drastic fast ion losses.

The ORBIT simulations corroborate the measurements from the beam-blip experiment and demonstrate a strong dependence on the core-resonant tearing mode amplitude. In addition, the confinement time is sharply impacted by the presence of the subdominant modes. This is direct confirmation of substantial fast ion losses in the QSH state. Coupled with the ANPA and neutron measurements, it has become apparent that the fast ions experience strong tearing mode induced transport. While the fast ions ignore the magnetic perturbations in the standard RFP, the QSH state has shifted the paradigm in a manner to ruin their confinement.

3.9   Fast Ion Phase-Space Stochasticity

Following the work in [89], the fast ion motion can be monitored as a function of the particle energy. This often provides insight into the magnetic perturbations' effects on fast ion transport. Figure 42 presents the radial motion of a fast deuteron in a MH state computed with ORBIT. The computation includes slowing collisions while omitting pitch-angle and classical scattering. This ensures that the particle motion is only dictated by the magnetic topology. At high energies, the fast ion remains well confined to the
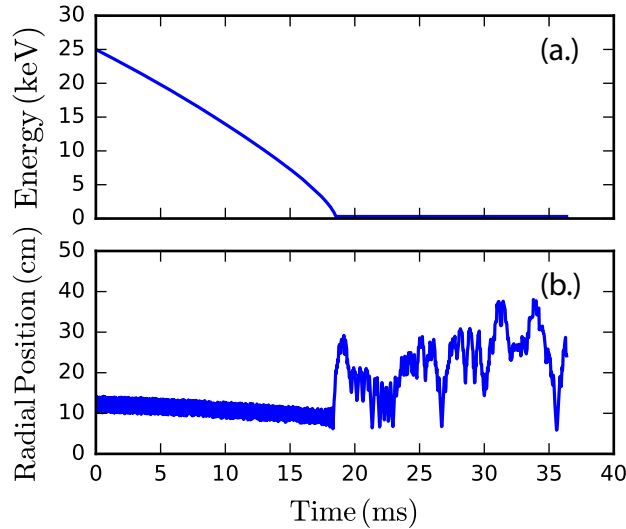
Figure 42: The energy, (a.), and radial position, (b.), for a 25 keV deuterium ion with initial position $r_0 = 12$ cm and pitch of 0.9 in a MH state with $\tilde{b}_5/|B| = 0.8\%$ found with ORBIT. This agrees with the results presented in reference [89].

core. As it slows, the fast ion safety factor approaches the magnetic safety factor and the ion starts to experience the tearing mode induced magnetic stochasticity. This is explicitly demonstrated in part (b.) by the random, chaotic motion of the particle once it has thermalized. These results match those of G. Fiksel quite well and provide an excellent comparison for QSH studies.[89]

The same ORBIT simulations were repeated for two cases: the first a QSH plasma with all magnetic perturbations present and the second with only the (1,5) tearing mode present. The results are plotted in Figure 43. The fast ion experiences large variations
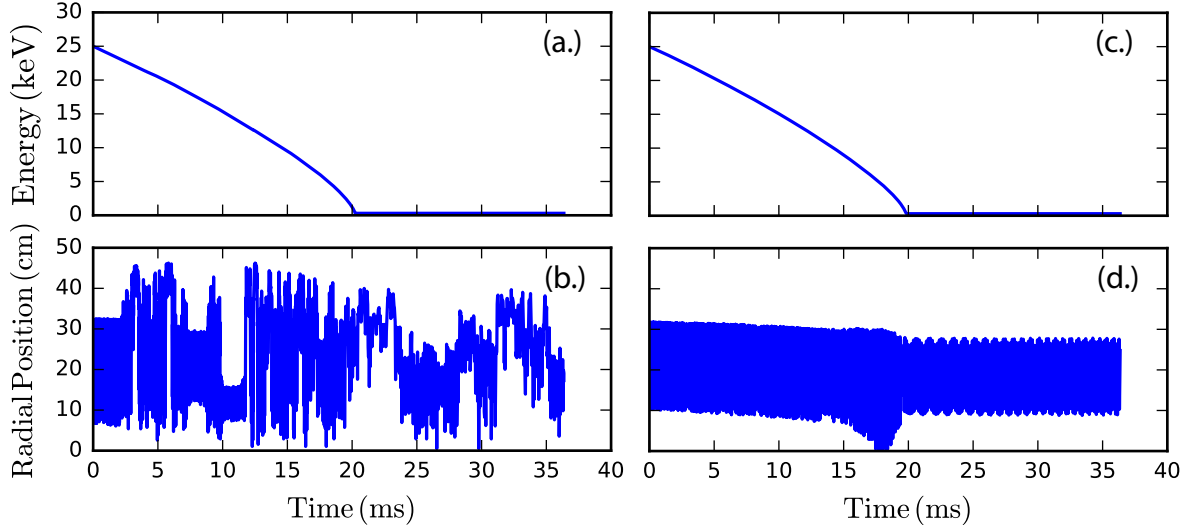
Figure 43: The energy, (a.) and (c.), and radial position, (b.) and (d.), for a 25 keV deuterium ion with initial position $r_0 = 12$ cm and pitch 0.9 in a QSH state with $\tilde{b}_5/|B| = 7.2\%$ found with ORBIT. Subplots (a.) and (b.) have all tearing modes present while subplots (c.) and (d.) only have the dominant (1,5) mode active.

in its radial position almost immediately in the QSH case with all modes present. The particle follows the same random walk pattern observed in the low energy MH case. When the subdominant modes are removed, though, the fast ion is relegated to a localized region near its starting point. Even when it thermalizes, the ion motion remains well ordered due to the lack of the secondary mode overlap. Figure 43 (b.) and (d.) provide a visual explanation for the confinement times found earlier.

In the previous section, fast ion confinement measurements showed rapid fast ion losses at high $n = 5$ amplitude. While Figure 43 (a.) - (b.) shows large radial displacements, the ion remains confined. The orbit was chosen explicitly for this reason: to

demonstrate the subdominant tearing mode dependence and the random walk behavior. Repeating the simulation for other QSH states, the fast ion was lost only after a short period, such as that depicted in Figure 44.
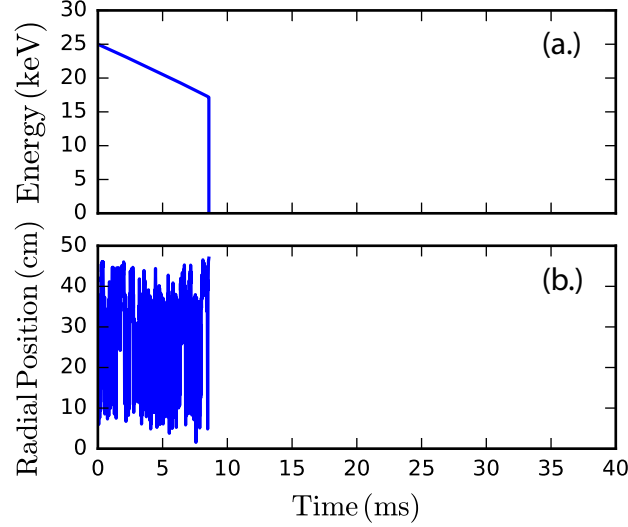
Figure 44: The energy, (a.) and radial position, (b.), for a lost 25 keV deuterium ion with initial position $r_0 = 12$ cm and pitch 0.9 in a QSH state with $\tilde{b}_5/|B| = 7.2\%$ found with ORBIT.

The wide radial structure in Figure 43 (d.) is the $n = 5$ island. As one can see, it is quite large and should overlap with the subdominant fast ion islands. Similiar to the magnetic topology in the standard RFP, this overlap should translate to a stochastic fast ion phase-space which would explain the strong degradation of fast ion confinement in the QSH state. ORBIT produced puncture plots were used to directly visualize the fast ion phase-space response to the tearing modes.

Figure 45 presents toroidally projected 25 keV deuterium Poincaré plots with increasing core-tearing amplitude in parts (a.)-(c.). Part (d.) shows the fast ion structure associated with only the $n = 5$ mode active at high perturbation level. The well-defined surfaces near the plasma core in part (a.) demonstrate the well-confined nature of fast
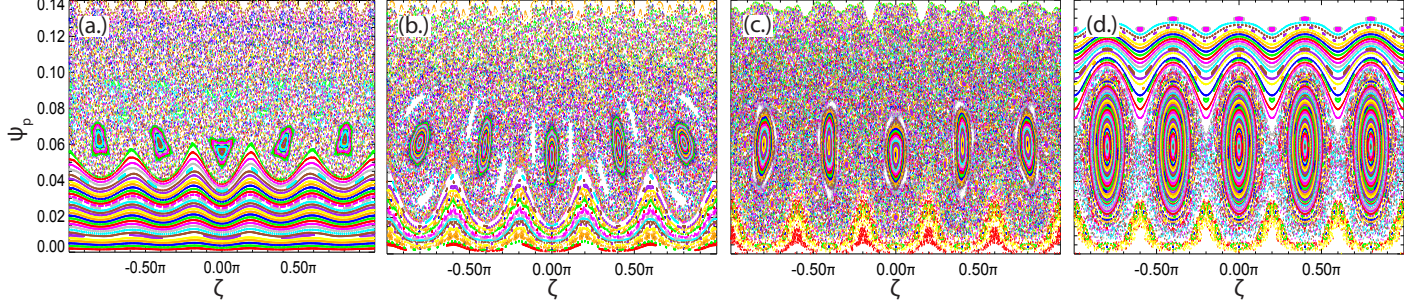
Figure 45: Fast ion phase-space Poincaré plots projected onto the toroidal plane and found with ORBIT for 25 keV deuterium ions, where ψ_p is the poloidal flux acting as the minor radius label and ζ is the toroidal angle. Subplots (a.) - (c.) have normalized core-resonant tearing strengths of 0.8%, 4.6%, and 7.5% and subdominant modes at experimental-like levels. Subplot (d.) is the same as plot (c.) with the exclusion of all subdominant tearing modes.

ions in the MH state.[89] As the helical perturbation strength grows in parts (b.) and (c.), however, those well-defined surfaces erode and the fast ion phase-space becomes more stochastic. The $n = 5$ fast ion guiding-center island presents itself in the plots as the localized structure around $\psi_p \sim 0.6$. There is clear evidence that the associated island width grows with the helical perturbation strength. Part (d.) is the Poincaré plot produced in the same scenario as (c.) but all of the subdominant tearing modes have been removed, allowing a full view of the $n = 5$ island structure. It spans a relatively large radial width that extends to the core region. This destroys the well ordered surfaces in part (a.) and allows fast ions in the core to quickly travel radially outward within the $n = 5$ island. The subdominant modes occur at large radius which, when coupled with the $n = 5$ island, result in significant island overlap and the observed stochasticity.

Using the puncture plots with only the (1,5) mode present, the $n = 5$ fast ion guiding-center island width can be calculated as a function of the core-resonant tearing mode strength. The $n = 5$ fast ion island widths are plotted in Figure 46. The island widths
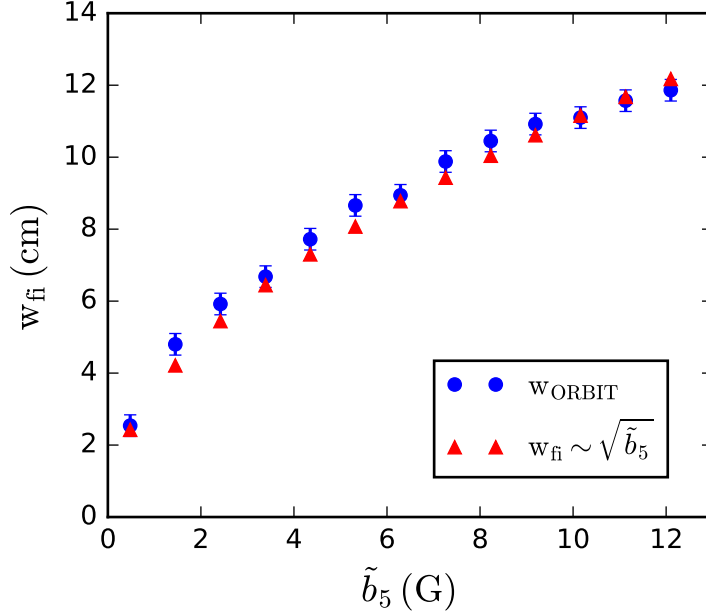
Figure 46: $n = 5$ fast island guiding-center width calculated from ORBIT Poincaré plots compared to the expected scaling: $w_{fi} \sim \sqrt{\tilde{b}_5}$.

scale exactly as expected from equation 3.11. Thus, with the increase in the $n = 5$ tearing mode amplitude in the transition to a QSH state, the corresponding fast ion guiding-center island will also experience considerable growth.

Figure 47 presents the fast ion guiding-center phase-space of a QSH state $(\tilde{b}_5/|B| = 7.5\%)$ but with scaled subdominant mode amplitudes. Parts (a.) - (c.) of Figure 47 have weakened subdominant amplitudes relative to Figure 45 (c.) which uses values typically found in the experiment. This allows for less island overlap, a larger $n = 5$ island, and a slightly improved confinement consistent with the confinement time simulations and neutron measurements. Part (d.) of Figure 47 has much larger subdominant amplitudes relative to Figure 45 (c.). In this case, the $n = 5$ island has shrunk considerably and almost all of the phase-space has become stochastic, providing further proof that the large $n = 5$ amplitude coupled with large secondary amplitudes is extremely detrimental
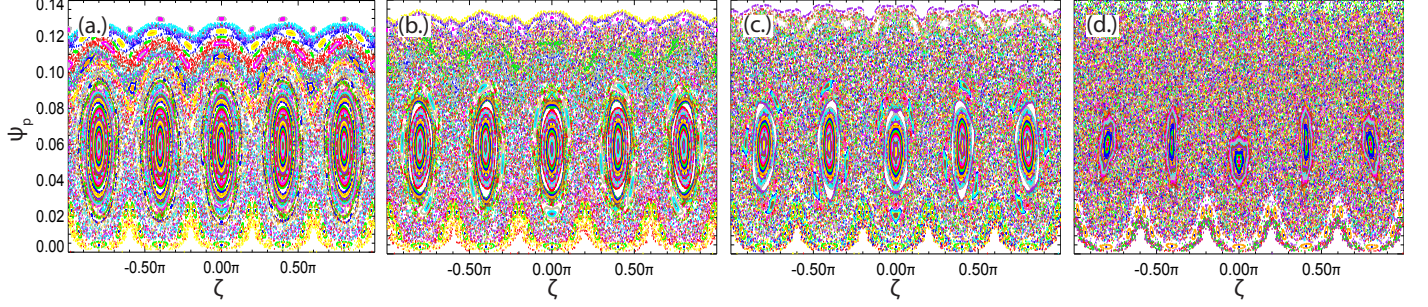
Figure 47: Fast ion phase-space Poincaré plots projected onto the toroidal plane and found with ORBIT for 25 keV deuterium ions, where ψ_p is the poloidal flux acting as the minor radius label and ζ is the toroidal angle. The subplots (a.) - (d.) have scaled subdominant mode amplitudes of 10%, 30%, 60%, and 200% relative to their original value of $\tilde{b}_{6-16}/|B| \sim 1.8\%$. All cases have a fixed normalized core-resonant tearing strength of 7.5% (same as Figure 45 (c.) and (d.)).

to fast ion confinement in the helical RFP.

The fast ions still observe some degree of de-coupling from the standard RFP's magnetic stochasticity. At large core-resonant amplitude, the fast ion phase-space surfaces near the core, representing the particle conservation, erode and ultimately disappear. The growth in the $n = 5$ tearing mode results in a slight reduction in fast ion confinement as particles are more easily transported outward by the larger island width. In the QSH state, subdominant modes greatly enhance the transport due to their additional overlap and result in considerable losses. Naturally, this appears to be a form of Rechester-Rosenbluth like transport where the magnetic chaos has propagated to fast ion phase-space.[90] The next section explores this idea further and attempts to identify the characteristic $D \sim \tilde{b}^2$ scaling.

3.10   Comparison to Rechester-Rosenbluth Transport

One may suspect that the tearing mode induced fast ion transport will mimic that of thermal particles in the standard RFP. That is, the fast ion phase-space stochasticity is a result of the growth in the $n = 5$ fast ion guiding-center island and the resulting overlap with the subdominant modes. At first glance, this appears to look just like Rechester-Rosenbluth transport except in fast ion phase-space.[90]

The fast ion island widths were examined with ORBIT and the overlap from the $n = 5$ island was found to significantly increase in the QSH state. The magnetic and fast ion safety factors were found according to equations 1.5 and 3.9 with ORBIT produced equilibria. The resulting safety factors and ORBIT calculated radial eigenfunctions were then used to compute the magnetic and fast ion island widths via equations 1.6 and 3.11. Care was taken to evaluate the relevant quantities at their associated resonances. The resulting safety factors and islands are plotted in Figure 48 for increasing $n = 5$ tearing mode strengths.

One may note the addition of the $m = 1, n = 4$ resonance to the fast ion safety factors. The (1,4) radial eigenfunction was found with the same Newcomb's analysis that was used for all other modes with the $n = 4$ amplitudes from MST's edge magnetic arrays as a boundary condition. The Newcomb's method is in good agreement with previous estimates and expectations. In the past, the $n = 4$ structure was found from a Debs simulation and scaled by the edge values $(\tilde{b}_{\mathrm{MST}}(a)/\tilde{b}_{\mathrm{Debs}}(a))$.[111] The ORBIT calculated $n = 4$ island width and location is consistent with the previous Debs estimates. The (1,4) mode was only added for the above demonstration of the fast ion resonances and was not included in any other ORBIT runs discussed in this thesis.
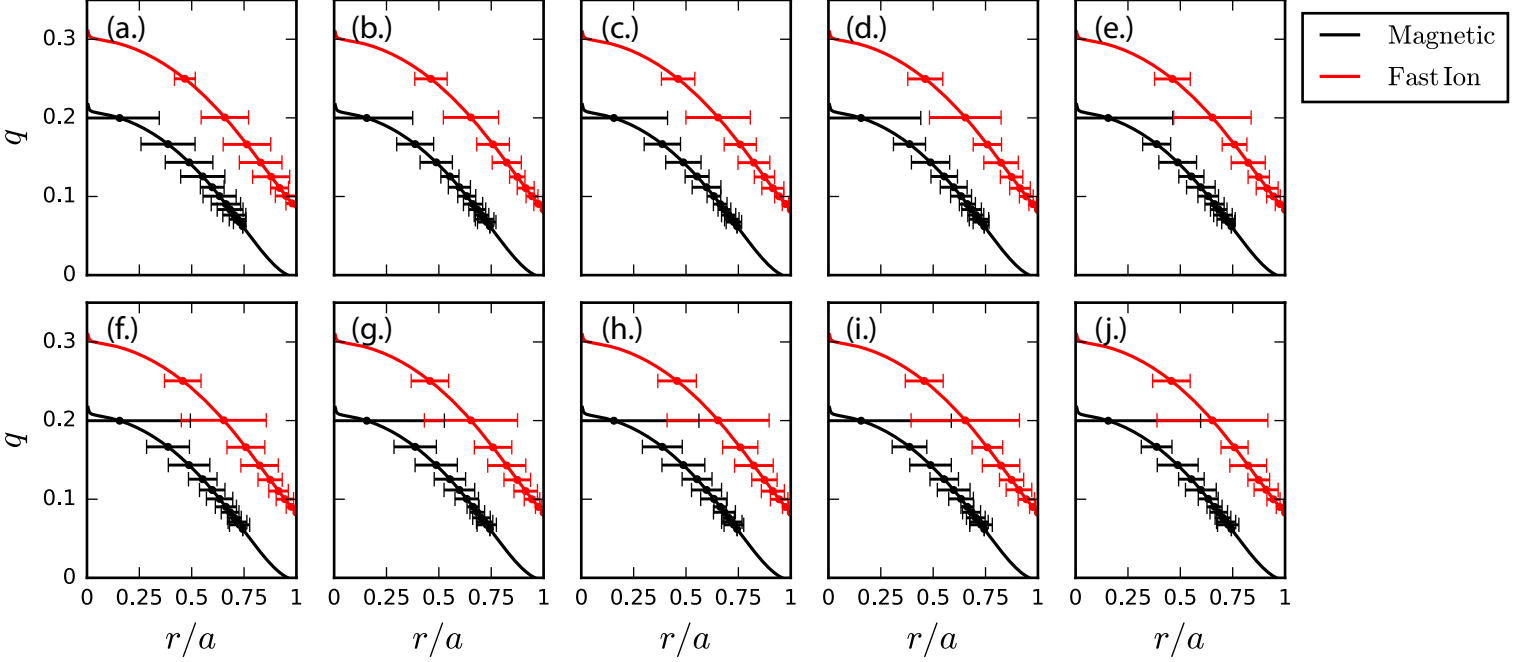
Figure 48: The magnetic safety factor (black) and fast ion safety factor (red) with their corresponding island resonances produced from ORBIT equilibria and perturbations. Subplots (a.)-(j.) have $\tilde{b}_5/|B|$ of 0.8, 1.8, 2.4, 3.0, 3.5, 4.3, 5.2, 6.2, 6.9, 7.3%, respectively.

Going back to Figure 48, the growth in the $n = 5$ island is clearly present. Even though the fast ion resonance is displaced from the maximum in the $\tilde{b}_{5,r}$ profile, it still experiences large enough perturbations to produce significant island overlap. In the MH state, the $n = 5$ fast ion island stretches a relatively narrow region. As the helical perturbation grows, however, the island starts to reach deeper into the core and edge. In the QSH regime, the island overlaps nearly all of the subdominant fast ion resonances. It looks as if the fast ions, at least in regards to the $n = 5$ fast ion island, meet the conditions necessary to follow Rechester-Rosenbluth diffusion.

Rechester and Rosenbluth defined the stochasticity parameter, s, in equation 3.13.[112] The stochasticity parameter provides a metric to define the overlap between two neighboring resonances, (m, n) and (m', n'), based on their locations, r, and island widths,

w.

$$s = \frac{1}{2} \frac{w_{m,n} + w_{m',n'}}{|r_{m,n} - r_{m',n'}|} \tag{3.13}$$

Originally, s was meant to describe the magnetic stochasticity. By substituting the fast ion islands widths and the fast ion resonance locations, an equivalent fast ion stochasticity parameter can be found. Using the fast ion resonances from Figure 48, Figures 49 and 50 were produced. At high-values, $s >> 1$, the overlap among resonances is
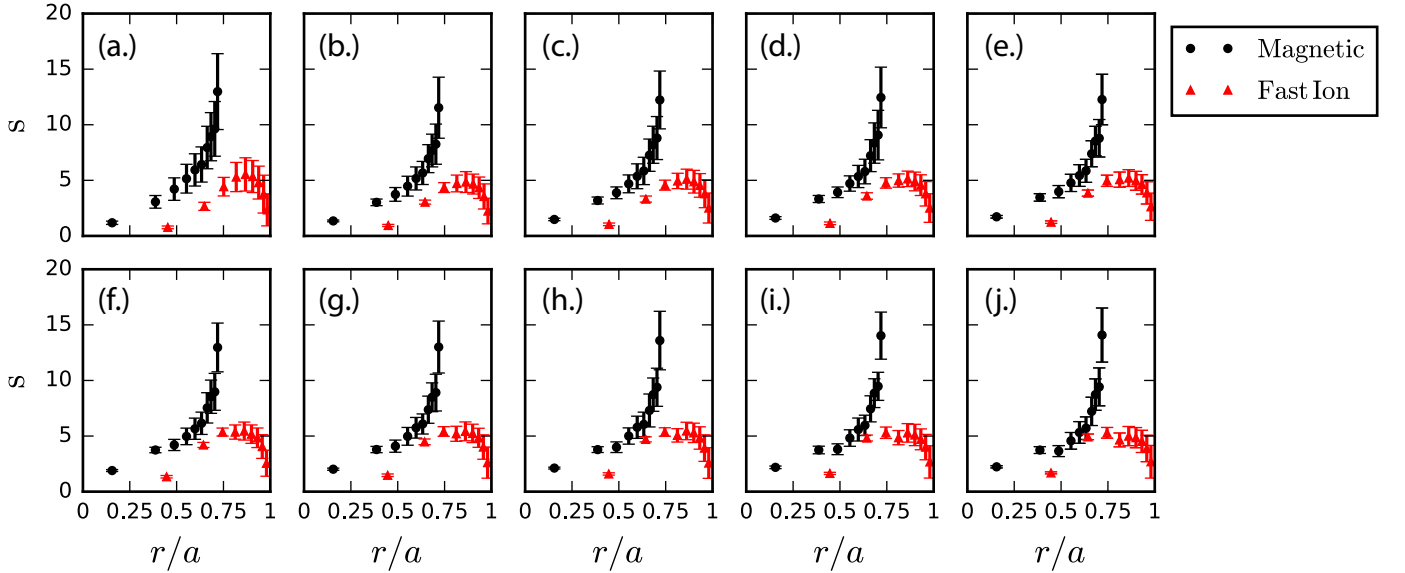
Figure 49: The magnetic stochasticity parameter (black) and fast ion stochasticity parameter (red) from the resonances in Figure 48.

sufficient to cause stochastic diffusion. Particles will wander across the island overlaps and diffuse radially outward as the overlap becomes more severe. For the case of the magnetics, the MH state is in good agreement with past results.[30] The $n = 5$ magnetic resonance does not increase too much because it only neighbors one other resonance. The magnetic $n = 6$ location experiences a small rise in stochasticity following a growth in $w_{1,5}$, but, overall, the magnetic stochasticity worsens with increasing radius due to
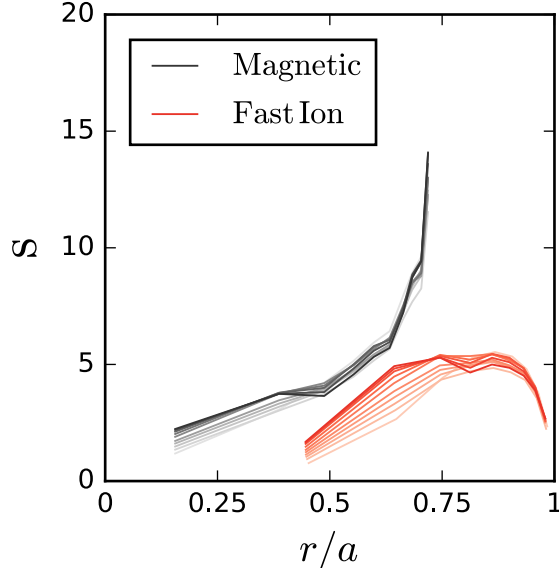
Figure 50: The magnetic stochasticity parameter (black) and fast ion stochasticity parameter (red) from all parts of Figure 49. The transition from light colored curves to darker curves corresponds to growth in the helical perturbation.

the severe overlap.

The fast ion case is quite different. Originally, s is below the magnetic stochasticity. The $n = 5$ fast ion resonance approaches the level of the magnetic stochasticity as the $n = 5$ tearing mode grows in amplitude. The edge fast ion resonances turn downward because the fast ion island widths become quite small at higher mode number. One should also note that the stochasticity parameter is only defined at the resonant locations and fails to graphically represent the extent of the island widths. For example, Figure 48 describes a core region free of any fast ion stochasticity, but the Poincaré plots in the previous section clearly show that this is not true.

Rechester and Rosenbluth found that the radial displacement of a particle in a regime of destroyed magnetic surfaces can be described by the diffusion coefficient in equation 3.14 where R_{cor} is the magnetic correlation length, v is the particle velocity, and the

magnetic values are found at the resonant locations, $q = m/n$.

$$D_{\text{RR}} = \pi R_{\text{cor}} v \sum_{m,n} \frac{\tilde{b}_r^2}{B_\phi^2} \delta(m - nq) \tag{3.14}$$

The Rechester-Rosenbluth diffusion, given in the above equation, was found for the fast ions upon substitution of the fast ion velocity and resonant locations. In MST, the magnetic correlation length is of order 1 m. [113, 114] This was assumed to hold for the fast ion phase-space and a value of unity was used in the calculations. In addition, the actual fast ion diffusion was calculated in ORBIT by examining the average radial displacement, $< \Delta r >$, across the total path, L, following equation 3.15.

$$D_{\text{ORBIT}} \approx v_{fi} \frac{< \Delta r^2 >}{2L} \tag{3.15}$$

This was inspired from the work done by Biewer *et al.* on electron heat transport in reference [30].

25 keV deuterium ions were initially placed at the $n = 5$ fast ion resonance with unity pitch. The resulting particle motion was analyzed for a time period of 2000 toroidal transits, or until the particle was lost, with collisions turned off. This was repeated for varying $n = 5$ tearing mode strengths. The results for D_{RR} and D_{ORBIT} are shown in Figure 51. An ad-hoc estimate of the fast ion diffusion calculated from the confinement time measurements, $D_{\text{exp}} \sim a^2/\tau_{fi}$, was also included along with a general diffusion term that scales linearly with $\tilde{b}_5$.

The Rechester-Rosenbluth diffusion scales, by definition, with $\tilde{b}^2$. This key feature
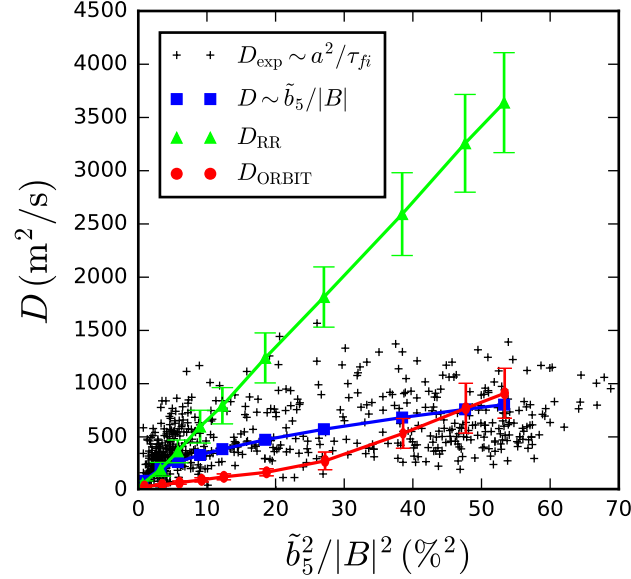
Figure 51: Fast ion diffusivity relative to the core-resonant amplitude based on a Rechester-Rosenbluth scaling (green), ORBIT calculations (red), fast ion confinement time measurements (black), and a linear scaling with $\tilde{b}_5$ (blue).

allows for quick identification of the transport. The τ_{fi} measurements and ORBIT calculated diffusion, however, do not scale as $\tilde{b}^2$. Instead, they appear to follow a scaling that goes as $\tilde{b} \sim w_{fi}^2$. The fast ions do not strictly follow Rechester-Rosenbluth like transport but, rather, a diffusion with a characteristic step size on order of the core-resonant fast ion guiding-center island width. The $n = 5$ tearing mode, however, should be considered a part of the equilibrium in the QSH state where the subdominant modes provide the majority of the stochasticity. In this regard, Figure 51 presents an incomplete picture of the fast ion stochasticity.

Figure 52 demonstrates the diffusivity for a QSH state $(\tilde{b}_5/|B| \sim 7.3\%)$ while varying the subdominant tearing mode amplitudes in ORBIT relative to their experimental values. The D_{ORBIT} values were calculated from the 25 keV deuterium confinement time calculations from Figure 41 via $D_{\text{ORBIT}} = a^2/\tau_{fi}$. The green line represents the
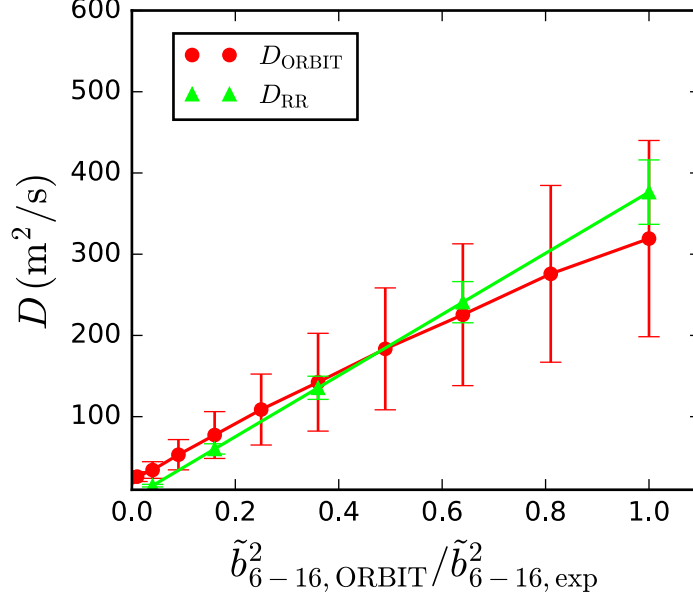
Figure 52: Fast ion diffusivity as a function of scaled subdominant mode amplitudes for a QSH state with a helical perturbation strength of 7.3% showing Rechester-Rosenbluth scaling (green) and ORBIT calculations (red).

theoretical scaling of equation 3.14 minus the (1,5) contribution. The ORBIT calculated diffusivity is approximately linear with $\tilde{b}^2$, matching the Rechester-Rosenbluth scaling. Thus, the transition from a MH to QSH state is a combination of transport associated with the large $n = 5$ fast ion guiding-center island and phase-space stochasticity governed by the subdominant tearing modes.

3.11   Summary

ANPA signals, neutron measurements, and ORBIT simulations all indicate drastic fast ion losses in the transition to the QSH state. The growth in the core-resonant fast ion island coupled with the subdominant modes translates to an increase in the fast ion phase-space stochasticity and enhanced transport. The associated diffusion does not

strictly follow Rechester-Rosenbluth scaling at all helical perturbation strengths and, instead, scales with a step-size characteristic of the $n = 5$ fast ion guiding-center island width. The large $n = 5$ island provides a wide radial width over which fast ions can travel. Coupled with the subdominant modes at the edge, the previously well-defined fast ion phase-space surfaces are destroyed. Ultimately, fast ions are transported across the $n = 5$ fast ion island and experience subdominant mode overlap that spoils the good confinement observed in the MH state.

Chapter 4

Energetic Particle Instability Induced Transport

4.1 Motivation

Energetic particle driven instabilities are known to cause resonant transport of fast ions.[1] In this chapter, a series of observations about bursting mode activity in the QSH state (particularly in the transition to the QSH state) are presented. These include experimental observations of mode frequency shifting and mode splitting into two branches (for one beam isotope), studies of the spatial mode localization via density fluctuations, and the QSH phase with respect to NBI deposition. A look at mode drive and damping is used to probe the main observation which is the vanishing of energetic particle instabilities during strong QSH. This does not necessarily imply that mode-resonant transport is unimportant. The dearth of MHD activity is from reduced drive due to orbit losses (previous chapter's results). Moving forward, there are some reasons to believe a next step RFP may have suppressed residual tearing modes, and the sharp effect of these on fast ions may disappear.[16] In that case, do we need to worry about energetic particle instability induced transport? This work, with other recent work, suggests that mode-resonant transport is not a main concern for fast ion confinement in the helical RFP.

4.2   The Shear-Alfvén Continuum

The conductive nature of plasmas allows particles to couple to electric and magnetic fields. Plasmas can contain a large number of electromagnetic modes that can result in particle motion described as wave phenomena. Compressional and transverse electromagnetic waves propagate in an idal MHD plasma.[28, 68] Linearizing the MHD equations, the shear-Alfvén wave dispersion relation is:

$$\omega = k_\parallel v_A \tag{4.1}$$

where $k_\parallel$ is the wave vector parallel to the magnetic field and $v_A = \frac{B}{\sqrt{\mu_0 n_i m_i}}$ defines the Alfvén velocity where $n_i m_i$ is the plasma mass density and B is the equilibrium magnetic field strength. Waves that satisfy equation 4.1 constitute the shear-Alfvén continuum. The perturbed magnetic field and velocity will always be perpendicular to the equilibrium magnetic field and wave vector for this transverse wave. The mode produces no density or pressure fluctuations because it is incompressible, so only the magnetic tension provides the restoring force to the wave. A physical analogy for shear-Alfvén waves are the waves produced from a plucked string, commonly studied in introductory mechanics courses. The frequency for a standing wave on a string depends on the tension and linear mass density. In the current scenario, the magnetic field provides the tension and the plasma ions provide the inertial mass. In regards to toroidal confinement devices, however, the shear-Alfvén waves travel along toroidal surfaces. In this case, a more precise analogy would be that of waves on the surface of a struck drum head.

This chapter focuses on energetic particles interacting with the shear-Alfvén continuum.[1] The shear-Alfvén wave is a stable mode but can be driven to instability from an

energetic particle population. Neutral beams, ion-cyclotron accelerated fast ions, alpha particles from-DT fusion reactions, and high energy electrons from electron-cyclotron heating have all driven shear-Alfvén waves unstable.[115] Energetic particles can drive modes to instability only when the following exist:

1. $\vec{v} \cdot \vec{E} \neq 0$ for power transfer

2. Resonance between the wave and particles

3. An available free energy source

The energetic particle's drift velocity satisfies the first requirement. Due to the Lorentz transformation of the electromagnetic fields, a particle traveling along a transverse wave at its phase velocity will lie in a reference frame with a static magnetic perturbation and no electric field. Therefore, the only contributions to the power transfer will be from the guiding-center drifts. The transverse electric field component, $\vec{E}_\perp$, dominates the power transfer for a shear-Alfvén wave. The phase-averaged quantity of the power transfer, $\oint \vec{v}_d \cdot \vec{E}_\perp \neq 0$, must be non-zero over many orbital cycles in order for particles to transfer energy to the wave. This relation leads to a direct satisfaction of the second condition above.

$\vec{v}_d$ and $\vec{E}_\perp$ can be written as Fourier series in terms of the poloidal and toroidal coordinates θ and ϕ, respectively. In doing so, the power transfer relation, $\oint \vec{v}_d \cdot \vec{E}_\perp$, transforms to equation 4.2.

$$\omega \approx (n+j)\omega_\phi - (m+l)\omega_\theta \tag{4.2}$$

Equation 4.2 defines the resonance condition between a shear-Alfvén wave of frequency ω with a particle that has a frequency of poloidal motion, ω_θ, and frequency of toroidal

motion, ω_ϕ, where n and m represent the toroidal and poloidal mode numbers of the wave and l and j are non-zero constant integers. The integers l and j derive from the poloidal and toroidal drift contributions of the particle guiding-center velocity, respectively. Both integers become important for the RFP where the drifts are strongly non-radial. To date, literature does not include the toroidal drift contribution, j. In many devices, such as the tokamak, the toroidal drift term is negligible, but this does not hold for the RFP.

Lastly, the free energy contained in an energetic particle distribution function may satisfy the third condition. Similar to Landau damping, the instability drive term originates from a gradient in the fast particle distribution. Particles above the resonant velocity supply energy to the wave, while particles below the resonant velocity take energy from the wave. In the case of the shear-Alfvén wave, the resonant velocity is simply v_A. Therefore, in order to drive the wave to instability, a monotonically increasing function with respect to a coordinate defining the resonance is necessary. Energetic particle distributions typically decrease with energy $(df/dE < 0)$, so the energy or velocity distributions usually dampen the wave. Instead, the drive comes from the spatial gradient. In regards to MST, the NBI produces a strong core-population of fast ions that falls with increasing radius, establishing a gradient suitable to destabilize.

These basic interactions of energetic particles and the shear-Alfvén continuum are general and applicable to any confinement scheme. The next section will describe the energetic particle driven instabilities in more detail. In particular, two types of modes are capable of excitation: those that lie directly on the continuum and those that lie in gaps.

4.3 Alfvén Eigenmodes and Energetic Particle Modes

Shear-Alfvén waves are dispersionless in a homogenous plasma with a constant, uniform magnetic field. All toroidal confinement devices have magnetic shear which results in a radially non-uniform parallel wave vector and introduce dispersion. Since the continuum frequency strongly varies with radius, a shear-Alfvén wave with any radial extent will rapidly disperse. One can imagine a wave packet where its finite size will result in its wavelets traveling at different speeds and destroying (i.e. dispersing) the packet. The damping rate associated with the dispersion is proportional to the variation of the phase velocity, $\frac{d}{dr}(k_\parallel v_A)$, demonstrating how strong magnetic shear leads to considerable damping of the wave. While other damping mechanisms exist, this continuum damping is among the strongest. Modes outside the continuum, however, do not encounter this strong damping effect and may easily be excited.

Gap modes lie off of the Alfvén continuum and allow for marginally stable, discrete eigenmodes to exist that require little drive for destabilization. Gap modes exist in many wave phenomena such as the electron band gap in semiconductors and interference structures from Bragg reflection. In these examples, periodic variations of the index of refraction create the band gaps. In a toroidal confinement device, periodic variations in the magnetic field strength, and thus v_A, represent a modulation of the plasma's index of refraction, creating gaps in the Alfvén continuum. The modulation of v_A can occur for a multitude of reasons: curvature of the field lines, plasma elongation or triangularity of flux surfaces, helicity, mirror effects, and more. The resultant gap modes take on many names and exist in many forms but generally fall into two groups of classification. The first originate due to extrema in the continuum, and the second result from multi-wave

coupling.

Extremum modes exist in a narrow region where $\frac{d\omega}{dr} \sim 0$. This establishes a localized area where the continuum damping is vanishingly small, so the modes require little energetic particle drive for destabilization. Common examples include the reverse-shear Alfvén eigenmode (RSAE), global Alfvén eigenmode (GAE), and beta-induced Alfvén eigenmode (BAE)[116–118]. All of these modes occur in regions near extremum in the Alfvén continuum.

The second classification of gap modes occurs when counter-propagating waves frequency match. The most common example is the toroidicity-induced Alfvén eigenmode (TAE) which has been shown to cause drastic transport of energetic particles.[119, 120] The TAE is associated with the frequency crossing of waves with the same toroidal mode number, n, but with poloidal mode numbers that vary by one, i.e. m and $m + 1$. The toroidal coupling of the modes eliminates the frequency crossing and establishes a gap, or break, in the continuum. The ellipticity-induced Alfvén eigenmode (EAE) and the helicity-induced Alfvén eigenmode (HAE) are examples of more gap modes.[121, 122] There exist a large number of gap modes all with different properties and origins. Their key similarity, though, is that they are all weakly-damped modes that exist off the continuum.

When the energetic particle pressure becomes comparable to the thermal plasma pressure, the fast particle distribution function may drive modes unstable directly on the continuum. Gap modes can be excited in the absence of energetic particles, such as with an external antennae, but energetic particle modes (EPMs) require a drive from a large fast ion population. While the EPM frequency lies on the shear-Alfvén continuum, the dispersion relation depends strongly on the energetic particle distribution, unlike

the gap modes which are sensitive to perturbations in v_A. That is, the energetic particle distribution itself governs both the real and imaginary EPM frequencies.

EPMs are commonly observed with powerful NBI. Introduced earlier, NBI on MST produces super-Alfvénic fast ions, allowing for the resonance condition to be satisfied. Coupled with the good confinement properties of fast ions in the standard RFP, a large fast ion pressure capable of exciting both gap and continuum modes exists.

4.4　Energetic Particle Instabilities in the Standard RFP

The dispersion relation for the shear-Alfvén wave (equation 4.1) can be easily solved for the standard RFP. Decomposing the wave vector in toroidal and poloidal mode numbers and using the definition of the safety factor, the parallel wave vector is:

$$k_\parallel = \frac{m - nq}{r} \frac{B_\theta}{|B|} \tag{4.3}$$

An example Alfvén continuum for $n = 4$, 5, and 6 (with multiple m values) modes in MST ($I_p = 300\,\text{kA}$, $n_e \sim 0.75 \times 10^{13}\,\text{cm}^{-3}, F = 0$) is shown below in Figure 53 (a.). Realistically, any mode numbers will produce a corresponding continuum via equation 4.3. Often the case in MST, though, only the resonant modes near the core are excited due to the fast ion population being strongest in the core. The core fast ion content is able to provide sufficient drive and satisfy the resonance condition (eqn. 4.2).

A distinct TAE gap is apparent for each n. In MST, the TAE gap typically lives around several hundred kHz in frequency and may move radially depending on the mode
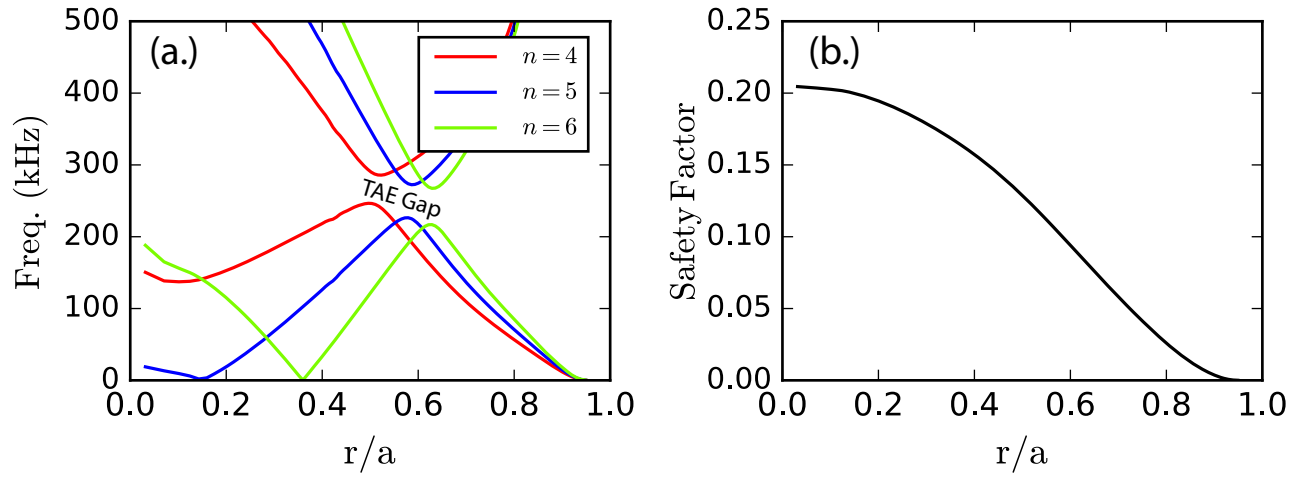
Figure 53: An example shear-Alfvén continuum in MST with $I_p = 300\,\mathrm{kA}$, $n_e \sim 0.75 \times 10^{13}\,\mathrm{cm}^{-3}$, and $F = 0$ for $n = 4, 5, 6$ mode numbers, (a.), and the corresponding q-profile, (b.).

numbers considered and structure of the q-profile. To date, excitation of the TAE mode in MST has never been observed. Other gap modes and EPMs, however, are readily destabilized in a very reproducible manner.[123]

Examples of beam-driven instabilities on MST are shown in Figure 54 for hydrogen fueled NBI at full power. Please note, this example shot is consistent with the Alfvén continuum and q-profile shown in Figure 53. The excitation of $n = 4$ and $n = 5$ Alfvén modes respectively present themselves as 120-240 kHz and 60-120 kHz, $\sim 50\,\mu$s bursts of magnetic activity. The 10-30 kHz, low frequency signals present throughout the shot are the tearing modes, and the large, broadband spikes correspond to the sawtooth crashes. The spectrograms are produced from wavelet analysis on the Fourier-decomposed edge magnetic coil signals.[124] The wavelet analysis occurs over a relatively narrow time window in order to temporally resolve the bursts. Consequently, following from the uncertainty principle, a decomposed burst will possess a frequency width around 80-90

Figure 54: A standard MST discharge with hydrogen NBI showing: (a.) plasma current and NBI power (b.) electron density and D_α emission (c.) tearing mode amplitudes (d.) $n = 4$ wavelet spectrogram showing AE mode excitation (e.) $n = 5$ wavelet spectrogram showing EPM mode excitation. This shot is consistent with the Alfvén continuum in Figure 53.

kHz.[19]

Standard RFP plasmas typically rotate with a velocity given by the core-most resonant tearing mode since the tearing modes are stationary in the plasma frame. The measurements from the edge coils, and the resulting spectrograms, occur in the stationary lab frame. Therefore, in order to achieve the actual mode frequency, it is necessary to correct for the plasma rotation produced Doppler shift. Equation 4.4 gives a mathematical description of the mode frequency, f_{mode} in terms of the measured frequency, f_{meas}, and Doppler frequency, f_{dopp}, where n is the toroidal mode number and $v_{n,\phi}$ is the toroidal plasma velocity.[125]

$$f_{meas} = f_{mode} + f_{dopp} = f_{mode} + \frac{n v_{n,\phi}}{2\pi R_0} \tag{4.4}$$

Care must always be taken to apply this Doppler correction when comparing measured frequencies to theory and simulation. All measurements presented in this thesis, with the exception of Figure 54, include the Doppler correction.

Koliner *et al.* showed that the $n = 4$ modes are Alfvénic, i.e. gap modes, while the $n = 5$ modes respond strongly to changes in the beam parameters and thus particle population, i.e. EPMs.[126] Comparing the $n = 4$ frequencies to the corresponding Alfvén continuuum branch in Figure 53, no gaps appear to be present. Recent theoretical and computational work by Cook *et al.* suggest the formation of a gap in the $n = 4$ continuum due to the $n = 5$ magnetic island eccentricity.[127–129] Measured $n = 4$ mode frequencies strongly match this theory, identifying this gap mode as an island induced Alfvén eigenmode (IAE).[130] Of note, the $n = 4$ energetic particle instabilities only present themselves with hydrogen NBI. 25 keV injected deuterium ions only show

$n = 5$ energetic particle activity. The lesser velocity deuterium ions do not resonate as efficiently as the faster hydrogen ions and fail to destabilize the $n = 4$ AEs.

Figure 54 shows that $n = 4$ and $n = 5$ energetic particle instabilities occur roughly one after the other. It has been shown that the $n = 4$, 5 and -1 (not shown) energetic particle driven modes exhibit a strong bicoherence.[131, 132] Figure 55 shows the bursting amplitudes of the modes, their bicoherence, and their associated effects on neutral particle analyzer (NPA) signal and the core-resonant tearing mode. The bursting am-
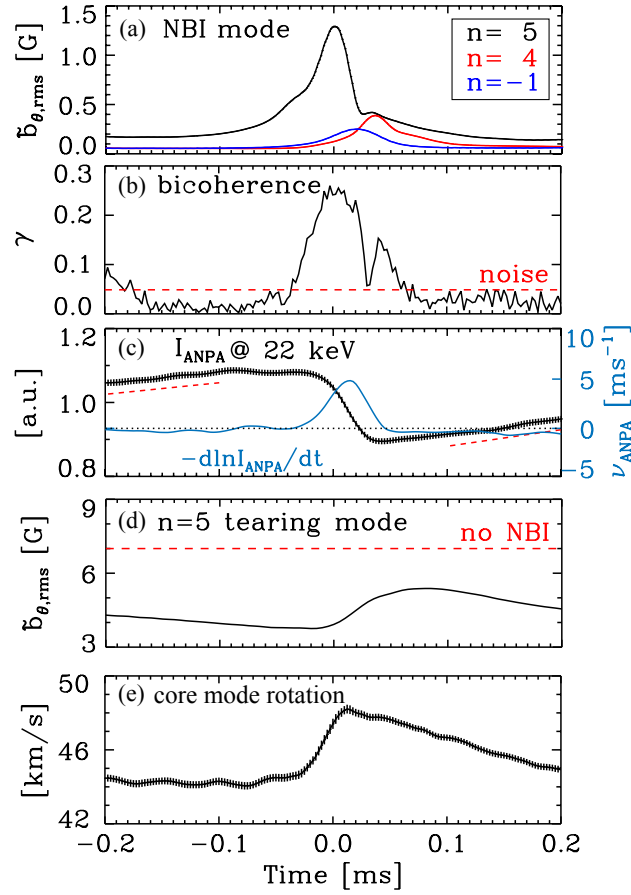
Figure 55: An ensemble average of $n = 5$, 4, and -1 energetic particle instabilities with respect to their bursting time: (a.) their magnetic fluctuation amplitudes (b.) their bicoherence (c.) 22 keV ANPA signal (d.) $n = 5$ tearing mode amplitude (e.) $n = 5$ toroidal velocity. Taken from reference [131].

plitudes were found from the edge magnetics by integrating in frequency space over the bursting frequencies. The current explanation is that the $n = 5$ mode occurs first and results in fast ion transport, creating the bursting nature of the $n = 5$ mode. The $n = 5$ mode redistributes particles which flattens the fast ion spatial gradient and eliminates the driving term. The fast ions scatter out of resonance with the $n = 5$ mode, move radially outward, and trigger the $n = 4$ mode. The $n = -1$ mode is then nonlinearly excited from the $n = 5$ and $n = 4$ modes. The bursting nature of the destabilized modes is characteristic of predator-prey relaxation oscillations consistent with localized fast ion transport.[131]

The redistribution reveals itself in the drop in the NPA signal around the 25 keV fast ion energy and a rise in the $n = 5$ tearing mode strength. The NPA view for this data is tangential and sensitive to high-pitch, co-passing fast ions. D_α measurements indicate that the neutral content remains relatively constant, so the change in NPA signal can be attributed to beam ion loss or redistribution. Discussed in Chapter 3, the fast ions suppress the $n = 5$ tearing mode, so its rise in Figure 55 (d.) also points toward fast ion transport.[70]

Knowing the spatial distribution of fast ions in MST allows for a verification of the spatial gradients necessary to drive energetic particle instabilities. This has proven to be a very difficult measurement to obtain on MST due to a number of experimental limitations. To date, the measurement of DD-fusion produced 2.45 Mev neutrons and 3.01 MeV protons have provided the best picture of the fast ion distribution in standard MST discharges. [56, 110, 133] Measurements with the collimated neutron detector (CiNDe) produced the fast ion beta shown in Figure 56 for a 300 kA $F = 0$ plasma.

Compared to a thermal beta of a few percent, a core value of $\beta_{fi} \sim 7-8\%$ is relatively
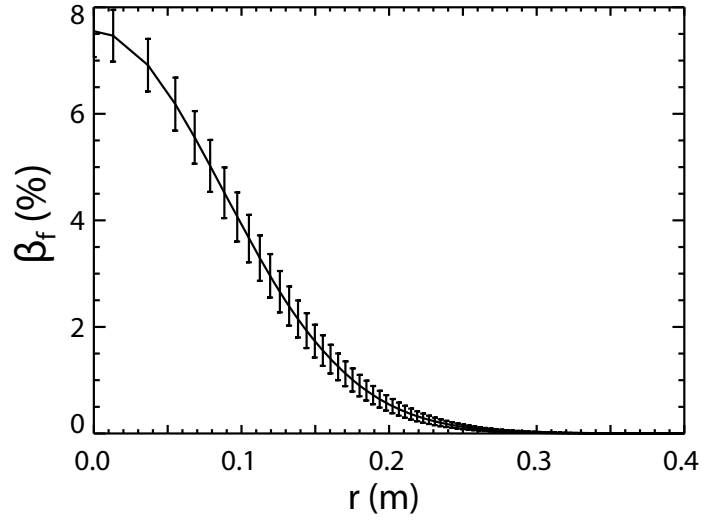
Figure 56: CiNDe measured fast ion beta in 300 kA MST plasmas. Taken from reference [110].

high and speaks to the well-confined nature of fast ions in the standard RFP. Capecchi *et al.* recently performed an in depth analysis of fast ion profile evolution through DD-fusion neutrons in standard, non-reversed MST plasmas and discovered a limit on the marginal stability in the fast ion beta.[110] A model simulated the fast ion density profile subject to NBI sourcing, EPM induced redistribution, and edge fast ion island stochasticity. The calculations defined a critical boundary at which the EPMs dominated fast ion transport inward, near the core, while fast ion phase-space diffusion dominated at large radius (r/a $\gtrsim$ 0.4). The model agreed with experimental measurements of n_{fi}. The combined EPM induced core transport and tearing mode induced edge transport established a saturated core fast ion density which then feeds back onto the EPM drive and tearing mode suppression. Suffice to say, the measurements indicate that EPM induced transport is localised to the core.

All in all, the NBI-heated standard RFP is rife with energetic particle instabilities.

The neutral beam injected ions on MST are capable of providing sufficient drive and resonance to destabilize the shear-Alfvén continuum. The resultant instabilities have been identified as gap modes and EPMs which result in localized transport of the fast ions. The redistribution of the fast ions feeds back onto the spatial fast ion gradient, resulting in the bursting behavior. Importantly, however, this transport is localized to the core region of MST. The bursts themselves result in no global alteration of the fast ion distribution. Thus, at first glance, while the energetic particle instabilities appear to be detrimental toward fast ion confinement, neutron measurements contradict this sentiment and report a rather high fast ion beta.

4.5 Energetic Particle Instabilities in the Helical RFP

The repetitive, reproducible bursting modes in the standard RFP (see Figure 54) are altered in the transition to the helical equilibrium. Figure 57 illustrates a typical high current, hydrogen NBI-heated QSH plasma where the energetic particle driven bursts rise in frequency with increased helical perturbation.

QSH plasmas in MST occur primarily in $F = 0$ discharges with $q(0) > 0.2$ and a core-resonant $m = 1$, $n = 5$ mode. Energetic particle induced magnetic activity with $n = 5$ in a QSH plasma is shown in Figure 57 (d.), while previously observed $n = 4$ activity in axisymetric discharges are not measured. Rather interestingly, the observed $n = 5$ bursting frequencies up-shift in frequency with the growth in the $n = 5$ tearing mode with two examples apparent in this discharge. Another observation is that the bursts disappear when the core-tearing mode amplitude becomes greater than about 7% despite constant particle sourcing by the NBI. These trends are born out in a scan of

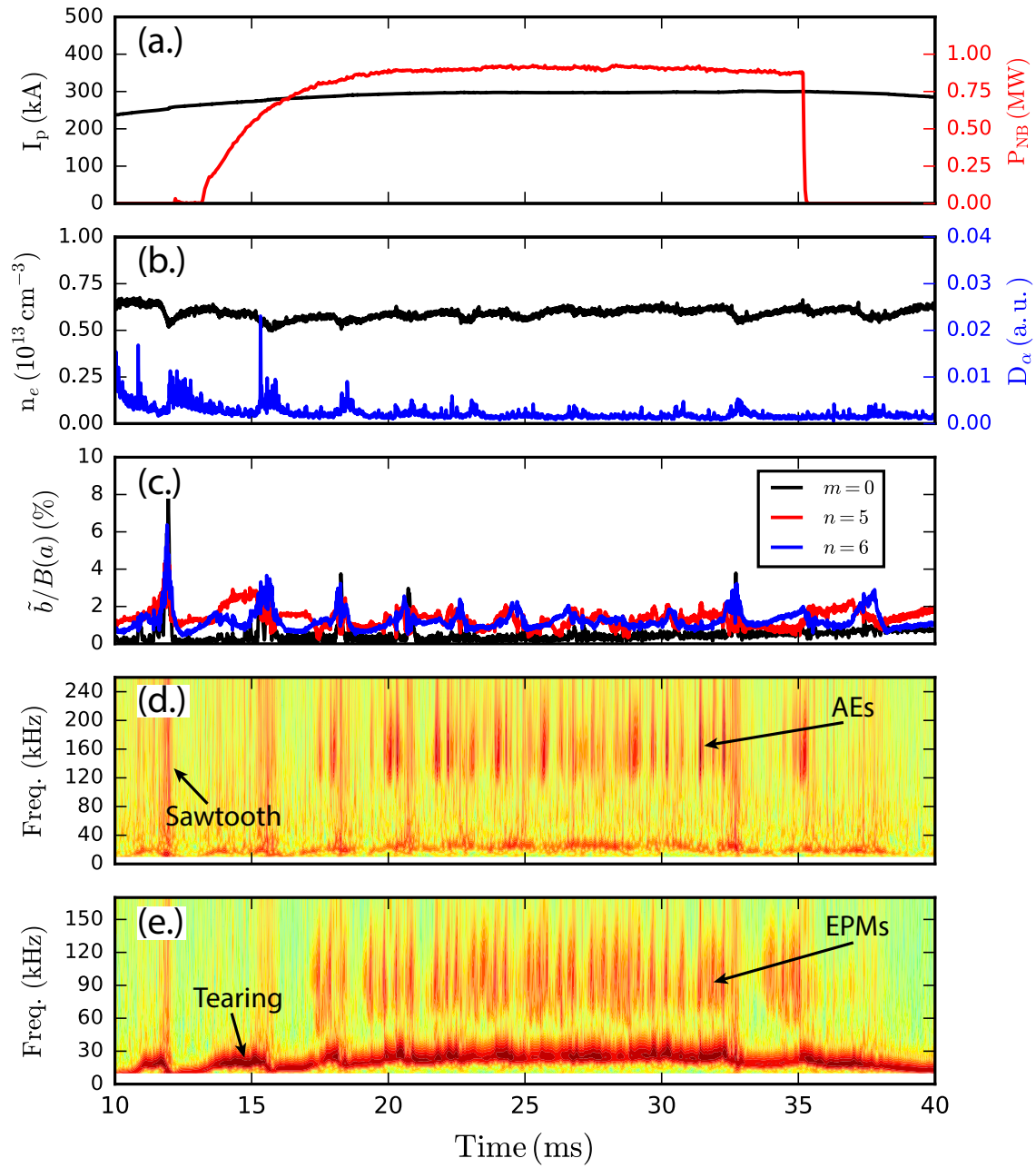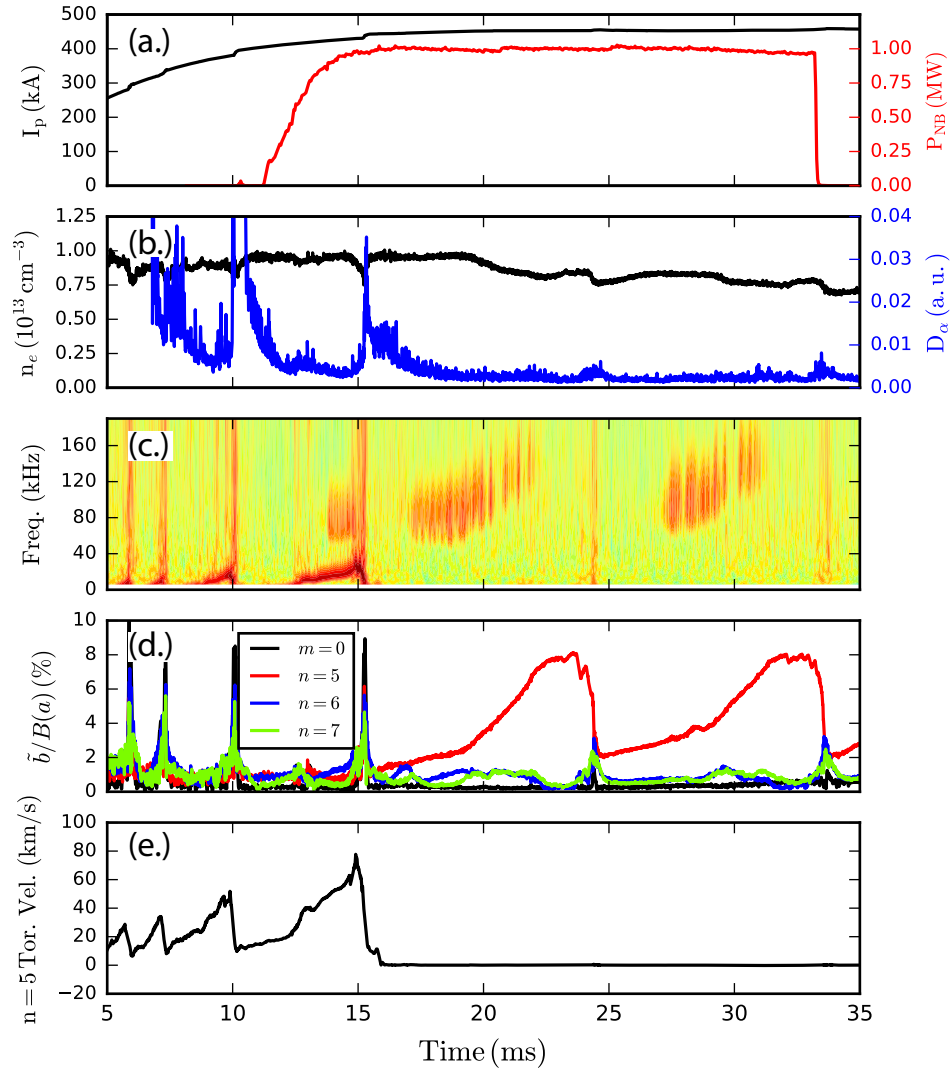Figure 57: A MST discharge with QSH transitions and hydrogen NBI: (a.) plasma current and NBI power (b.) electron density and D_α emission (c.) Doppler corrected $n = 5$ wavelet spectrogram showing energetic particle instabilities (d.) tearing mode amplitudes.

plasma current (keeping other parameters approximately constant) and measuring burst frequencies at all values of normalized helical perturbation strength.

Figure 58 shows the bursting mode frequency response as a function of normalized core tearing mode strength for both hydrogen and deuterium beam species. The burst
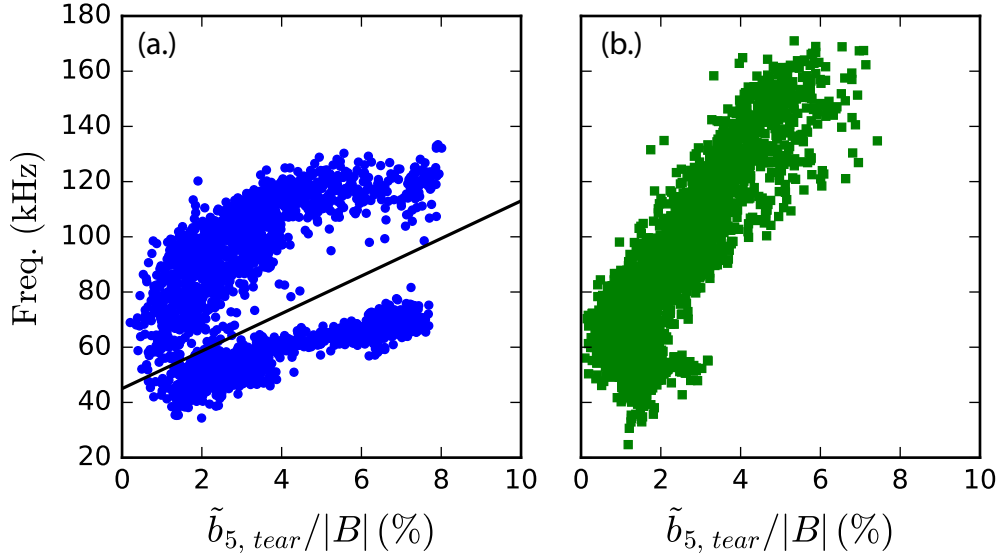
Figure 58: The relationship between normalized core-tearing mode amplitude and energetic particle burst frequency for deuterium, (a.), and hydrogen, (b.), fueled NBI. The black line in (a.) is the fit line determined to separate the low and high frequency deuterium driven bursts.

times and frequencies were found from the wavelet spectrograms by eye. Routines examining the spectrogram as a function of frequency and time were developed to numerically search for localized maxima, but the search algorithms were found to be less accurate than a simple point-and-click scheme. The frequencies of the bursts were taken as the middle of their widths where their amplitudes are greatest. The corresponding helical perturbation strengths were found by matching the time point to the $n = 5$ Fourier decomposed edge magnetics in the tearing mode frequency range.

Figure 58 presents some interesting observations: the well-established connection between burst frequency and core-resonant amplitude, the cessation of bursts at corresponding high amplitude, and the appearance of two frequency branches for deuterium fueled NBI. The deuterium driven bursts were categorized into either the high or low frequency branch by fitting a line between the branches. The disappearance of the bursts is correlated to the core-resonant tearing mode amplitude and not the QSH flat top period. That is, the divergence and saturation of the core-resonant tearing strength only effects the fast ion content at high amplitude. Figure 59 presents a discharge in which the Alfvénic instabilities readily survive a weaker QSH state. Figure 60 offers an example shot with low frequency deuterium bursts for the reader's reference.

Two possible explanations exist for the dearth of bursting modes in strong QSH periods: an increased mode damping or decreased particle drive. It is not an instantaneous bifurcation, Figure 61 shows that bursts gradually weaken with the growth in the helical perturbation. The NBI power remains constant throughout the shots (see Figure 57 (a.) as an example), so the driving mechanism of the modes, the energetic particle distribution, can only decrease if the fast ions become lost or undergo massive redistribution. The tearing mode induced transport of Chapter 3 appears to be the likely culprit but does not speak to resonant mode transport or dampening. The most common damping mechanisms are ion/electron Landau damping, radiative damping, collisional damping with electrons, and continuum damping.[134–137] Landau and collisional damping may be ruled out because the particle distributions in MST are not of the correct structure and the electron-fast ion collisionalities are too low. Radiative damping requires other modes to couple to the Alfvén continuum, so this may also be ignored. A change in
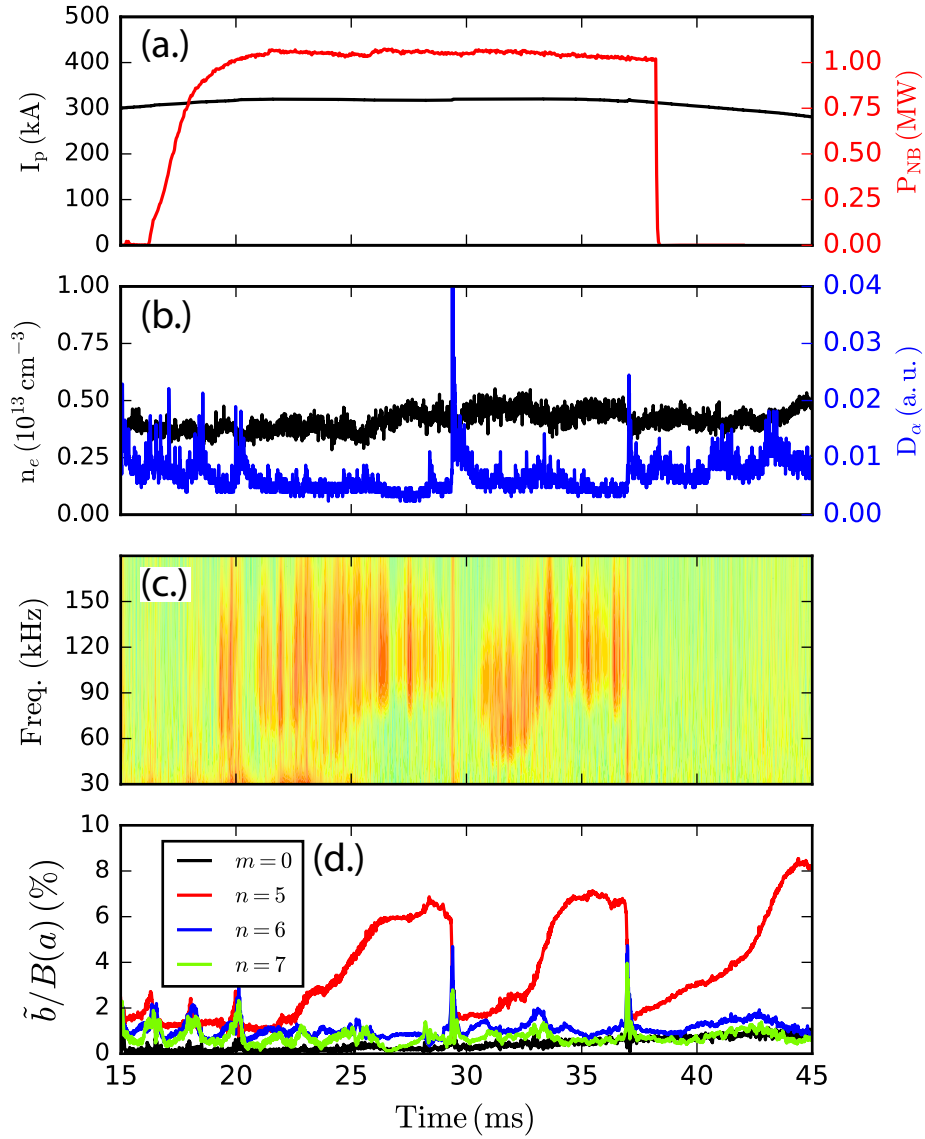
Figure 59: A MST discharge with energetic particle instabilities during QSH saturation: (a.) plasma current and NBI power (b.) electron density and D_α emission (c.) Doppler corrected $n = 5$ wavelet spectrogram showing energetic particle instabilities (d.) tearing mode amplitudes. Note a clear burst at $t = 27$ ms in an established QSH period.
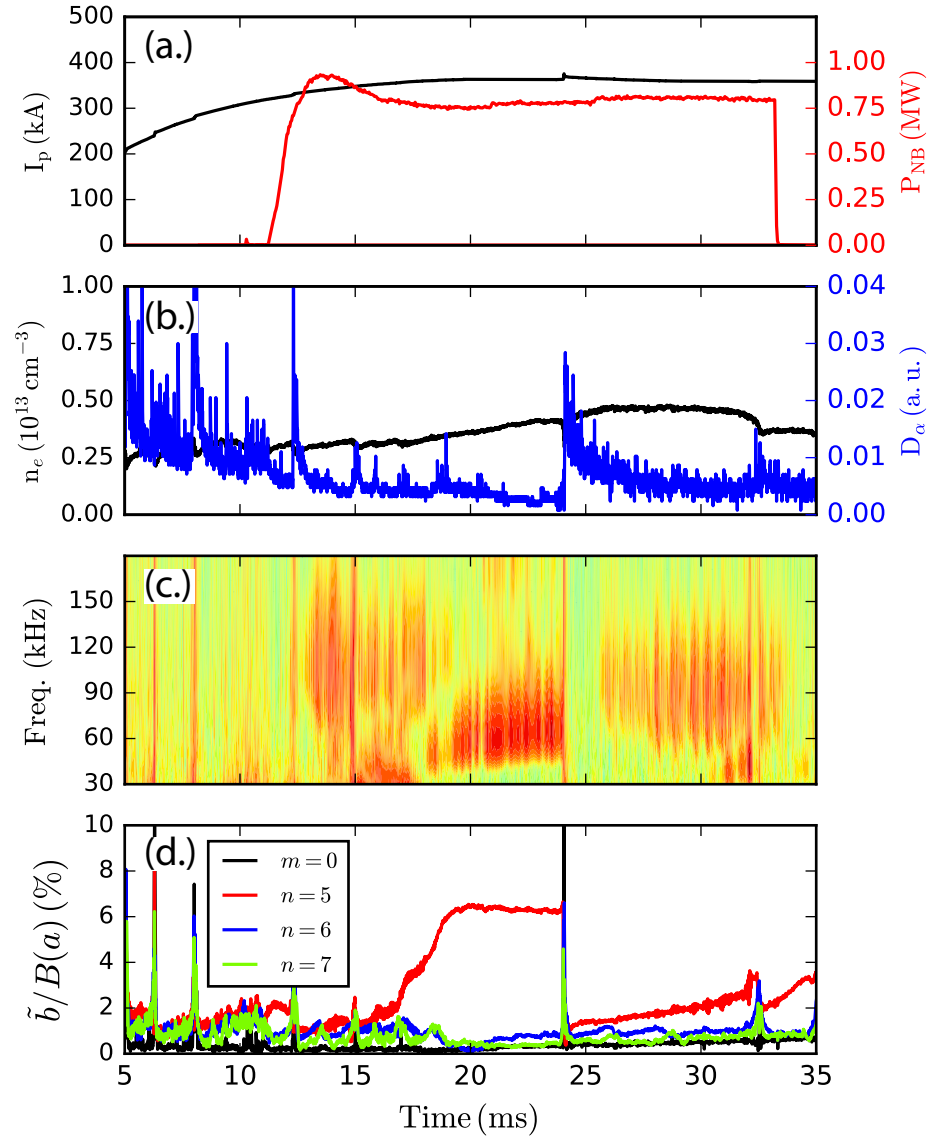
Figure 60: A MST discharge with low frequency deuterium driven bursts: (a.) plasma current and NBI power (b.) electron density and D_α emission (c.) Doppler corrected $n = 5$ wavelet spectrogram showing energetic particle instabilities (d.) tearing mode amplitudes. Note the emergence of low frequency bursts during QSH at $20 < t < 24$ ms.

continuum damping poses the best possibility as a natural outcome of the evolving equilibrium. STELLGAP-computed equilibria as a function of $\tilde{b}_5$ in section 4.8 will show that damping is expected to lower with increased helical perturbation.
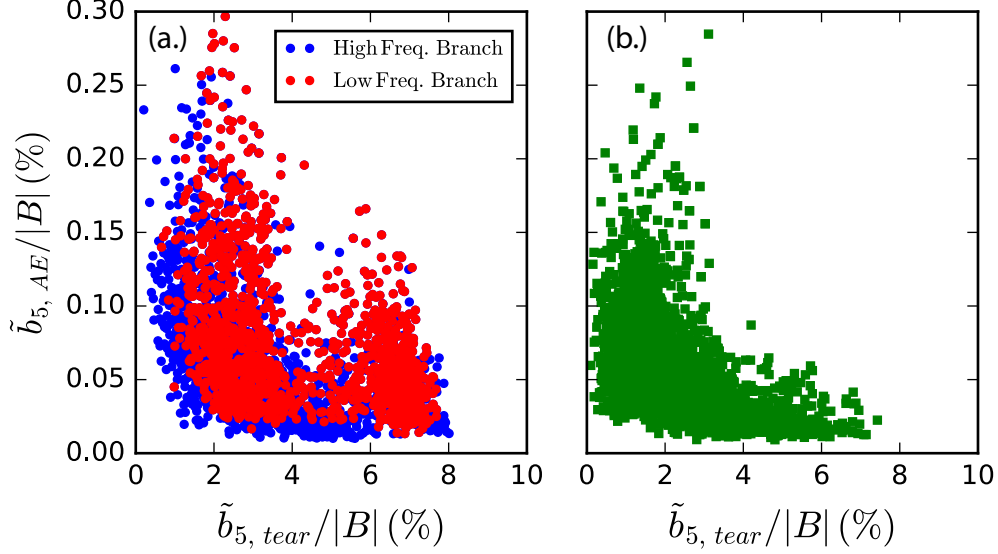
Figure 61: The relationship between normalized core-tearing mode amplitude and energetic particle instability amplitude for deuterium, (a.), and hydrogen, (b.) fueled NBI. The deuterium bursts have been split into the low and high frequency branches from Figure 58.

Figure 62 shows the ensembled average amplitudes of the bursts as a function of time. The deuterium bursts appear symmetric with respect to $t = 0$ indicating equal growth and decay rates. The lower frequency deuterium driven branch has a higher burst amplitude whose cause is discussed later in the chapter. The hydrogen bursts in Figure 62 possess a longer decay time than growth with no explanation. Growth and decay rates were calculated from these ensembles by fitting exponential curves of the form $e^{-t/\tau}$. The growth and decay rates do not substantially deviate from those in the standard RFP.
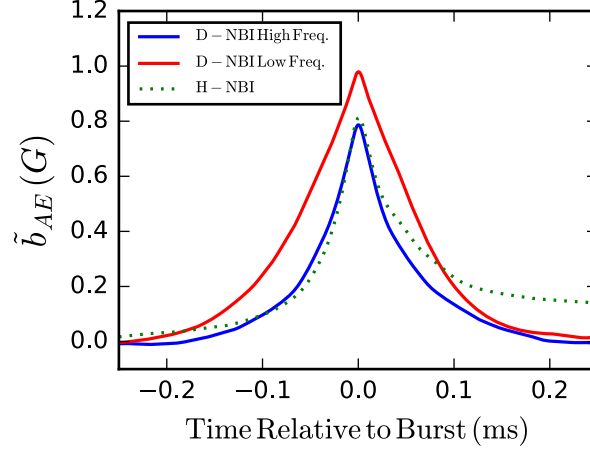
Figure 62: Ensemble average of the deuterium and hydrogen bursting mode amplitudes relative to bursting time. The deuterium bursts have been split into the low and high frequency branches from Figure 58.

4.6   FIR Coherence Measurements

Additional understanding of the mode splitting and frequency upshift is gleaned from a measure of the modes' spatial localization. The 11 chord FIR interferometry system on MST provides spatial measurements of the Alfvén instabilities from correlations between electron density perturbations associated with the wave induced magnetic fluctuations.[132] Each of the 11 chords on the FIR system can provide line integrated density fluctuations across MST's poloidal cross-section. Magnetic induced perturbations associated with the destabilized shear-Alfvén modes can be found from the edge magnetic coils. The spectral coherence between the density and magnetic fluctuation signals can be calculated as:

$$\gamma = \sqrt{\frac{|<\mathcal{F}_{\tilde{b}}\mathcal{F}_{\tilde{n}}>|^2}{<|\mathcal{F}_{\tilde{b}}|^2><|\mathcal{F}_{\tilde{n}}|^2>}} \tag{4.5}$$

where $\mathcal{F}$ represents the associated Fourier transform of the temporal signal and $<>$ denotes an ensemble average over the Alfvénic bursts. This procedure was followed for the thousands of hydrogen and deuterium driven bursts across all of the FIR chords throughout the transition to the helical RFP. The resulting spectral coherences were stitched together to visualize the spatial structure of the modes in frequency space. The mode structures are plotted in Figure 63.
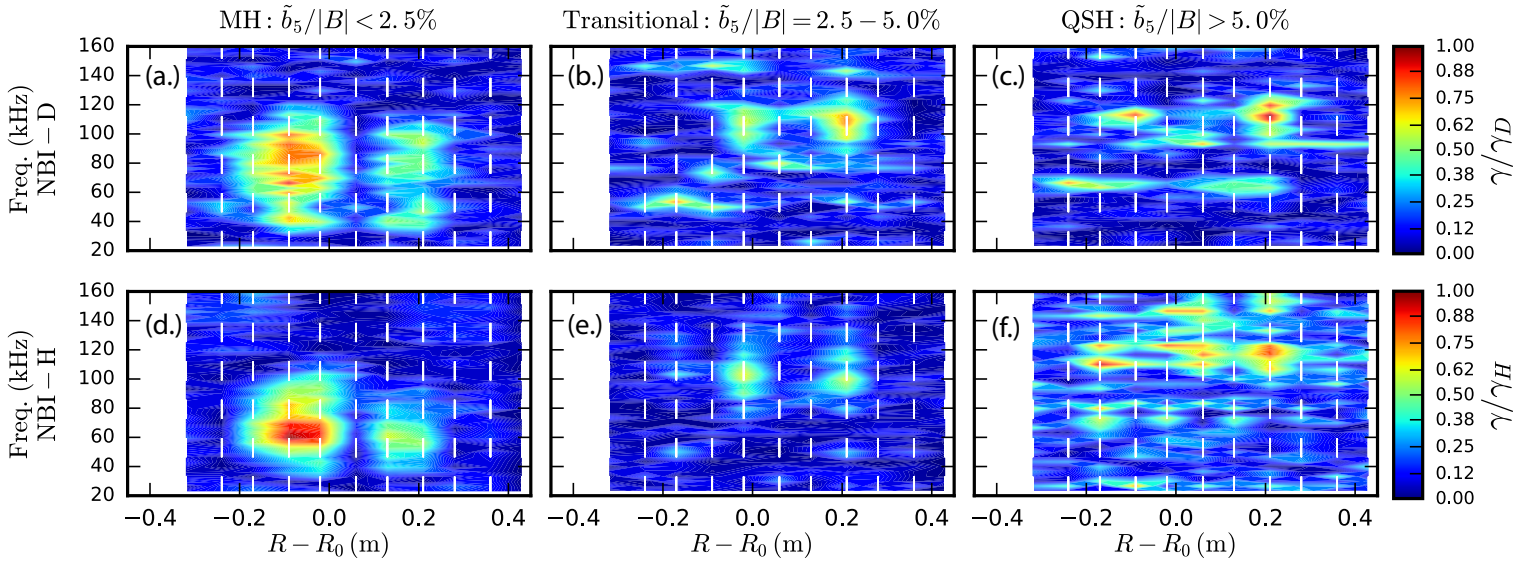
Figure 63: The spectral coherence between electron density perturbations and magnetic flucuations from deuterium driven Alfvén instabilities, (a.) - (c.), and hydrogen driven, (d.) - (f.). The coherences are normalized relative to their maxima of $\gamma_D = 0.25$ and $\gamma_H = 0.32$. Looking from left to right, the associated bursts are ensembled according to normalized core-resonant amplitudes of: $< 2.5\%$, $2.5\% - 5\%$, and $> 5\%$, respectively. The dashed-vertical lines represent the FIR chords.

Figure 63 presents the spectral coherence for hydrogen and deuterium injected fast ions in three topologies: the MH state, a transitional state, and the QSH state. The observed rise in burst frequency with increased helical perturbation strength is again evident, and the deuterium driven bursts display distinct structures for the low and

high frequency branches. Additionally, the coherence structures undergo an outward, radial shift indicative of a strong fast ion population in the newly forming helical axis. In viewing Figure 63, one must take care in the transitional and QSH plots to disassociate $R - R_0 = 0$ as the core. In the right most plots, the plasma has adopted a helical axis that has shifted from the previously axisymmetric magnetic axis. Measurements and simulations have shown that the helical core in MST forms around 14 cm in minor radius, i.e. $R - R_0 = \pm 0.14$.

Figure 63 contains all QSH locking phases which is counterintuitive for a helical core that can lie across different FIR chords depending on the phase. The FIR coherence structures do not move as a function of helical locking phase for either beam species. This was tested by using the RMP to lock the helical core across different FIR chords. This is quite puzzling as one would expect the instabilities to possess the same $m = 1$ poloidal mode structure as their branch on the Alfvén continuum. L. Lin *et al.* observed a similar inboard-outboard asymmetry shown in Figure 63 but gave no explanation for its cause.[132] This is a rather interesting observation that goes against initial expectations, so a break is taken to investigate this further.

4.7 Helical Phase Dependence

No phase dependence was observed in any fast ion measurement made for this work with the exception of the two deuterium bursting mode branches. Figure 64 shows the phases of the recorded bursts as a function of their frequency. RMPs were utilized throughout the various shot days in order to get an even distribution of discharges
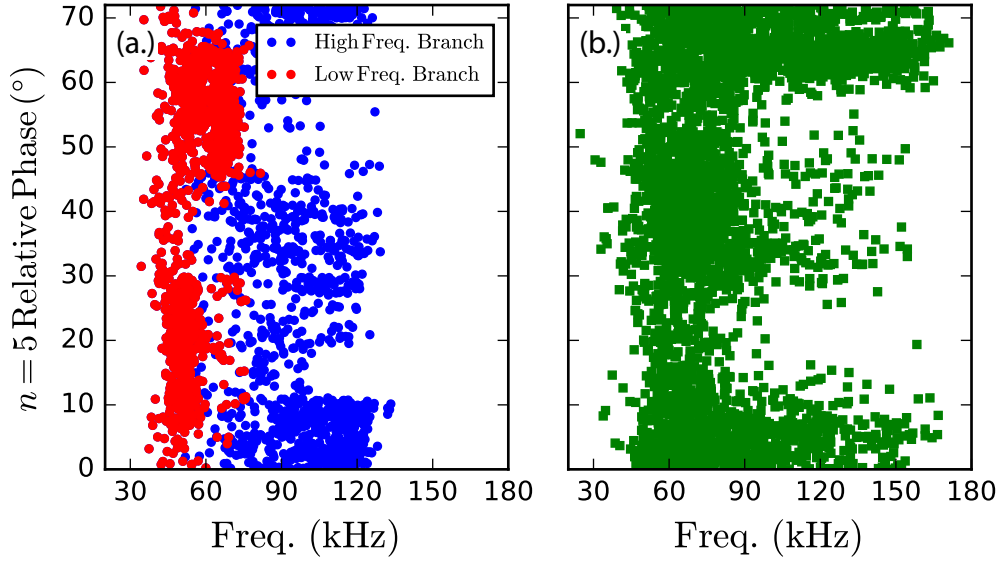
Figure 64: The relationship between burst frequency and plasma phase modulated by the $n = 5$ periodicity (72°) for deuterium, (a.), and hydrogen, (b.), fueled NBI. The deuterium bursts have been split into the low and high frequency branches from Figure 58.

at all phases. The low frequency deuterium driven bursts seem to favor the ranges 10-30° and 45-65° and the high frequency branch prefers the complementing phases. The high frequency branch's phase preference appears to coincide with the hydrogen driven bursts as well. In comparison to other plasma and fast ion signals, however, there appears to be no consequences associated with this phase dependence. Such an example is shown in Figure 65 for the measured fast ion confinement times at high helical perturbation strength. The current hypothesis is that the NBI deposits fast ions across a full QSH period, shown in Figure 66, that washes out or smooths over any fast ion phase dependence. A hypothesis can be made that the phase effect on the mode branches is from some subtle off-axis beam fueling which excites a different region of the Alfvén continuum.
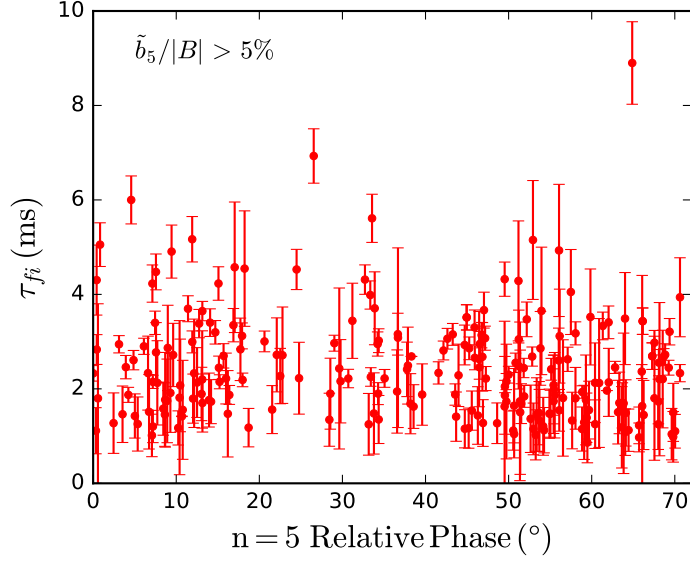
Figure 65: Fast ion confinement time measurements from Figure 39 for $\tilde{b}_5/|B| > 5\%$ as a function of the helical locking phase. Note: The locking phase is in reference to the $n = 5$ periodicity, $360/5 = 72°$. This is an expansion of the dataset presented in reference [99].

A discussion on phase dependence demands the mention of fast ion charge-exchange losses. Recent work on MST has shown that neutral sourcing in QSH plasmas possesses a very strong helical phase dependence.[138] Figure 65 clearly shows that the fast ion confinement is independent of phase, though. Figures 32 and 33 show a sharp cutoff of the ANPA signal below the full energy (25 keV) component and with the transition to QSH. A lack of ANPA signal indicates a lack of charge-exchange losses. If the local neutral density were to increase with the fast ion content remaining relatively constant, then the ANPA signal should also increase. Since the ANPA signal decreases, this indicates that the fast ion loss mechanism is faster than charge-exchange loss. Neutral modeling combined with NBI heating measurements on MST have previously found low neutral densities that result in near zero charge-exchange losses.[67, 139] For all of these reasons, fast ion charge-exchange losses are presumed to be negligible. Never the less,

the establishment of a shifted-helical core closer to the neutral dense edge is a reminder of their possibility.
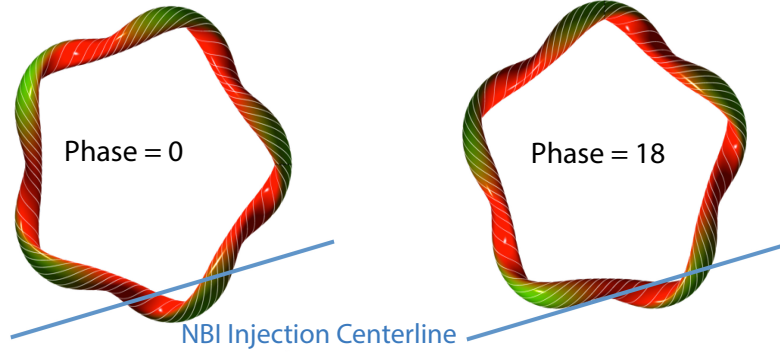
Figure 66: Representations of the NBI injection across two QSH plasma phases. The NBI roughly crosses a full $n = 5$ period.

4.8 The Alfvén Continuum in the Helical RFP

Since the burst frequencies and spatial locations are known, it would be convenient to map our experimental findings onto the theoretical Alfvén continuum. In the helical RFP equations 1.5 and 4.3 no longer apply because they rely on cylindrical approximations and the assumption of axisymmetry. The full calculation of the parallel wave vector needs to be performed in the new 3D-equilibrium in order to determine the correct version of equation 4.1. Analytically, this is a challenging task that would require working in a helical coordinate system with new flux labels.

The shear-Alfvén continuum was calculated with the STELLGAP code across a variety of helical perturbation strengths utilizing 3D-equilibria from VMEC/V3FIT. Figure 67 displays the resultant q-profiles and $n = 5$ Alfvén continua. As the topology transitions from the MH to QSH regime, the q-profile becomes non-monotonic and the
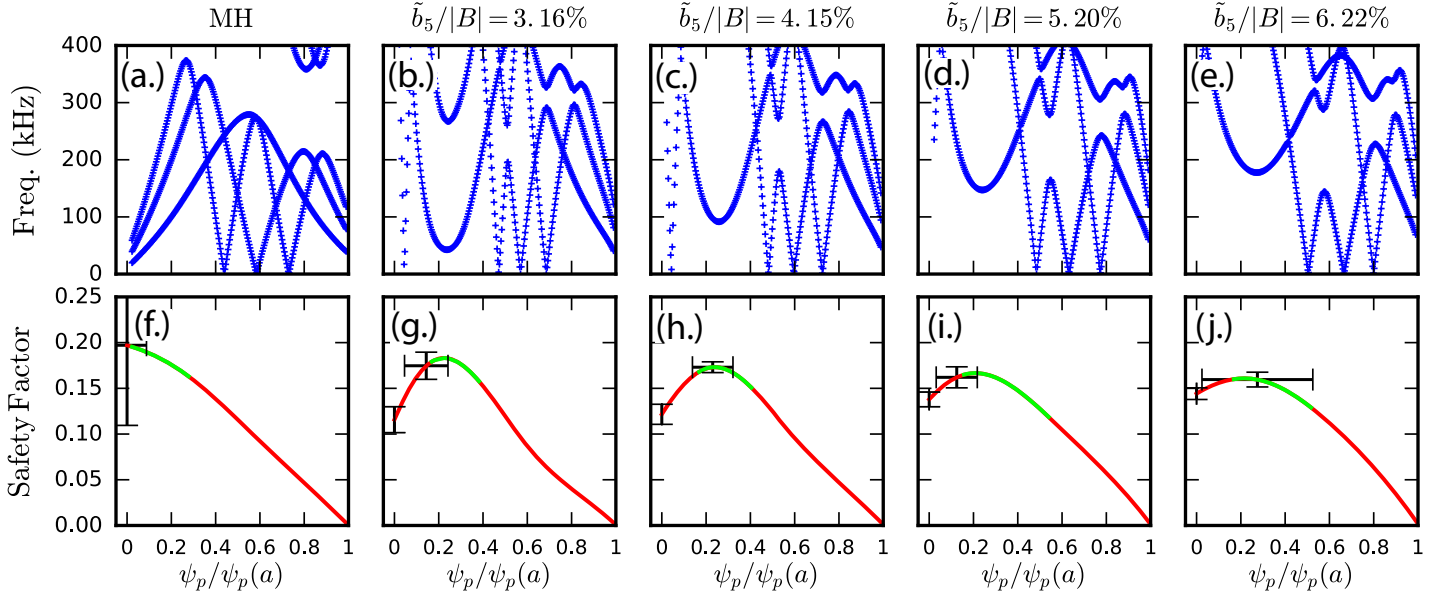
Figure 67: Shear-Alfvén continua, (a.) - (e.), produced from the code STELLGAP and their associated q-profiles, (f.) - (j.), from V3Fit reconstructions. Looking from left to right, the normalized core-resonant strengths are: 1.7%, 3.2%, 4.2%, 5.2%, and 6.2%. (a.) and (f.) denote a standard MH RFP while all others represent varying strengths of QSH. Regions highlighted in green identify the mapped NBI deposition and measured FIR resonance locations.

on-axis value decreases.[85] The Alfvén continuum responds with a branch that forms a local minimum that rises with the corresponding change in q. The error bars indicate that the change in q is valid. The V3Fit reconstruction was generated from the most complete available dataset to minimize fit error.[140] Polarimetry measurements provide a large constraint in the V3Fit reconstructions, but were not used in order to maximize the interferometry laser power. The reproducibility of the shifting burst frequency, though, acts as experimental validation of the reconstructions.

Since STELLGAP works in the poloidal flux coordinate and the FIR operates in physical space, a mapping must be performed to determine where the spatially resolved mode excitations lie on the continuum. The radial locations of the modes were taken from

the measurements in Figure 63 and were assumed to be near the midplane, $Z = 0$. The toroidal locations of the modes were taken as the location of the FIR chords (250° relative to the poloidal gap). The (R, Z, ϕ) coordinates of the FIR measured mode structures were then cast to a given V3Fit reconstruction from which the poloidal flux variable can be inferred. To further narrow the parameter space at which the modes could occur, a simulated NBI deposition based on the beam geometry was similarly cast to the equilibrium construction to estimate the fast ion distribution as a function of poloidal flux. The overlap of the NBI deposition and the FIR measurements was then taken as the locations of the Alfvén instabilities. It should be noted that the phase of the helical equilibria could be freely chosen. The described methodology was performed for various plasma phases in VMEC, and the location of the mode resonances showed no phase-dependence.

The aforementioned continuum calculation was performed for each 3D-equilibrium in Figure 67 (f.) - (j.) with the corresponding energetic particle bursts of Figure 63. Examining the mapped FIR measurements on the STELLGAP continua (green regions), the Alfvénic modes first occur near the core then shift to around 0.2 in units of normalized polodial flux. The evolving 3D-equilibrium alters the Alfvén continuum in such a manner so as to preserve the energetic particle distribution near the core. In reference to Figure 58, this provides an explanation for the observed up-shift in frequency and deuterium branch splitting. The helical evolution translates to an alteration of the q-profile which propagates to the Alfvén continuum. While the helical perturbation grows in strength, the excited branch of the continuum grows in frequency. With NBI deposition strongest in the core, the fast ion spatial gradient and resonance allow the bursts to up-shift in frequency and maintain a region for instability growth throughout the topological

evolution.

Since it is not critical to the main tenants of this dissertation, an exact identification of the Alfvénic instabilities was not carried out. Some interesting observations can be made nonetheless. The minima in the Alfvén continua strongly suggest the possibility of discrete gap modes such as GAEs, RSAEs, or even low frequency BAEs.[1] The continua minima establish regions of near zero continuum damping ($\frac{d\omega}{dr} \sim 0$) where Alfvén modes may present themselves at varied frequency so long as the fast ion resonance is satisfied. For fixed beam energy, the higher velocity hydrogen ions are theorized to resonate less efficiently with the low frequency modes compared to the slower deuterium ions. This explains the lack of a lower frequency branch for hydrogen fueled NBI but its presence in deuterium fueled NBI.
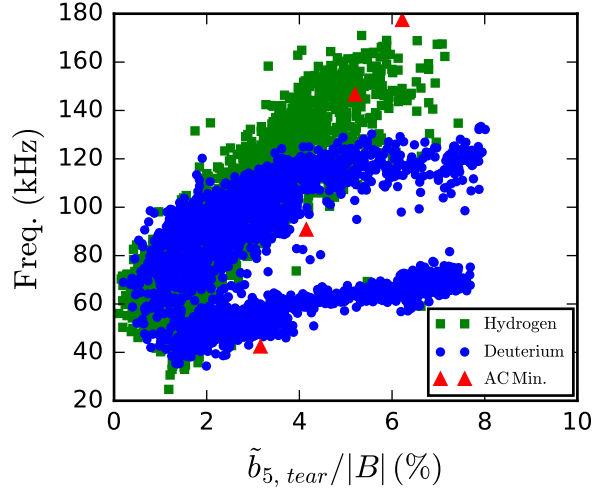
Figure 68: Burst frequency as a function of normalized core-resonant tearing mode amplitude for hydrogen and deuterium fueled NBI. The local minima in the Alfvén continua from Figure 67 are overplotted as red triangles.

Koliner *et al.* previously showed that the hydrogen NBI would produce $n = 5$ EPM

bursts in axisymmetric discharges, while the STELLGAP continua point to AEs at strong helical perturbation. Figure 68 overplots the local minima of Figure 67 (a.) - (e.) on the measured burst frequency as a function of the dominant tearing mode amplitude. One can see that the bursts are initially above the STELLGAP produced minima but then fall below. Perhaps the bursts originally appear as the typical $n = 5$ EPMs then convert to extrema modes due to the topological change and altered q-profile? While these observations are interesting and provide some physical insight onto the picture at hand, we are more interested in how, and if, these bursts impact the energetic particle population.
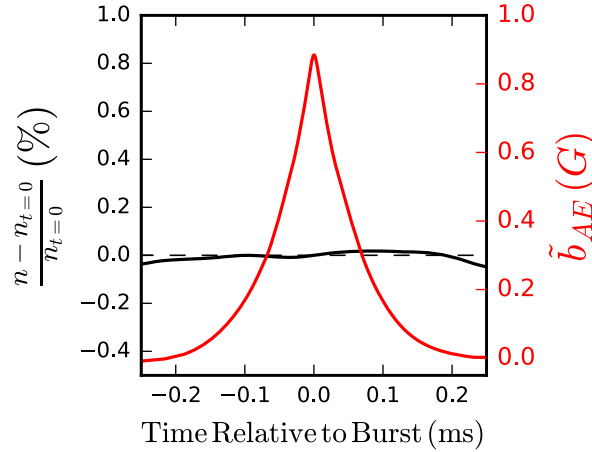
Figure 69: Normalized change in global neutron flux (black) and AE burst amplitude (red) with respect to bursting time for ensembled, deuterium-driven AE bursts.

In regards to fast ion transport, although the bursts result in a localized re-distrbution of the fast ions, they have little observed effect on the global particle content. Neutron flux measurement ensembles confirm this and show no marked difference in the presence of energetic particle instabilities. Figure 69 shows that the bursting modes themselves do not cause a significant change in the global neutron flux at less than the 1% level.

The redistribution of the fast ions associated with the bursting events is localized to the core, conserving the overall volume integration of the particle content.[110]

4.9 Summary

Overall, the neutron flux ensembles demonstrate that the bursting modes produce negligible losses. These results hold true regardless of the strength of the helical perturbation. Thus, even though one may infer information about the evolving helical equilibrium from the response of the energetic particle driven Alfvén modes, the modes themselves result in no substantial particle transport. Figure 61, however, shows that the mode amplitudes decrease as the plasma transitions to the helical state. If the modes are located near the minima in the Alfvén continuum, then the main damping mechanism can be ruled out and the loss of particle drive seems more logical. The lower frequency deuterium branch having weaker amplitudes, shown in Figures 61 and 62, further supports this as they would be further from the continuum and experience little to no damping. Therefore, one must consider other fast ion transport mechanisms, and the results of Chapter 3 provide an adequate explanation for the bursting mode disappearance at high core-resonant mode strength.

Chapter 5

Neoclassical Enhancement of Transport

5.1   A Brief Overview

Historically, the energy confinement time in early tokamak experiments was found to be much smaller than classical predictions. This gave way to investigations on particle transport where it was discovered that the toroidal geometry of the magnetic fields gave rise to enhanced particle transport. The particle diffusion was found to be orders of magnitude greater than the classical predictions with the inclusion of trapped particle effects.[141] This new-transport mechanism associated with the trapped particles was, rather unimaginatively, called neoclassical transport.[18, 21, 141] Neoclassical transport is simply classical transport with the added effects of toroidicity. The particle diffusion is still driven by Coulomb collisions except trapped particles' gyrocenters can drift radially larger than the gyroradius itself. This allows for particle diffusion with a larger effective step size and an increase in the transport coefficients.

The trapped particles occur due to toroidal effects which cause a poloidal variation in the magnetic field structure.[21] The toroidicity creates a magnetic field that is stronger on the inboard side of the machine than the outboard side, so particles with low-parallel velocity on the outboard side of the machine can become trapped in a magnetic well. The particles will stop, "bounce", reverse direction, and repeat this motion so long as they

remain in the magnetic well. The grad-B and curvature guiding-center drifts will radially displace the motion of the particle and give it a characteristic width and banana shape in the poloidal plane. An example of a banana orbit in a tokamak topology is shown below in Figure 70. As one can see, the motion of the gyrocenter is larger than the gyroradius,
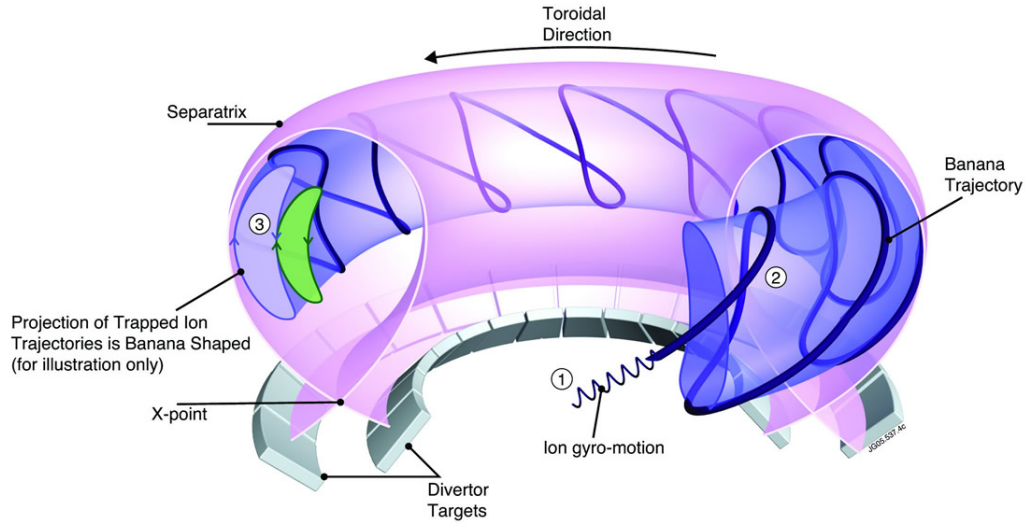
Figure 70: An illustrative trapped-banana orbit in a tokamak. Key features include: 1. An ion gyroradius much smaller than the banana width 2. The characteristic bouncing motion and reversal of direction 3. The poloidal projection of the orbit showing the characteristic banana shape. Taken from reference [142].

resulting in a larger diffusive step size.

In the non-axisymmetric geometries of the stellarator [4, 13] or field-rippled tokamak (from discrete toroidal field coils) [115, 143], particles can experience the same magnetic mirror effects due to a toroidal variation in the magnetic field which will produce additional magnetic wells for particle trapping.[144] Figure 71 pictorially represents these wells and is labeled with their representative orbits. The toridally trapped orbits are referred to as superbanana orbits.[145] Banana orbits, which are poloidally symmetric with respect to the vertical coordinate, Z, sample both the top and bottom halves of the
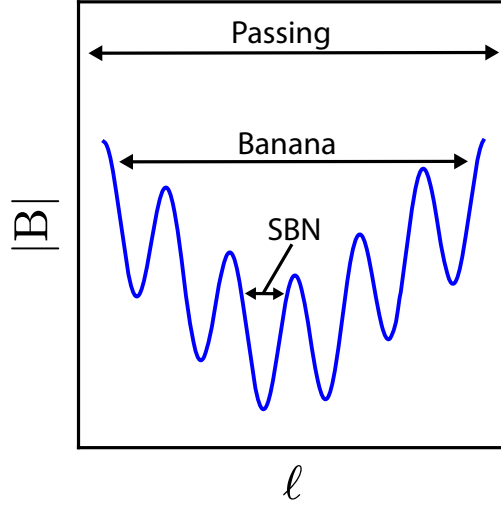
Figure 71: An illustration of magnetic field strength, $|B|$, along a field line length, ℓ. The regions that give rise to passing, banana, and superbanana (SBN) orbit trajectories are labeled. This is an adaptation of a figure in reference [144].

geometry equally which will cancel out any vertical drifts associated with a $B_\phi \sim 1/R$ field structure. Superbanana orbits are not constrained by the poloidal variation of the magnetic field and may only sample a small portion of the topology.[144] In this case, the cross-field drifts will not cancel and can allow for large radial excursions and convective losses.

Since collisions can effect the trapping and de-trapping of particles, neoclassical transport is commonly described in terms of the collisionality, ν.[18, 21] Collisions can scatter particles out of the trapped region in velocity space, negating trapped orbit effects. In order for neoclassical effects to occur, the particles must remain trapped for at least one bounce period. Figure 72 provides a representative description of neoclassical transport theory. Figure 72 is a simplified version of a figure in reference [4]. Please see reference [4] for a full description of Figure 72 in greater detail. The blue and green lines
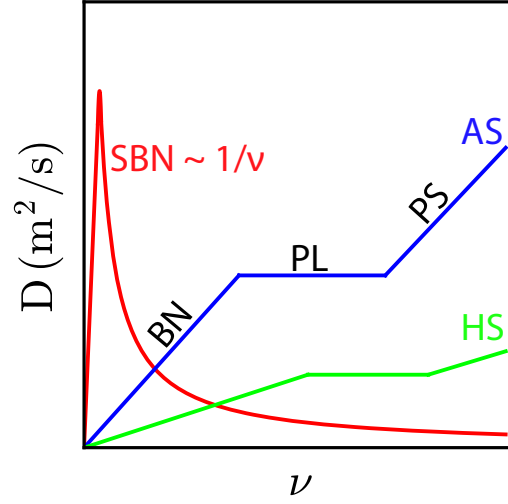
Figure 72: Particle diffusion, D, as a function of collisionality, ν, for an axisymmetric (AS - blue) and helically symmetric (HS - green) topologies with banana (BN), plateau (PL), and Pfirsch-Schluter (PS) regimes. The superbanana component (SBN - red) is dominant at low collisionality. This is an adaptation of a figure in reference [4].

represent the diffusion associated with an axisymmetric and helically symmetric configurations, respectively. At high-collisionality, frequent collisions prevent particles from completing full orbits and neoclassical effects are vanishingly small. This is the Pfirsch-Schluter regime and approaches the classical limit at high enough collisionality. At low collision frequency, trapped particles can execute full bounce periods, thereby enhancing classical transport due to a wider-than-Larmour banana width. The intermediate zone, the plateau regime, is where particles with low $v_\parallel$ undergo, on average, a single coulomb collision during a toroidal transit. The associated diffusion has no dependence on collisionality and can be viewed as a competition between particle de-trapping and collisions.

The red curve of Figure 72 represents effects associated with superbanana orbits. At

low collisionality, fast ions may execute full superbanana orbits with nonzero bounce-averaged radial drifts, which produces the large rise in the diffusion coefficient with decreasing collisionality. Of note, only the peaked $1/\nu$ dependence occurs from the helical magnetic trapping. The linear and roll-over portions of the curve at extremely low collisionality (i.e. $D \sim \nu$ and $\sqrt{\nu}$) result from radial electric fields present in stellarators.[4, 146, 147] These do not apply to the helical RFP and the work in this thesis.

In summary, magnetic confinement devices typically cover three regimes of neoclassical transport: the banana, plateau, and Pfirsch-Schluter. At low collisionality, trapped orbits enhance transport due to large diffusive step sizes. Toroidal field variations give rise to a special orbit topology called superbananas. These orbits can result in near-immediate losses due to non-averaged radial drifts. This would appear to be extremely detrimental to the inherently helical geometry of a stellarator, but advances in coil optimization have eliminated nearly all superbanana orbits.[148] Tokamak field-ripples and 3D-resonant magnetic perturbations are edge localized and have a small effect on fast ion losses, but studies are ongoing to further minimize their effects.[149] Experimentally, transport in toroidal magnetic fusion devices is typically larger than neoclassical values due to other macroscopic effects as well.

5.2   Orbit Topology

The previous section introduced the possible orbit types commonly present in a toroidal confinement device: passing or untrapped orbits, banana, and superbanana. Rather than strictly following a particle's trajectory, its orbit can be categorized based

solely on its constants of motion. On timescales large compared to the gyroperiod, Energy, E, magnetic moment, μ, and canonical angular momentum, p_ϕ, are conserved.[1, 150–152] They are found below in equations 5.1.

$$E = \frac{1}{2}mv^2 \tag{5.1a}$$

$$\mu = \frac{mv_\perp^2}{2B} \tag{5.1b}$$

$$p_\phi = mRv_\phi + e\psi_p \tag{5.1c}$$

The orbit topology is found by examining the "legs" of the orbit where the orbits cross a "stagnation" surface. The stagnation surface is the surface at which the extreme values of the poloidal flux along a particle's orbit can be found. Since the standard RFP is up-down symmetric, this is simply the equatorial mid-plane. Considering the poloidal projection of a given orbit, passing orbits cross the mid-plane on both sides of the magnetic axis while trapped (banana) orbits cross on the same side. The orbit legs can easily be found by recasting the orbit in terms of the constants of the motion. A complete description of the methodology for classifying particle orbits may be found in reference [150]. In short, by considering a particle with fixed energy, the values of p_ϕ and μ can be calculated as functions of R, Z, and pitch angle. One can then draw contours of p_ϕ and μ in the (R, Z) plane for a given pitch angle where each pair of contours would correspond to a different orbit. The intersection points of the p_ϕ and μ contours translate to the orbit legs. Based on the orbit legs' locations, an orbit may be identified as passing, trapped (banana), or pinch (kidney). Kidney orbits are a special case of a banana orbit that just barely encompasses (or pinches) the magnetic axis.

This procedure was performed for a standard RFP equilibrium created with MSTFit

for a 20 keV hydrogen ion. [153] The results are shown in Figure 73 as a function of the ion's canonical momentum and a pitch variable, $\mu B/E = v_\perp^2/v^2$. The NBI deposition
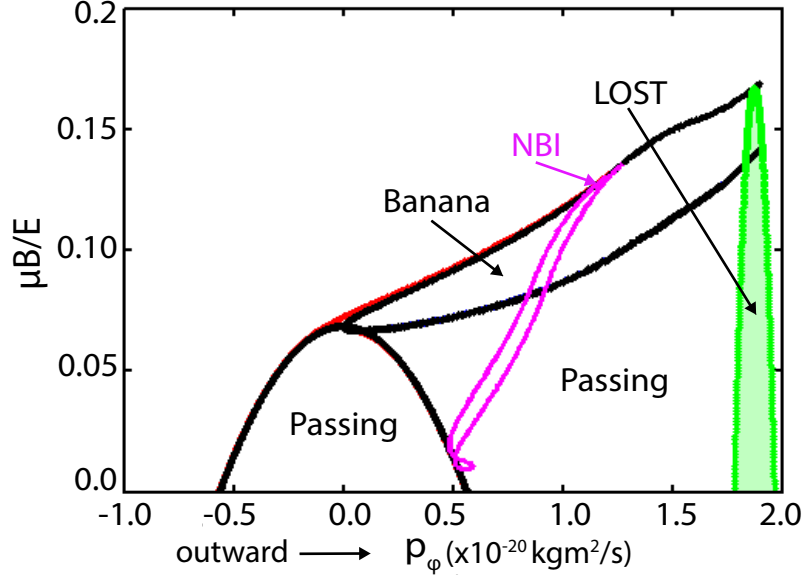
Figure 73: Orbit topology diagram for a 20 keV hydrogen ion in a 400 kA, $F = -0.27$ RFP plasma. The purple line represents the initial NBI deposition, and the green region highlights the parameter space that gives rise to lost orbits.

(purple line) starts in the banana region at large major radius (high p_ϕ) then transitions to passing orbits through mid-radius to the core. This agrees with expectations for the beam's tangential injection geometry. The plasma edge is dominated by the poloidal field component which gives the fast ions a very low pitch (perpendicular velocity) suitable for banana orbits. In practice, however, fast ion banana orbits are minimal due to the fast ion's large gyroradii and fast ion island overlap near the edge. The passing region of the NBI denotes the core-confined fast ions with high-parallel velocity. The favorable nature of the RFP's guiding-center drifts is manifested in the small lost region (especially when compared to the tokamak case in Figure 74) in p_ϕ, μ space.

Repeating this procedure for a hypothesized MST tokamak plasma where the externally induced B_ϕ could reach 0.4 T to match the strength of a 400 kA RFP discharge, the resultant orbit topologies are shown in Figure 74. The biggest difference to the standard
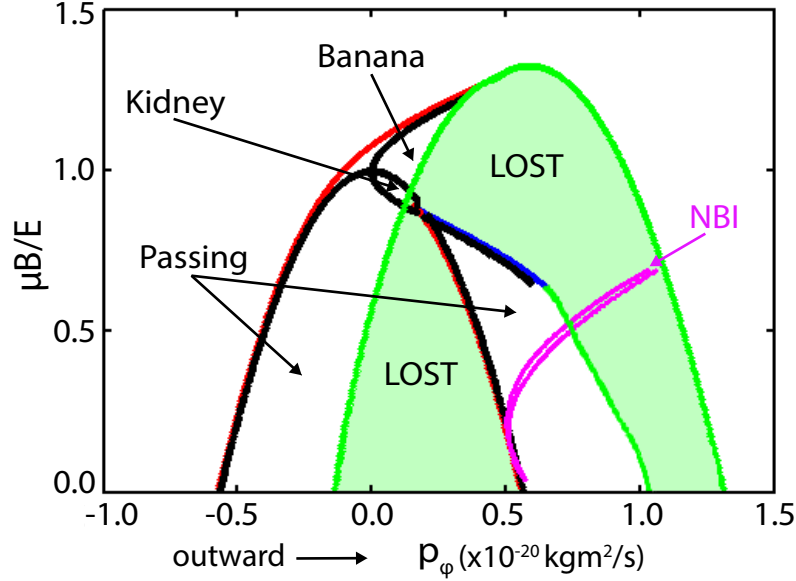
Figure 74: Orbit topology diagram for a 20 keV hydrogen ion in a hypothetical MST tokamak discharge with $B_\phi(0)$=0.4 T and $B_\theta(0)$=0.05 T. The purple line represents the initial NBI deposition, and the green region highlights the parameter space that gives rise to lost orbits.

RFP case is the size of the "LOST" region. The tokamak plasma possesses a $B_\phi \sim 1/R$ dependence that produces vertical drifts. As an aside, MST's maximum B_ϕ strength is $\sim$0.14 T and cannot confine 20 keV fast ions. Poor fast ion confinement in MST tokamak plasmas has been verified by a lack of beam-excited Alfv'enic activity and sharp neutron decay with beam turn-off in an experiment conducted without much fore thought.

Unfortunately, the topological orbit identification method cannot be applied to the QSH state in the RFP because the helical perturbation breaks the ϕ-symmetry and conservation of p_ϕ. Later in this chapter, the non-conservation of p_ϕ will be used as a

proxy to determine the presence of superbanana orbits.

5.3 Neoclassical Transport in the Standard RFP

Quite simply, particles in the standard RFP do not experience any neoclassical enhancement to cross-field transport. The transport related to other effects is comparable or larger than that associated with neoclassical values. In Chapter 3, the tearing-mode induced magnetic stochasticity dominated the confinement properties of the thermal particles.[90] Parallel particle motion along the field line surpassed that of the perpendicular motion.[91–93] Thermal particles wander around the overlapping magnetic islands in the standard RFP and are lost prior to the occurrence of trapped particle effects.

While fast ions possess good confinement in the standard RFP, they also experience no neoclassical transport. The relatively weak fields of the RFP translate to a large fast ion gyroradius. Depending on the plasma conditions, particle pitch, and location of the fast ion, the Larmor radius can range from approximately 3 cm to upwards of 10 cm. Fast ions with an acceptable pitch will execute banana orbits but the banana width will be on the order of, or smaller than, the gyromotion. This is explicitly observed in Figure 75 for a simulated fast ion trajectory in a standard RFP discharge. Clearly, the large gyroradius replaces the banana width as the diffusive step size and gives rise to classical transport.

In regards to the MST experiment, the tangential injection of fast ions produces high-pitch trajectories along most of the injection path length. Figure 73 demonstrates that the well-confined ions injected near the core result in passing orbits while ions near the edge have lower pitch and may be trapped. The fast ions near the edge, however,
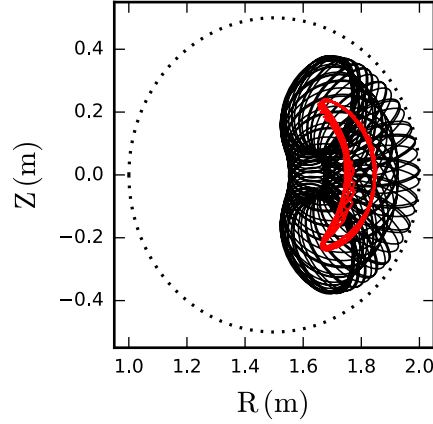
Figure 75: A poloidal projection of a banana orbit produced from a 25 keV deuterium ion with initial pitch of 0.6 in a 300 kA standard RFP discharge with the guiding-center in red and particle trajectory in black.

may be lost relatively quickly due to large gyroradii and fast ion island overlap. The core deposited fast ions must pitch-angle scatter to lower pitches in order to transfer to trapped orbits. Therefore, trapped fast ions only compose a small portion of the total population in standard RFP discharges on MST.

5.4 Toroidal Symmetry Breaking in the Helical RFP

Stated many times already, the QSH state in the RFP appears to qualitatively resemble a stellarator. The helical core creates a toroidal variation in the field structure and toroidal magnetic wells. Discussed earlier in this chapter, these wells can trap particles of sufficiently low-pitch and give rise to strong neoclassical transport effects. The helical variation is strongly observed in the magnetic contours of the QSH state.

The magnetic field structure was created with the aid of the ORBIT produced equilibrium and radial tearing mode eignefunctions. Recalling that the ORBIT equilibrium

assumes axisymmetry, the equilibrium profiles (B_θ and B_ϕ) were simply mapped symmetrically around a toroidal geometry. Since ORBIT outputs the radial tearing mode eigenfunctions as radial profiles through Newcomb's analysis, they needed to be expanded toroidally and poloidally with reference to their mode numbers. Knowing $\tilde{b}_r$, one can use $\vec{\nabla} \cdot \vec{\tilde{b}} = 0$ and $\vec{\nabla} \times \vec{\tilde{b}} = \lambda \vec{\tilde{b}}$ to find $\tilde{b}_\theta$ and $\tilde{b}_\phi$ and arrive at equations 5.2.

$$\tilde{b}_r(r, \theta, \phi) = \tilde{b}_r \cos(m\theta - n\phi + \delta_\phi) \tag{5.2a}$$

$$\tilde{b}_\theta(r, \theta, \phi) = \beta \cos(m\theta - n\phi - \frac{\pi}{2}) \text{ for m} = 1 \tag{5.2b}$$

$$\tilde{b}_\phi(r, \theta, \phi) = \left(\beta \frac{nr}{mR_0} + \frac{r\lambda}{am}\tilde{b}_r\right) \cos(m\theta - n\phi + \pi) \text{ for m} = 1 \tag{5.2c}$$

$$\tilde{b}_\theta(r, \theta, \phi) = -\frac{R_0 \lambda}{an}\tilde{b}_r \cos(m\theta - n\phi - \frac{\pi}{2}) \text{ for m} = 0 \tag{5.2d}$$

$$\tilde{b}_\phi(r, \theta, \phi) = -\frac{R_0}{n}\left(\frac{d\tilde{b}_r}{dr} + \frac{\tilde{b}_r}{r}\right) \cos(m\theta - n\phi + \pi) \text{ for m} = 0 \tag{5.2e}$$

$$\beta = \left[\frac{-n\lambda r^2}{m^2 a R_0}\tilde{b}_r - \frac{1}{m}\frac{d(r\tilde{b}_r)}{dr}\right]\left[1 + \left(\frac{nr}{mR_0}\right)^2\right] \tag{5.2f}$$

In the above equations, $\tilde{b}_r = \tilde{b}_r(r)$ and δ_ϕ is a randomly assigned toroidal phase. Adding equations 5.2 to the equilibrium creates the full magnetic topology in three-dimensions with the appropriate experimental boundary conditions applied.

The magnetic contours for a MH state at mid-radius are shown in Figure 76 for the equilibrium, the equilibrium and the dominant (1,5) tearing mode, and the equilibrium with all tearing modes present. Looking at Figure 76, the equilibrium field still dominates, and the tearing modes wash out the effects of the (1,5) mode. Since the (1,5) tearing mode is the core-resonant mode, it is slightly stronger than the other modes
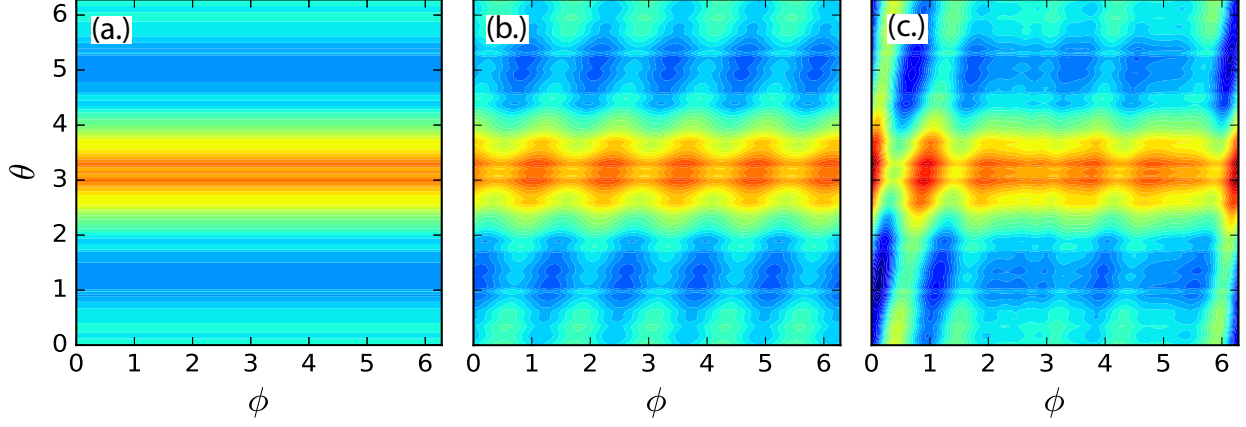
Figure 76: Magnetic contours of a MH state at mid-radius separated into the equilibrium fields, (a.), the equilibrium + (1,5) tearing mode, (b.), and the equilibrium + all tearing modes, (c.). The three subplots are normalized to the relative maximum between them.
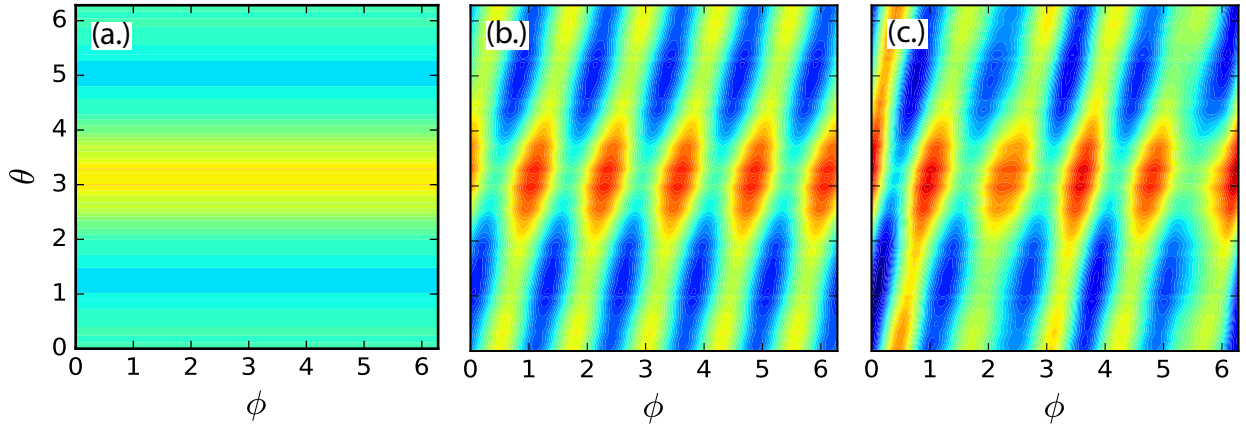
Figure 77: Magnetic contours of a QSH state with $\tilde{b}_5/|B| \sim 7.3\%$ at mid-radius separated into the equilibrium fields, (a.), the equilibrium + (1,5) tearing mode, (b.), and the equilibrium + all tearing modes, (c.). The three subplots are normalized to the relative maximum between them.

which is why a slight $m = 1$, $n = 5$ presence appears in part (c.) along with a substantial $m = 0$, $n = 1$ component. The subdominant modes are comparable in amplitude, so the toroidal periodicity (i.e. n dependence) is washed out and the contours are relatively constant in ϕ with only the $m = 1$ variation remaining. Thus, one should expect poloidally trapped particles, or banana orbits, in the MH state and no toroidal trapping.

The contours of a QSH state are shown in Figure 77. The ϕ symmetry is clearly broken by the large (1,5) perturbation, and the contours qualitatively resemble that of an unoptimized stellarator.[154] Large toroidal variations are present that establish regions of high-low-high field strength. In essence, this should allow for the presence of superbanana orbits which could be extremely detrimental to the fast ion confinement.

A field line trace was performed starting at $\theta = \pi$, $\phi = 0$ in the topology of Figure 77 (c.) and is overplotted in Figure 78 (a.). Figure 78 (b.) plots the normalized magnetic
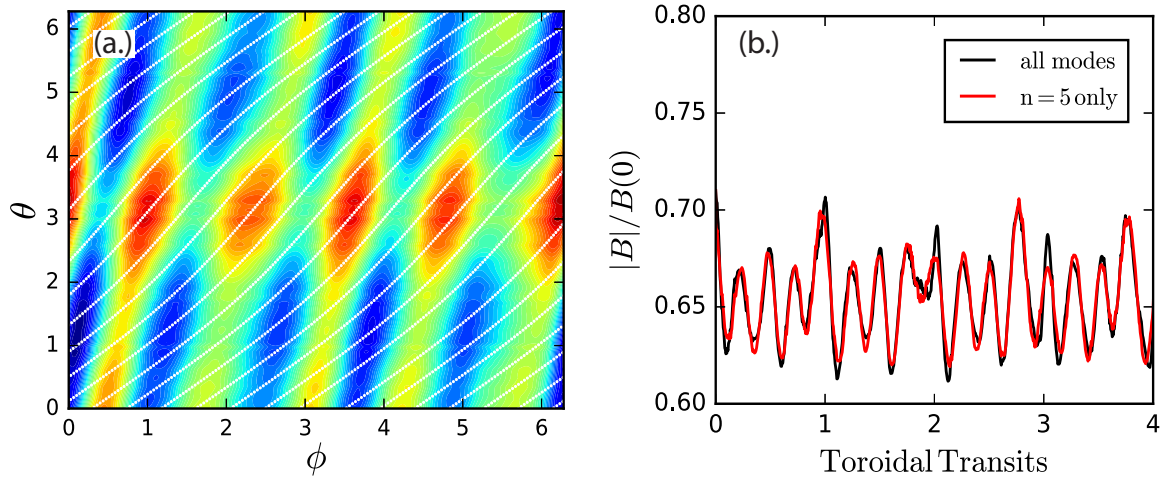
Figure 78: The magnetic contour of Figure 78 (c.) with a field line trace (white) overplotted, (a.), and the magnetic field strength along that field line for several toroidal transits in the presence of only the $n = 5$ tearing mode and all modes, (b.).

field strength for the field line for a number of toroidal transits. Toroidal magnetic wells exist that could allow for low-pitch fast ions to become helically trapped and could result

in superbanana orbits.

5.5 ORBIT Diffusivity Calculations

Any neoclassical transport should be evident by calculating the particle diffusion as a function of collisionality. If the superbanana orbits produce strong radial transport of the fast ions, then the $1/\nu$ dependence should present itself at low collisionality. ORBIT was used to calculate volume averaged diffusion coefficients in the same manner as Gobbin and Spizzo *et al.* in reference [109].

The diffusion, D, was found from the outward particle flux, Γ, and density gradient, $\frac{dn}{dr}$, via equation 5.3.

$$\Gamma = D\frac{dn}{dr} \tag{5.3}$$

The ORBIT simulations were performed with only the (1,5) mode active ensuring that any measured transport effects would be from the helical field perturbation and not the subdominant tearing modes. The equilibrium and the (1,5) tearing mode define a helical magnetic field, $\vec{B}_H = \vec{B}_0 + \tilde{b}_{1,5}$, which can be used to numerically solve for a helical-flux coordinate, χ, such that $\vec{\nabla}\chi \cdot \vec{B}_H = 0$.[155] The helical flux surfaces formed the boundaries for the simulation. An injection surface was chosen near the helical core where the particles were initialized. An outer χ-surface was chosen as the diffusion boundary where particles would be counted and then re-injected at the injection surface. The run would continue until the outward particle flux saturated which was found to occur at roughly 1500 toroidal transit times (the temporal units of any ORBIT run).

Before continuing onward with the description of the diffusivity computation, it is important to discuss the chosen χ-surfaces. Depending on the particle energy (i.e. fast

ion vs. thermal ion), one must take into account guiding-center drift effects. While a χ-surface near the helical axis is chosen as the injection surface for particles to originate from, drifts can quickly displace the particle to a different starting surface. This is apparent in Figure 79 which shows the desired injection surfaces (black), the outer boundaries (red), and the actual injection surfaces(green) for fast ions and thermal particles. Evidently, the fast ion injection surface is much larger than intended due to
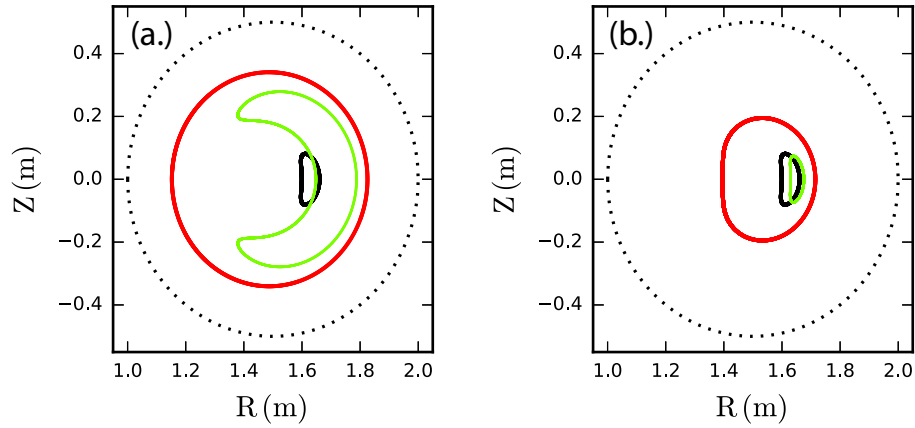
Figure 79: χ-surfaces used for ORBIT diffusion coefficient calculations for 25 keV fast ions, (a.), and 900 eV thermal particles, (b.), in the presence of a helical pertutbation of approximately 7%. The black boundary denotes the intended injection surface, the green boundary represents the actual injection surface due to particle drifts, and the red boundary is the outer defined limit for the calculations.

the fast ions' strong drifts. This is akin to how fast ions ignore the standard RFP's tearing-induced magnetic stochasticity. The thermal particles have much weaker drifts, so their injection is roughly the same as the intended χ-surface. Care must be taken to choose a large enough outer boundary for the fast ions to ensure no prompt losses of injected particles and an inflated value for the diffusion coefficient.

In order to calculate all of the parameters of equation 5.3, the geometry of the helical flux surfaces has to be numerically computed. The χ-surface volumes were found

via a Monte-Carlo method in ORBIT where particles were randomly placed in three-dimensions and tallied depending on whether they fell inside or outside the χ-surface. The ratio of the number of particles within the surface to the total number of particles was then related to the surface volume relative to the MST volume shown in equation 5.4.

$$\frac{N_{\text{inside}}}{N_{\text{total}}} = \frac{V_\chi}{V_{MST}} \tag{5.4}$$

Knowing the χ-surface volume, V_χ, the surface area was then estimated as $A_\chi = \frac{V_\chi}{2\pi r_{\text{eff}}}$ where r_{eff} is the effective radius of a given surface found by taking the average of all points along the surface at a single toroidal location. These procedures can be performed for any χ-surface, providing the needed geometries to calculate Γ and $\frac{dn}{dr}$.

The outward particle flux, Γ, can easily be calculated from the running count of particles lost to the outer boundary, N_{lost}, the surface area of the outer boundary, A_{out}, and the simulation run time as shown in equation 5.5.

$$\Gamma = \frac{N_{\text{lost}}}{A_{\text{out}} \times \text{run time}} \tag{5.5}$$

The density gradient is found by histogramming the particles based on their χ-coordinate at the end of the run. The volume and effective radius for each χ-surface represented in the histogram was then found to find the particle density, n, as a function of radius. A linear fit was applied whose slope yields the density gradient, $\frac{dn}{dr}$. At this point, all the needed quantities have been computed, and the diffusion coefficient is solved from equation 5.3.

The diffusivity calculation was repeated for a number of ORBIT runs with varied

collision frequency. Slowing collisions were turned off so that the particles' energies re-
mained fixed while classical and pitch-angle scattering were kept. Figure 80 shows the
resulting diffusivities, D, as a function of collisionality, ν, normalized to the particle's
toroidal transit time, $\tau_{tor} = 2\pi R_0 / v$, for fast ions with random positive initial pitch and
thermal ions with random initial pitch between -1 and 1. The thermal particles are in
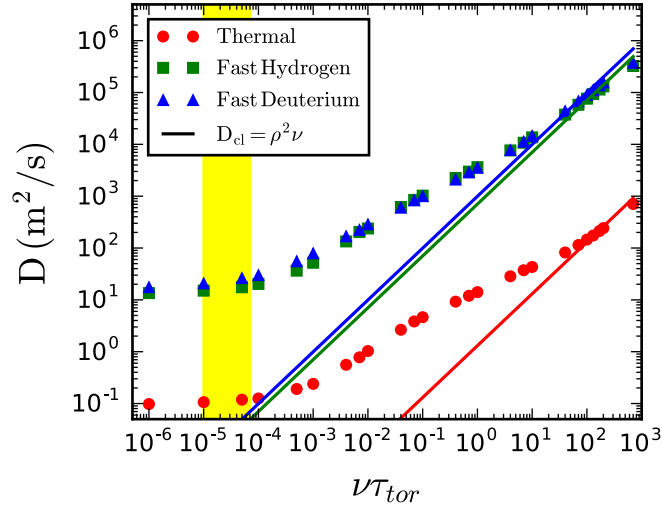
Figure 80: ORBIT calculated diffusivity profiles for 25 keV hydrogen and deuterium ions
and 900 eV deuterium ions in a magnetic topology with only the (1,5) mode present at
a strength of 7.3% relative to the equilibrium field. The region highlighted in yellow
denotes the MST operational regime for 25 keV ions. The collisionality, ν, is normalized
to the particle toroidal transit time, $\tau_{tor} = 2\pi R_0 / v$. This is an extension to fast ions
from thermal particles in reference [109].

good agreement with the results of Gobbin and Spizzo *et al.*, so the methodology pre-
viously described appears correct. The fast ion diffusivities monotonically increase with
collisionality until they reach the classical limit, $D_{cl} = \rho^2 \nu$ where ρ is the Larmor radius.
As fast ions in MST experience a relatively low collisionality (yellow region), one would
expect the presence of helically trapped superbanana orbits for low-pitch particles. Fig-
ure 80, however, lacks the $1/\nu$ dependence characteristic of these orbits.[4] Thus, while

the presence of the large $m = 1$, $n = 5$ mode allows for helical trapping of fast ions and the existence of superbanana orbits, their effect appears to be lacking. The fast ion diffusivity, subject to MST levels of collisionality, appears to be of order 10 m^2/s which gives an estimated confinement time $(0.3^2/D)$ of 9 ms where the outer boundary's (red curve) radius of 0.3 m was used. This is in good agreement with the fast ion confinement simulations in Chapter 3 for a QSH state free of subdominant modes.

It would be interesting to see how these results differed with the inclusion of the subdominant tearing modes, but the methodology breaks down in the presence of additional modes. The fast ion injection surface becomes stochastic and greatly complicates the diffusion calculation. An example of such a case is shown in Figure 81 that shows the fast ion injection surface in the presence of the (1,5) and (1,6) tearing modes. With
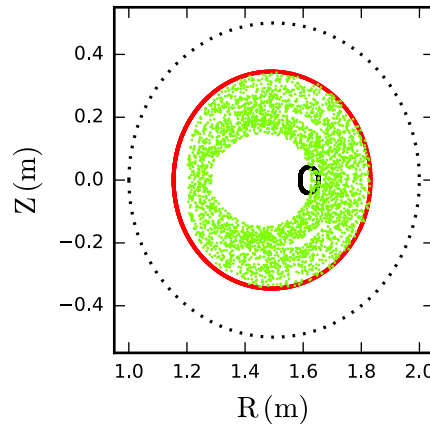
Figure 81: The same injection and outer boundary χ-surfaces for fast ions in Figure 79 (a.) with the inclusion of the (1,5) and (1,6) tearing modes.

the inclusion of just one additional tearing mode, the fast ion injection surface becomes fairly stochastic and approaches the outer simulation boundary. While a solution would simply be to extend the outer boundary surface and inject particles more locally to the core, this fails with more tearing modes as the surfaces give way to larger and larger

stochasticity. Essentially, the definition of the helical flux, χ, starts to fail. This leads to artificially inflated diffusion coefficients as some injected particles are placed on or outside the outer boundary. This issue may be addressed as future work and is discussed more in the conclusion. Importantly, this serves as yet another illustration of the impact of the subdominant tearing modes on fast ion phase-space.

5.6 Superbanana Orbits in the Helical RFP

The hypothesis that the helical RFP possesses similar neoclassical transport to that of an unoptimized stellarator proved to be incorrect. Superbanana orbits should occur due to the toroidal field variation created by the large (1,5) perturbation. The super-banana enhancement of cross-field transport, however, relies on the guiding-center drifts. While the perturbation levels reach a maximum of approximately 7-8%, the equilibrium field still dominates the particle drifts given in equations 3.7. In that regard, the drifts predominantly occur in the poloidal (θ) and toroidal (ϕ) directions. While B_ϕ has curvature in major radius ($\hat{R}$) that gives rise to vertical drifts, the poloidal field is comparable in amplitude which severely weakens this effect. In that sense, the radial drifts are strongly compensated by the large rotational transform of the RFP. Figure 82 presents the magnetic contour of a QSH state shown earlier with the guiding-center drifts over-plotted as a vector field. While the radial components of the vectors are not shown, their calculated values are appreciably smaller than the θ and ϕ components. Therefore, the RFP's well-natured guiding-center drifts result in $< \vec{v}_d \cdot \vec{\nabla} \psi > \sim 0$, where $\vec{v}_d$ denotes the guiding-center drifts and $<>$ represents an average over the particle's motion, and little radial transport.[4, 156] Thus, one may argue that the helical RFP acts more akin to an
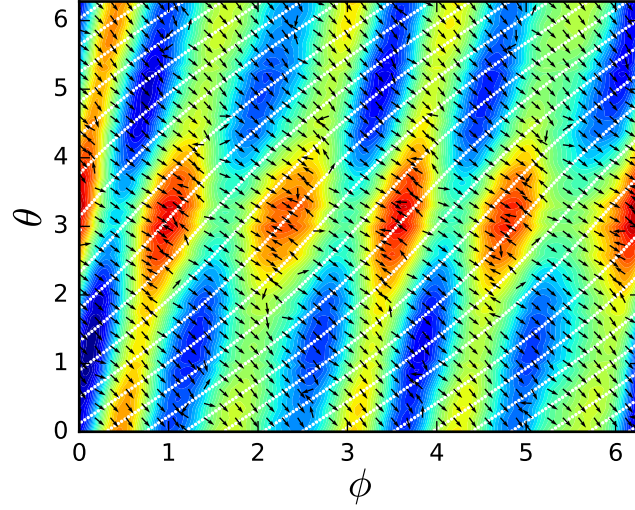
Figure 82: The same magnetic contour plot and field line trace as Figure 78 (a.) with added vectors denoting the grad-B and curvature guiding-center drifts. The vectors have been normalized to unity length.

omnigenous stellarator in which collisionless trapped trajectories are confined.[13, 154, 156–158]

An interesting effect in the QSH RFP geometry is the smooth transition from one orbit configuration to another. The drifts act to push the fast ions out of the helical magnetic wells which would transition the orbit from a superbanana to a banana or passing topology. A helically trapped particle will undergo small outward drifts, relative to drifts in the poloidal and toroidal directions, so it appears that superbanana orbits may still occur in the QSH state. The RFP's guiding-center drifts, however, are more likely to force a change in the orbit topology with minimal enhancement of the outward transport.

This has been numerically verified using a full particle trajectory code for the topology shown in Figure 82. Figure 83 shows a 25 keV deuterium ion orbit that experiences helical trapping. Figure 83 (c.) shows a helically trapped orbit that bounces asymmetri-
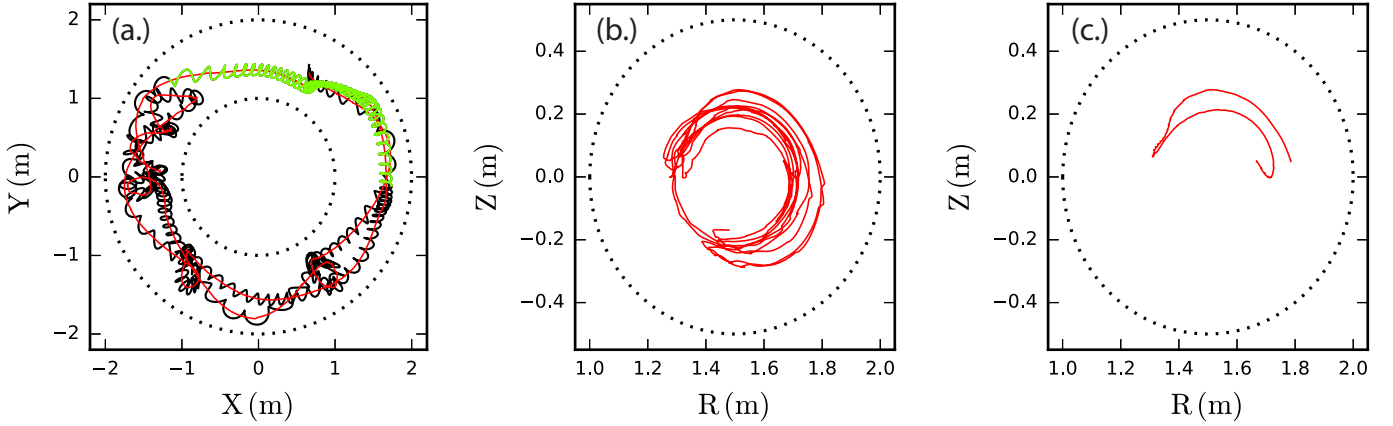
Figure 83: A 25 keV deuterium orbit with 0.6 initial pitch in the QSH topology shown in Figure 82. The toroidal view, (a.), shows the particle trajectory (black), guiding-center motion (red), and a helically trapped portion of the particle path (green). Subplot (b.) shows the poloidal projection of the motion with only the guiding-center shown for clarity. The helical trapping portion is shown in the poloidal view, (c.).

cally in Z. In fact, the motion is limited to the top half of the machine for a few bounce periods. This particle would undergo strong vertical drifts and near immediate loss in a stellarator or tokamak. The fast ion does undergo some outward motion as evidenced by the upward drift but remains confined; it drifts in-surface onto another orbit type. The particle continues with its motion until the end of the run which was fixed at a distance of 100 m. Throughout the simulation lifetime, the particle undergoes superbanana, banana, and passing orbits as evidenced in Figure 83 (b.). The fast ion poloidally drifts and transitions from orbit to orbit but is never lost.

All in all, the fast ions may execute motion due to helical trapping but experience negligible radial transport. Superbanana orbits can exist in the QSH state but have minimal bearing on transport as particles simply drift, or pitch-angle scatter, to other orbit topologies. A small vertical drift component exists but is relatively weak thanks to the RFP's comparable toroidal and poloidal field strengths. Thus, fast ions in the

QSH state experience little enhancement of transport as a result of neoclassical effects, explaining the lack of the characteristic $1/\nu$ diffusion in Figure 80.

Even though the transport associated with superbanana orbits is vanishing in the QSH state, it is still of interest to know the impact of the helical perturbation on the formation of the superbanana population. Direct numerical identification of the orbit topology is very difficult though: using the orbit in Figure 83 as an example, the orbit could be classified as passing or trapped depending on the time frame in which the motion is examined. Orbits that spend time in the superbanana regime will have strong nonconserved p_ϕ, which is used as a metric to evaluate the impact of the helical perturbation.

An ORBIT simulation with 4000 25 keV deuterium test particles was conducted with collisions turned off in the presence of only the equilibrium and (1,5) mode. The simulation was performed for two particle groups with different initial conditions as a way to recognize that the anisotropic NBI particles used in experiment do not represent a full pitch distribution. The first group contained particles that replicated MST's NBI deposition and pitch-distribution. The second group was a random Monte-Carlo placement of particles that covered nearly all of the spatial domain and the positive pitch domain. The toroidal canonical angular momentum was calculated for each particle as a function of time until either the particle was lost or the run ended (run time of 50 toroidal transits). The fraction of fast ions with conserved p_ϕ is shown in Figure 84 as a function of the helical perturbation strength. At low $\tilde{b}_5$ amplitude, p_ϕ is almost entirely conserved. The error attributed with the p_ϕ constancy is roughly 10% due to particles near the plasma edge that experience near immediate loss. This results in a time window too small to check for the constancy of p_ϕ. Thus, the helical effects appear to be near 0
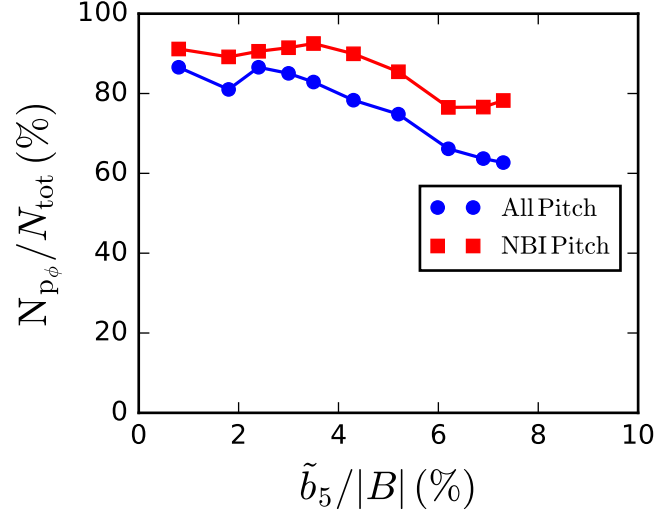
Figure 84: Fraction of 25 keV deuterium ions with conserved p_ϕ as a function of $n = 5$ tearing mode amplitude found with ORBIT. The "NBI Pitch" labeled data represents a simulated deposition of particles mimicking that of MST's NBI. The "All Pitch" labeled data represent particles initially seeded within the domain: $\{\frac{v_\parallel}{v} \in [0.01, 1.0]; \frac{\psi_p}{\psi_p(a)} \in [0.1, 1.0]; \theta \in [0, 2\pi]; \phi = 0\}$.

until about $\tilde{b}_5/|B| \sim 4\%$ which is around the transition point for the establishment of a helical core.

Only low-pitch particles can become trapped in the magnetic wells of Figure 71 and undergo superbanana orbits with non-conserved p_ϕ. The pitch-distribution of the NBI is mainly parallel, so the Monte-Carlo subgroup should contain more lower pitch particles. Examining sample orbit trajectories from each subgroup, superbanana and banana orbits were more prevalent in the Monte-Carlo initialized particles much more frequently than in the NBI ions, as expected. The key feature of Figure 84 is that the fraction of ions with conserved p_ϕ decreases with the transition to the QSH state. This is entirely expected as the toroidal variation is needed for the presence of superbanana orbits. Fixing the helical perturbation strength at 7.5%, the same ORBIT calculations were performed with subdominant modes scaled from 0 to their respective experimental

levels. The results are presented in Figure 85.
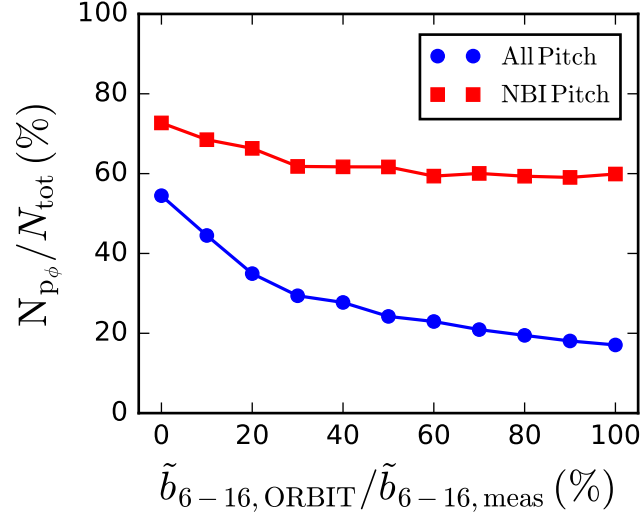
Figure 85: Fraction of 25 keV deuterium ions with conserved p_ϕ as a function of scaled subdominant tearing mode amplitudes found with ORBIT at $\tilde{b}_5/|B| = 7.5\%$. The "NBI Pitch" labeled data represents a simulated deposition of particles mimicking that of MST's NBI. The "All Pitch" labeled data represent particles initially seeded within the domain: $\{\frac{v_\parallel}{v} \in [0.01, 1.0]; \frac{\psi_p}{\psi_p(a)} \in [0.1, 1.0]; \theta \in [0, 2\pi]; \phi = 0\}$.

The rapid loss of particles from the subdominant tearing modes must be taken into consideration. The "All Pitch" particles are spread over a larger radial extent than the majority of the NBI deposited fast ions and experience more stochastic transport effects. Therefore, the relative error of the "All Pitch" subgroup should increase with the addition of the subdominant modes due to rapid losses. Regardless, the lower-pitch Monte-Carlo group still experiences a larger breaking of p_ϕ than the high-pitch NBI fast ions. While the breaking of p_ϕ occurs weakly for the emergence of the subdominant modes, the presence of the lower-pitch fast ions provides the greatest impact on p_ϕ conservation.

5.7   Summary

While problematic for devices with broken toroidal symmetry, neoclassical transport enhancements to the RFP remain absent. Overall, the particles are still lost quickly due to the presence of the subdominant tearing modes discussed in Chapter 3. Superbanana orbits are possible but, as shown in Figure 80, bear no significant impact on fast ion transport. The superbanana particles are more likely to pitch-angle scatter or poloidally drift out of the magnetic well to a new orbit than remain trapped.[115, 143, 156] The radial displacement of a superbanana orbit is negligible when compared to other transport. The macroscopic effects of the stochastic fast ion phase-space dominate over the neoclassical effects, making the presence of superbanana orbits fairly moot in the helical RFP.

Chapter 6

Conclusion

6.1 Summary of Key Results

In the standard RFP, fast ions typically achieve classical confinement due to the RFP's guiding-center drifts. The fast ions are decoupled from the tearing mode induced magnetic stochasticity and are simply limited by slowing collisions with electrons. The RFP, however, contains the unique ability to spontaneously transition to a helical equilibrium at adequately high Lundquist number. This transition is marked by a collapse of the tearing mode spectrum to the core-resonant mode. A well-ordered helical core forms surrounded by the RFP's natural magnetic stochasticity. Thermal particles respond favorably to this transition and experience improved confinement. This thesis answers the question of the fast ion response to the changing magnetic topology. Specifically, the fast ion transport associated with energetic particle driven Alfvénic activity, neoclassical effects, and tearing modes were investigated.

Energetic particle driven Alfvén instabilities, commonly observed in standard RFP discharges, up-shift in frequency with growth in the core-resonant tearing mode and cease to exist at corresponding at high amplitude. 3D modeling of the helical equilibria and Alfvén continua demonstrate that the frequency shift and radial displacement of energetic particle bursts are a direct consequence of the evolving equilibrium itself. While the bursts have not yet been identified, FIR coherence measurements mapped onto

STELLGAP-produced Alfvén continua suggest the existence of gap modes in the helical RFP. These measurements may provide insight into the helical formation; however, the bursting modes themselves have no role in the observed global particle transport. Neutron measurements confirm that the overall volume integration of the fast ion content remains constant throughout the bursts.

While the helical RFP may qualitatively resemble an unoptimized stellarator, ORBIT simulations show a vanishingly small neoclassical transport enhancement as a consequence of the RFP's well-natured guiding-center drifts. Reconstructions of the QSH state magnetic topology demonstrate that helical wells exist for toroidal trapping, but ORBIT calculated diffusivity simulations failed to produce the $1/\nu$ dependence characteristic of superbanana transport. The grad-B and curvature drifts result in minimal radial drifts and are more likely to cause a change in the orbit topology. In this regard, the QSH state acts as an omnigenous stellarator where superbanana orbits may be present but have no detrimental effects on confinement. This was directly observed in full orbit simulations where helical trapping was present and confinement was still maintained.

Neutron flux and neutral particle analysis measurements support the disappearance of the bursting modes in the QSH state and infer fast ion losses. More so, the neutron signals demonstrate that the fast ions respond more strongly to the subdominant tearing modes in the QSH state than in the MH state. The beam-blip technique provided direct experimental fast ion loss time measurements and confirms substantial fast ion losses in the helical RFP. Corroborating ORBIT simulations illustrate that growth in the dominant $n = 5$ tearing mode coupled with remnant secondary modes are to blame. ORBIT produced fast ion phase-space Poincaré plots clearly illustrate this growth in

the $n = 5$ fast ion guiding-center island and the detrimental effects of the subdominant tearing modes. This appears to be a transport mechanism akin to Rechester-Rosenbluth transport where the core-resonant (1,5) mode is treated as a part of the equilibrium and the stochasticity is strictly governed by the subdominant modes. The modeled and experimental diffusivity goes as w_{fi}^2, $\tilde{b}$ as a function of the helical perturbation and follows Rechester-Rosenbluth scaling as a function of the subdominant mode amplitudes in the QSH state.

6.2   Implications for the Next-Step RFP

Overall, while thermal particles experience a reduction in stochasticity and improved confinement, fast ions experience the opposite. Examination into fast ion transport in relation to Alfvén instabilities, tearing mode effects, and neoclassical effects was performed. Remnant tearing mode induced fast ion phase-space stochasticity governs the fast ion confinement more so than trapped particle effects. The dominant fast ion transport mechanism is a developed stochasticity in the fast ion guiding-center phase-space, due to the increase in $n = 5$ tearing amplitude, and is sharply impacted by the amplitude of remnant, subdominant modes.

While this presents an obstacle in the utilization of the QSH regime in a fusion scheme, the subdominant mode strengths decrease with Lundquist number scaling, lessening their impact, and may present a consistent scenario for ignition provided the tearing instability falls fast enough with S.[16, 159, 160] The NBI-born fast ions in MST have normalized parameters designed to mimic fast alphas in an envisioned reactor, and the measured confinement is well below that required for a self-heated burning plasma.

MST is conducted at $S < 10^7$ which is more than 3 orders below that of a reactor. The most complete study of QSH mode scaling to date from the RFX-Mod device covers slightly more than an order of magnitude in S ($10^6 - 10^7$) and is shown in Figure 86.[16] There is a favorable trend: the normalized strength of the dominant helical mode grows
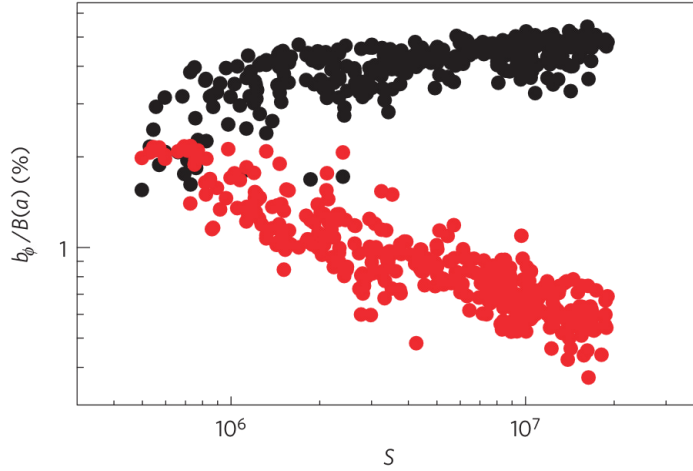
Figure 86: Core-resonant (black) and subdominant (red) $m = 1$ tearing mode amplitudes in RFX-Mod as a function of Lundquist number. Taken from reference [16].

modestly while the secondary modes drop by approximately a factor of 2. Should the trend continue to reactor-level Lundquist number, the fast ion phase-space will be nearly free of subdominant mode-induced orbit losses. With well confined fast ions, the possibility of Alfvénic mode induced resonant transport may become an important factor (negligible in the NBI-heated MST case). Regardless, evaluation of fast ion confinement will be a critical mission of any next-step RFP experiment.

The results in this thesis do not disqualify a helical RFP reactor, but do show a key remaining challenge in fast ion confinement. Measurements herein predict that the helical perturbation will reduce fast ion confinement from classical; diffusivity will increase from scaling as ρ_{fi}^2 to w_{fi}^2. In the limit of negligible subdominant modes, it could very well

be tolerable. The results of this thesis strongly suggest that neoclassical effects from the helical equilibrium will be insignificant. Furthermore, if alpha-driven energetic particle instabilities behave as the fast deuterium driven modes in MST, their effect on global fast ion content is also negligible. These modes cause localized redistribution in the core, but the overall fast ion population is governed by the rate of orbit losses at larger radius.

6.3 Suggestions for Future Work

Since no research project is ever complete, this dissertation will conclude with possible ideas for future studies. In no way is this meant to be a complete and exhaustive list. The effort needed and degree of difficulty varies among the suggestions, but all possess obtainable goals with worthwhile results. Hopefully, these projects may serve as a catalyst for future work and prompt further discoveries and/or ideas.

Fast Ion Loss Measurements

Since a main conclusion of this dissertation is the poor confinement of fast ions in the QSH state, a direct measurement of the losses would provide excellent confirmation. Further development of the FILD is required to perform this measurement, though. The current version suffers from too much electron noise relative to the captured ion signal. Similar work by the heavy ion beam probe (HIBP) group on the MST has achieved great results in the reduction of electron noise in plasma facing ion detectors and could be used as a great reference for the next iteration of the FILD.[161–164] Additionally, if the next FILD design incorporated better pitch resolution, measurements could provide further insight into the nature of tearing-induced stochastic diffusion vs. neoclassical

losses. Since the region outside of the helical core retains the same RFP flux surfaces and magnetic stochasticity, the new FILD design could be implemented in both MH and QSH states. One would have to be careful to minimize the density rise associated with the probe insertion for QSH plasmas.

Collimated Neutron Measurements

Collimated neutron measurements could further support fast ion losses with the added benefit of providing the full fast ion spatial profile. A series of 5 scintillator-PMT detectors and accompanying fast digitizers have recently been loaned to the MST fast ion group from RFX-Mod collaborators.[165] Their fast data acquisition system allows for shot-to-shot pulse-shape discrimination between the gammas and neutrons, overcoming CiNDe's main obstacles. Multiple scintillator-PMT detectors also permits a quicker reconstruction of the fast ion profile without the need to perform a radial scan of the sight lines. Overall, the spatial distribution and its evolution with reference to the helical perturbation strength would provide fruitful information. The spatial fast ion distribution could aid in diffusion and loss calculations, energetic particle driven instability observations, and tearing mode stability studies. Since the detectors would be geometrically fixed, the shift of the magnetic axis and helical phase would have to be taken into account. This complicates the inversion process which usually assumes axisymmetry.

NBI Heating

The effects of the fast ion population on the thermal particle content have never been examined in the helical state. Most notably, the fast ion slowing on the electrons is of particular interest. Most of the data for this dissertation, except for the confinement time measurements, lack Thomson scattering data, unavailable due to an upgrade of the diagnostic, so NBI heating effects could not be included in this work. Recall that, the electrons only retain an appreciable amount of heat from slowing beam ions when operating in an enhanced confinement scheme.[95] The helical RFP, however, establishes a thermal transport barrier that would effectively act as an enhanced confinement operation. A key point of this thesis, however, is that the fast ion confinement becomes very poor. It appears that while thermal confinement limits beam heating in the standard RFP, fast ion confinement may limit heating in the helical RFP. Nevertheless, it would be interesting to see the fast ion heating effects on the electrons as a function of the helical perturbation. Perhaps a "sweet spot" exists where the thermal confinement has improved, relative to the standard RFP, and the fast ion confinement has not yet completely deteriorated. Such an example could possibly arise when Alfvénic instabilities exist in a low-current QSH topology such as that shown in Figure 60.

NBI Counter-Injection

Counter-injection of the neutral beam has never been performed in QSH plasmas. Reversing the plasma current relative to beam injection will strongly impact guiding-center drifts and the alteration of the fast ion safety factor. In the standard RFP, this shifts the fast ion resonances closer together, causing fast ion island overlap, and poor

confinement. While the outcome is not expected to change and the fast ions already experience poor confinement in the helical RFP, this experiment is still worth the effort. At minimum, one could glean the basic confinement properties of the counter-injected ions with measured neutron flux.

Energetic Particle Instability Studies

The $n = 5$ energetic particle driven bursts presented in Chapter 4 have yet to be identified. While they traditionally present themselves as continuum modes in the standard RFP, the structure of the Alfvén continuum shown in Figure 67 strongly suggests the presence of an extremum that could support eigenmodes in the helical RFP. Clearly, the instabilities have a strong frequency response to the changing equilibrium, but their dependence on the altered fast ion population (i.e. beam parameters) is yet to be investigated. This could aid in the comparison between EPMs and AEs. In the past, changes in the Alfvén velocity or fast ion distribution have been performed independently of one another to distinguish between the two flavors of modes.[126] A key assumption, however, was the constancy in the $k_\parallel$ component of the frequency response ($\omega = k_\parallel v_A$). A dataset of approximately the same equilibrium conditions (i.e. $k_\parallel$) can be accumulated by examining the burst behavior during periods of $n = 5$ tearing mode saturation in a scan of plasma current. This would measure across the helical perturbation strength and be repeated for different NBI parameters. The drawback, however, is that a rather large number of shots would be required to cover all beam inputs and $n = 5$ tearing mode strengths.

Additionally, the existence of $n = 4$ energetic particle activity was not heavily examined in this work as well. A cursory, but not extensive, search for $n = 4$ bursts was performed and few were observed to exist in the helical state. A much more thorough examination of the recorded shot database could be performed in an attempt to see if the $n = 4$ activity reacts in a similar manner to the evolving equilibrium as the $n = 5$ bursts. In addition, most of the energetic particle data included interferometry measurements. It may prove worthwhile to compare this dataset to E. Parke's $n = 4$ polarimetry measurements in the standard RFP.[166] Parke compared his polarimetry measurements to the theoretical spatial structure of IAEs and HAEs. Comparing his analysis to any $n = 4$ structures in the helical topology would be very interesting and might provide insight into the mode's identification.

ORBIT Simulations

Mentioned in Chapter 5, the ORBIT calculated diffusivity breaks down with the addition of the subdominant tearing modes. Visible from the fast ion phase-space Poincaré plots, the fast ions quickly become stochastic in the QSH state. The stochasticity has a strong dependence on the presence of the subdominant tearing modes as well. In regards to the diffusivity calculations, the stochasticity follows to the fast ion injection which can overlap with the outer boundary. The problem is relatively straightforward to fix but involves a significant amount of code work. Currently, this is only coded to function with the helical-flux coordinate, χ, and would need to be changed to the geometric coordinates (R,Z). By calculating the diffusivities with the added subdominant modes, other transport mechanisms could be explored such as further estimates of Rechester-Rosenbluth

like transport.

The ORBIT simulations presented in this work only examined the fast ion guiding-center's reaction to the magnetic topology. Simulating the effects of the Alfvénic activity might provide further insight into the fast ion response and/or identifying the energetic particle instabilities themselves. The spatial structures of the $n = 5$ bursts have already been measured in this work via interferometry. MST's polarimetry system could provide complementing measurements of the magentic mode structure, providing a complete picture of the bursting modes. This mode structure could then by simulated by modifying the associated radial magnetic eigenmodes with the measured instability structures. Some amount of interpretation would be required, though, due to measurement error and the rough spatial structure associated with the limited number of interferometry-polarimetry viewing chords. The incorporation of HIBP-measured potential fluctuations may add considerable detail to measurements of the mode structure, though. It's unique in its ability to precisely scan the measurement location across the entire region of interest.

Electrostatics were also not included in the ORBIT simulations. While the associated drift effects should be relatively weak, numerical verification would be ideal. Additionally, ORBIT could provide another tool to study the natural generation of fast ions in the standard RFP via sawtooth crashes.[53, 167, 168] Unfortunately, the subroutines implementing the electrostatic perturbations are non-working on the version of ORBIT installed on MST's servers. Some debugging and alteration of the source code is thereby required to add electrostatic effects.

Lastly, ORBIT requires an axisymmetric equilibrium. Performing particle tracking simulations in the full 3D equilibrium, such as that produced from VMEC/V3Fit, would

provide the best comparison to the actual QSH state. ORBIT3D is another version of the ORBIT code that accepts VMEC equilibria as input. The code is not widely used and supported, though. Most of the features in ORBIT used in this thesis do no exist for ORBIT3D, especially anything that pertains specifically to the RFP. Using either an altered version of ORBIT3D to function with the RFP or another code altogether, fast ion transport simulations in the VMEC equilibria would provide great comparison studies.

Bibliography

[1] W. W. Heidbrink, "Basic physics of Alfven instabilities by energetic particles in toroidally confined plasmas", Phys. Plasmas **15**, 055501 (2008).

[2] R. B. White, R. J. Goldston, M. H. Redi, and R. V. Budny, "Ripple-induced energetic particle loss in tokamaks", Phys. Plasmas **3**, 3043 (1996).

[3] M. H. Redi, H. E. Mynick, M. Suewattana, R. B. White, and M. C. Zarnstorff, "Energetic particle transport in compact quasi-symmetric stellarators", Phys. Plasmas **6**, 3509 (1999).

[4] H. E. Mynick, "transport optimization in stellarators", Phys. Plasmas **13**, 058102 (2006).

[5] P. N. Yushmanov, J. R. Cary, and S. G. Shasharina, "Transport in non-axisymmetric tori with up-down symmetry", Nucl. Fusion **33**, 1293 (1993).

[6] C. D. Beidler, N. G. Hitchon, W. I. van Rij, S. P. Hirshman, and J. L. Shohet, "Unified theory of ripple transport in stellarators", Phys. Rev. Lett. **58**, 1745 (1987).

[7] M. H. Redi, M. Zarnstorff, R. White, R. Budny, A. Janos, D. Owens, J. Schivell, S. Scott, and S. Zweben, "Collisional stochastic ripple diffusion of alpha particles and beam ions on TFTR", Nucl. Fusion **35**, 1191 (1995).

[8] D. Pfefferle, J. P. Graves, W. A. Cooper, C. Misev, I. T. Chapman, M. Turnyanskiy, and S. Sangaroon, "NBI fast ion confinement in the helical core of MAST hybrid-like plasmas", Nucl. Fusion **54**, 064020 (2014).

[9] M. Garcia-Munoz, S. Akaslompolo, P. de Marne, M. G. Dunne, R. Dux, T. E. Evans, N. M. Ferraro, S. Fietz, C. Fuchs, B. Geiger, et al., "Fast-ion losses induced by ELMs and externally applied magnetic perturbations in the ASDEX Upgrade tokamak", Plasma Phys. Control Fusion **55**, 124014 (2013).

[10] J.-K. Park, Y. M. Jeon, J. E. Menard, W. H. Ko, S. G. Lee, Y. S. Bae, M. Joung, K.-I. You, K.-D. Lee, N. Logan, et al., "Rotational resonance of nonaxisymmetric magnetic braking in the KSTAR tokamak", Phys. Rev. Lett. **111**, 095002 (2013).

[11] J. W. Ahn, A. R. Briesemester, M. Kobayashi, J. D. Lore, O. Schmitz, A. Diallo, T. K. Gray, C. J. Lasnier, B. P. LeBlanc, and R. Maingi, "Effect of 3D magnetic perturbations on divertor conditions and detachment in tokamak and stellarator", Plasma Phys. Control Fusion **59**, 084002 (2017).

[12] J.-K. Park, Y. M. Jeon, Y. In, J.-W. Ahn, R. Nazikian, G. Park, J. Kim, H. H. Lee, W. H. Ko, H.-S. Kim, N. C. Logan, et al., "3D field phase-space control in tokamak plasmas", Nature Physics **14**, 1223 (2018).

[13] H. E. Mynick, T. K. Chu, and A. H. Boozer, "Class of model stellarator fields with enhanced confinement", Phys. Rev. Lett. **48**, 322 (1981).

[14] G. Grieger, W. Lotz, P. Merkel, J. Nuhrenberg, J. Sapper, E. Strumberger, H. Wobig, W7-x Team, R. Burhenn, V. Erickmann, et al., "Physics optimization of stellarators", Phys. Fluids B **4**, 2081 (1991).

[15] A. H. Boozer and L. P. Ku, "Control of stellarator properties illustrated by a Wendelstein7-X equilibrium", Phys. Plasmas **18**, 052501 (2011).

[16] R. Lorenzini et al., "Self-organized helical equilibria as a new paradigm for ohmically heated fusion plasmas", Nature Physics **5**, 570 (2009).

[17] P. J. Bonofiglo, J. K. Anderson, M. Gobbin, D. A. Spong, J. Boguski, E. Parke, J. Kim, and J. Egedal, "Fast ion transport in the quasi-single helical reversed-field pinch", Phys. Plasmas **26**, 022502 (2019).

[18] J. Freidberg, *Plasma Physics and Fusion Energy*, 1st ed. (Cambridge University Press, New York, 2007).

[19] P. A. Tipler and R. A. Llewellyn, *Modern Physics*, 5th ed. (W. H. Freeman and Company, New York, 2008).

[20] A. Lepine-Szily and P. Descouvemont, "Nuclear astrophysics: nucleosynthesis in the universe", Int. J. Astrobiol. **11**, 243 (2012).

[21] J. Wesson, *Tokamaks*, 3rd ed. (Oxford University-Press, New York, 2004).

[22] *Fusion_ntau*, (2010) `https : / / en . wikipedia . org / wiki / Lawson \_criterion # /media/File:Fusion_ntau.svg`.

[23] J. M. Pasachoff and A. Filippenko, *The Cosmos: Astronomy in the New Millenium*, 3rd ed. (Thomson Brooks/Cole, California, 2007).

[24] J. Bennett, M. Donahue, N. Schneider, and M. Voit, *Stars, Galaxies, and Cosmology*, 5th ed. (Pearson Education Inc., California, 2009).

[25] L. A. El Guebaly, "Fifty years of magnetic fusion research (1958–2008): brief historical overview and discussion of future trends", Energies **3**, 1067 (2010).

[26] O. A. Hurricane, D. A. Callahan, D. T. Casey, P. M. Celliers, C. Cerjan, E. L. Dewald, T. R. Dittrich, T. Döppner, D. E. Hinkel, L. F. Berzak Hopkins, et al., "Fuel gain exceeding unity in an inertially confined fusion implosion", Nature Physics **506**, 343 (2014).

[27] H. A. B. Bodin and A. A. Newton, "The reversed field pinch", Nucl. Fusion **20**, 1255 (1980).

[28] J. Freidberg, *Ideal Magnetohydrodynamics*, 1st ed. (Plenum Press, New York, 1987).

[29] J. C. Triana, "Measurements of Two-fluid Relaxation in the Madison Symmetric Torus", Ph.D. thesis (Univeristy of Wisconsin - Madison, 2017).

[30]T. M. Biewer, C. B. Forest, J. K. Anderson, G. Fiksel, B. Hudson, S. C. Prager, J. S. Sarff, J. C. Wright, D. L. Brower, W. X. Ding, and S. D. Terry, "Electron heat transport measured in a stochastic magnetic field", Phys. Rev. Lett. **91**, 054004 (2003).

[31]R. N. Dexter, D. W. Kerst, T. W. Lovell, S. C. Prager, and J. C. Sprott, "The Madison Symmetric Torus", Fusion Technology **19**, 131 (1990).

[32]S. Assadi, S. C. Prager, and K. L. Sidikman, "Measurement of nonlinear mode coupling of tearing fluctuations", Phys. Rev. Lett. **69**, 281 (1992).

[33]J. S. Sarff, S. Assadi, A. F. Almagri, M. Cekic, D. J. Den Hartog, G. Fiksel, S. A. Hokin, H. Ji, S. C. Prager, W. Shen, K. L. Sidikman, and M. R. Stoneking, "Nonlinear coupling of tearing fluctuations in the Madison Symmetric Torus", Phys. Fluids B **5**, 2540 (1993).

[34]R. J. Hawryluk, "Poloidal and toroidal programmable power supplies on MST", in 60th Annual Meeting of the APS Division of Plasma Physics Conference (2018).

[35]S. Munaretto, B. E. Chapman, M. D. Nornberg, J. Boguski, A. M. DuBois, A. F. Almagri, and J. S. Sarff, "Effect of resonant magnetic perturbations on three dimensional equilibria in the Madison Symmetric Torus reversed-field pinch", Phys. Plasmas **23**, 056104 (2016).

[36]J. M. Finn, R. Nebel, and C. Bathke, "Single and multiple helicity Ohmic states in reversed-field pinches", Phys. Plasmas **4**, 1262 (1992).

[37]P. Martin, A. Buffa, S. Cappello, F. D'Angelo, D. F. Escande, P. Franz, L. Marrelli, E. Martines, S. Ortolani, G. Spizzo, et al., "Quasi-single helicity states in the reversed field pinch: beyond the standard paradigm", Phys. Plasmas **7**, 1984 (2005).

[38]J. H. Kim and P. W. Terry, "Magnetic turbulence suppression by a helical mode in a cylindrical geometry", Phys. Plasmas **19**, 122304 (2012).

[39]P. W. Terry and G. G. Whelan, "Time-dependent behavior in a transport barrier model for the quasi-single helicity state", Plasma Phys. Control Fusion **56**, 094002 (2014).

[40]R. Paccagnella, "Pressure-driven reconnection and quasi periodical oscillations in plasmas", Phys. Plasmas **21**, 032307 (2014).

[41]I. J. McKinney and P. W. Terry, "Thermal transport dynamics in the quasi-single helicity state", Phys. Plasmas **24**, 062303 (2017).

[42]D. F. Escande, P. Martin, S. Ortolani, A. Buffa, P. Franz, L. Marrelli, E. Martines, G. Spizzo, S. Cappello, A. Murari, R. Pasqualotto, and P. Zanca, "Quasi-single helicity reversed-field pinch plasmas", Phys. Rev. Lett. **85**, 1662 (1999).

[43] L. Marrelli, P. Martin, G. Spizzo, P. Franz, B. E. Chapman, D. Craig, J. S. Sarff, T. M. Biewer, S. C. Prager, and J. C. Reardon, "Quasi-single helicity spectra in the Madison Symmetric Torus", Phys. Plasmas **9**, 2868 (2002).

[44] S. Cappello and D. F. Escande, "Bifurcation in viscoresistive MHD: the Hartmann number and the reversed field pinch", Phys. Rev. Lett. **85**, 3838 (2000).

[45] Y. L. Ho and G. G. Craddock, "Nonlinear dynamics of field maintenance and quasiperiodic relaxation in reversed-field pinches", Phys. Fluids B **3**, 721 (1991).

[46] F. Auriemma, P. Zanca, W. F. Bergerson, B. E. Chapman, W. X. Ding, D. L. Brower, P. Franz, P. Innocente, R. Lorenzini, B. Momo, and D. Terranova, "Magnetic reconstruction of nonaxisymmetric quasi-single-helicity configurations in the Madison Symmetric Torus", Plasma Phys. Control Fusion **53**, 105006 (2011).

[47] D. Bonfiglio, M. Veranda, S. Cappello, D. F. Escande, and L. Chacon, "Experimental-like helical self-organization in reversed-field pinch modeling", Phys. Rev. Lett. **111**, 085002 (2013).

[48] M. Veranda, D. Bonfiglio, S. Cappello, L. Chacon, and D. F. Escande, "Impact of helical boundary conditions on nonlinear 3D magnetohydrodynamic simulations of reversed-field pinch", Plasma Phys. Control Fusion **55**, 074015 (2013).

[49] R. Fridstrom, S. Munaretto, L. Frassinetti, B. E. Chapman, P. R. Brunsell, and J. S. Sarff, "Tearing mode dynamics and locking in the presence of external magnetic perturbations", Phys. Plasmas **23**, 062504 (2010).

[50] A. F. Almagri, S. Assadi, S. C. Prager, J. S. Sarff, and D. W. Kerst, "Locked modes and magnetic field errors in the Madison Symmetric Torus", Phys. Fluids B **4**, 4080 (1992).

[51] D. Craig, *Magnetic Mode Analysis in MST*, tech. rep. (University of Wisconsin - Madison, 2005).

[52] S. Munaretto, B. E. Chapman, D. J. Holly, M. D. Nornberg, R. J. Norval, D. J. Den Hartog, J. A. Goetz, and K. J. McCollam, "Control of 3D equilibria with resonant magnetic perturbations in MST", Plasma Phys. Control Fusion **57**, 104004 (2015).

[53] S. Eilerman, J. K. Anderson, J. A. Reusch, D. Liu, G. Fiksel, S. Polosatkin, and V. Belykh, "Time-resolved ion energy distribution measurements using an advanced neutral particle analyzer on the MST reversed-field pinch", Phys. Plasmas **83**, 10D302 (2012).

[54] J. A. Reusch, J. K. Anderson, V. Belykh, S. Eilerman, D. Liu, G. Fiksel, and S. Polosatkin, "Calibration of an advanced neutral particle analyzer for the Madison Symmetric Torus reversed-field pinch", Rev. Sci. Instrum. **83**, 10D704 (2012).

[55] J. D. Strachan, P. L. Colestock, S. L. Davis, D. Eames, P. C. Efthimion, H. P. Eubank, R. J. Goldston, L. R. Grisham, R. J. Hawryluk, J. C. Hosea, et al., "Fusion neutron production during deuterium neutral-beam injection into the PLT tokamak", Nucl. Fusion **21**, 67 (1981).

[56] W. J. Capecchi, "A Critical Fast Ion Beta in the Madison Symmetric Torus Reversed Field Pinch", Ph.D. thesis (Univeristy of Wisconsin - Madison, 2017).

[57] D. L. Brower, Y. Jiang, W. X. Ding, S. D. Terry, N. E. Lanier, J. K. Anderson, C. B. Forest, and D. Holly, "Multichannel far-infrared polarimeter-interferometer system on the MST reversed field pinch", Phys. Plasmas **72**, 1077 (2001).

[58] I. H. Hutchinson, *Principles of Plasma Diagnostics*, 2nd ed. (Cambridge University Press, New York, 2002).

[59] H. K. Park, "A new asymmetric Abel-inversion method for plasma interferometry in tokamaks", Nucl. Fusion **31**, 2035 (1989).

[60] E. Parke, W. X. Ding, J. Duff, and D. L. Brower, "An upgraded interferometer-polarimeter system for broadband fluctuation measurements", Rev. Sci. Instrum. **87**, 11E115 (2016).

[61] D. S. Darrow, A. Werner, and A. Weller, "Energetic ion loss diagnostic for the Wendelstein 7-AS stellarator", Rev. Sci. Instrum. **72**, 2936 (2001).

[62] D. S. Darrow, S. Baumel, F. E. Cecil, R. Ellis, K. Fullard, K. Hill, A. Horton, V. Kiptily, L. Pedrick, M. Reiche, and A. Werner, "Initial results from the lost alpha diagnostics on Joint European Torus", Rev. Sci. Instrum. **77**, 10E701 (2006).

[63] D. S. Darrow, "Scintillator based energetic ion loss diagnostic for the National Spherical Torus Experiment", Rev. Sci. Instrum. **79**, 023502 (2008).

[64] R. K. Fisher, D. C. Pace, M. Garcia-Munoz, W. W. Heidbrink, C. M. Muscatello, M. A. Van Zeeland, and Y. B. Zhu, "Scintillator-based diagnostic for fast ion loss measurements on DIII-D", Rev. Sci. Instrum. **81**, 10D307 (2010).

[65] D. C. Pace, R. S. Granetz, R. Vieira, A. Bader, J. Bosco, D. S. Darrow, C. Fiore, J. Irby, R. R. Parker, W. Parkin, et al., "Energetic ion loss detector in the Alcator C-Mod tokamak", Rev. Sci. Instrum. **83**, 073501 (2012).

[66] P. J. Bonofiglo, J. K. Anderson, A. F. Almagri, J. Kim, J. Clark, W. Capecchi, S. H. Sears, and J. Egedal, "Development towards a fast ion loss detector for the reversed field pinch", Rev. Sci. Instrum. **87**, 11D824 (2016).

[67] J. Waksman, "Neutral Beam Heating of a Reversed-Field Pinch in the Madison Symmetric Torus", Ph.D. thesis (Univeristy of Wisconsin - Madison, 2013).

[68] T. H. Stix, *Waves in Plasmas*, 1st ed. (American Institute of Physics, New York, 1992).

[69]B. Hudson, "Fast Ion Confinement in the Reversed Field Pinch", Ph.D. thesis (Univeristy of Wisconsin - Madison, 2006).

[70]J. K. Anderson, A. F. Almagri, D. J. Den Hartog, S. Eilerman, C. B. Forest, J. J. Koliner, V. V. Mirnov, L. A. Morton, M. D. Nornberg, E. Parke, et al., "Fast ion confinement and stability in a neutral beam injected reversed field pinch", Phys. Plasmas **20**, 056102 (2013).

[71]R. J. Hawryluk, "An empirical approach to tokamak transport", in Physics of Plasmas Close to Thermonuclear Conditions (1980).

[72]For more details of the TRANSP code, please go to http://w3.pppl.gov/∼pshare/help/transp.htm.

[73]David Hill (Chair) and Richard Hazeltine (Vice Chair), *Report of the FESAC Toroidal Alternates Panel*, `http://fusion.gat.com/tap/final_report.php/`, 2008.

[74]W. W. Heidbrink, J. Kim, and R. J. Groebner, "Comparison of experimental and theoretical fast ion slowing-down times in DIII-D", Nucl. Fusion **28**, 1897 (1988).

[75]D. Liu, "Studies of fast ion confinement in the MST reversed field pinch", in 53rd Annual Meeting of the APS Division of Plasma Physics Conference (2011).

[76]R. B. White and M. S. Chance, "Hamiltonian guiding center drift orbit calculation for plasmas of arbitrary cross section", Phys. Fluids **27**, 2455 (1984).

[77]M. Gobbin, "Numerical study of magnetic topology and test particle transport in the Reversed Field Pinch and in the Tokamak", Ph.D. thesis (Univeristy of Padova, 2008).

[78]R. B. White, G. Spizzo, and M. Gobbin, "Guiding center equations of high accuracy", Plasma Phys. Control Fusion **55**, 115002 (2013).

[79]P. Zanca and D. Terranova, "Reconstruction of the magnetic perturbation in a toroidal reversed field pinch", Plasma Phys. Control Fusion **46**, 1115 (2004).

[80]X. Ma, D. A. Maurer, S. F. Knowlton, M. C. ArchMiller, M. R. Cianciosa, D. A. Ennis, J. D. Hanson, G. J. Hartwell, J. D. Hebert, J. L. Herfindal, et al., "Non-axisymmetric equilibrium reconstruction of a current-carrying stellarator using external magnetic and soft x-ray inversion radius measurements", Phys. Plasmas **22**, 122509 (2015).

[81]W. A. Cooper, J. P. Graves, A. Pochelon, O. Sauter, and L. Villard, "Tokamak magnetohydrodynamic equilibrium states with axisymmetric boundary and a 3D helical core", Phys. Rev. Lett. **105**, 035003 (2010).

[82]M. Gobbin, D. Bonfiglio, A. H. Boozer, A. W. Cooper, D. F. Escande, S. P. Hirshman, J. Lore, R. Lorenzini, L. Marrelli, P. Martin, et al., "Three-dimensional equilibria and transport in RFX-Mod: a description using stellarator tools", Phys. Plasmas **18**, 062605 (2011).

[83]S. P. Hirshman, W. I. van RIJ, and P. Merkel, "Three-dimensional free boundary calculations using a spectral Green's function method", Comput. Phys. Commun. **43**, 143 (1986).

[84]J. D. Hanson, S. P. Hirshman, S. F. Knowlton, L. L. Lao, E. A. Lazarus, and J. M. Shields, "V3FIT: a code for three-dimensional equilibrium reconstruction", Nucl. Fusion **49**, 075031 (2009).

[85]J. J. Koliner, M. R. Cianciosa, J. Boguski, J. K. Anderson, J. D. Hanson, B. E. Chapman, D. L. Brower, D. J. Den Hartog, W. X. Ding, J. R. Duff, et al., "Three dimensional equilibrium solutions for a current-carrying reversed-field pinch plasma with a close-fitting conducting shell", Phys. Plasmas **23**, 032508 (2016).

[86]D. A. Spong, R. Sanchez, and A. Weller, "Shear Alfven continua in stellarators", Phys. Plasmas **10**, 3217 (2003).

[87]A. Salat and J. A. Tataronis, "Shear Alfven mode resonances in nonaxisymmetric toroidal low-pressure plasmas. I. mode equations in arbitrary geometry", Phys. Plasmas **8**, 1200 (2001).

[88]J. D. Callen, *Kinetic Theory and Radiation Processes*, tech. rep. (University of Wisconsin - Madison, 2014).

[89]G. Fiksel, B. Hudson, D. J. Den Hartog, R. M. Magee, R. O'Connell, S. C. Prager, A. D. Beklemishev, V. I. Davydenko, A. A. Ivanov, and Y. Tsidulko, "Observation of weak impact of a stochastic magnetic field on fast-ion confinement", Phys. Rev. Lett. **95**, 125001 (2005).

[90]M. N. Rosenbluth and M. N. Rosenbluth, "Electron heat transport in a tokamak with destroyed magnetic surfaces", Phys. Rev. Lett. **40**, 38 (1978).

[91]M. R. Stoneking, S. A. Hokin, S. C. Prager, G. Fiksel, H. Ji, and D. J. Den Hartog, "Particle transport due to magnetic flucuations", Phys. Rev. Lett. **73**, 549 (1994).

[92]G. Fiksel, S. C. Prager, W. Shen, and M. Stoneking, "Measurement of magnetic fluctuation induced energy transport", Phys. Rev. Lett. **72**, 1028 (1994).

[93]T. Barbui, L. Carraro, D. J. Den Hartog, S. T. A. Kumar, and M. Nornberg, "Impurity transport studies in the Madison Symmetric Torus reversed-field pinch during standard and pulsed poloidal current drive regimes", Plasma Phys. Control Fusion **56**, 075012 (2014).

[94]J. S. Sarff, S. A. Hokin, H. Ji, S. C. Prager, and C. R. Sovinec, "Fluctuation and transport reduction in a reversed field pinch by inductive poloidal current drive", Phys. Rev. Lett. **72**, 3670 (1994).

[95]J. S. Sarff, N. E. Lanier, S. C. Prager, and M. R. Stoneking, "Increased confinement and β by inductive poloidal current drive in the reversed field pinch", Phys. Rev. Lett. **78**, 62 (1997).

[96] M. R. Stoneking, N. E. Lanier, S. C. Prager, J. S. Sarff, and D. Sinitsyn, "Fivefold confinement time increase in the Madison Symmetric Torus using inductive poloidal current drive", Phys. Plasmas **4**, 1632 (1997).

[97] N. E. Lanier, D. Craig, J. K. Anderson, T. M. Biewer, B. E. Chapman, D. J. Den Hartog, C. B. Forest, S. C. Prager, D. L. Brower, and Y. Jiang, "An investigation of density fluctuations and electron transport in the Madison Symmetric Torus reversed-field pinch", Phys. Plasmas **8**, 3402 (2001).

[98] S. T. A. Kumar, D. J. Den Hartog, K. J. Caspary, R. M. Magee, V. V. Mirnov, B. E. Chapman, D. Craig, G. Fiksel, and J. S. Sarff, "Classical impurity ion confinement in a toroidal magnetized fusion plasma", Phys. Rev. Lett. **128**, 125006 (2012).

[99] J. K. Anderson, W. Capecchi, S. Eilerman, J. J. Koliner, M. D. Nornberg, J. A. Reusch, J. S. Sarff, and L. Lin, "Fast ion confinement in the three-dimensional helical reversed-field pinch", Plasma Phys. Control Fusion **56**, 094006 (2014).

[100] E. Parke, J. K. Anderson, D. L. Brower, D. J. Den Hartog, W. X. Ding, C. A. Johnson, and L. Li, "Current profile redistribution driven by neutral beam injection in a reversed-field pinch", Phys. Plasmas **23**, 056108 (2016).

[101] R. Lorenzini, D. Terranova, A. Alfier, P. Innocente, E. Martines, R. Pasqualotto, and P. Zanca, "Single-helical-axis states in reversed-field-pinch plasmas", Phys. Rev. Lett. **10**, 025005 (2008).

[102] D. F. Escande, R. Paccagnella, S. Cappello, C. Marchetto, and F. D'Angelo, "Chaos healing by separatrix disappearance and quasisingle helicity states of the reversed field pinch", Phys. Rev. Lett. **85**, 3169 (2000).

[103] R. Lorenzini, F. Auriemma, A. Fassina, E. Martines, D. Terranova, and F. Sattin, "Internal transport barrier broadening through subdominant mode stabilization in reversed field pinch plasmas", Phys. Rev. Lett. **116**, 185002 (2016).

[104] M. Gobbin, D. Bonfiglio, D. F. Escande, A. Fassina, L. Marrelli, A. Alfier, E. Martines, B. Momo, and D. Terranova, "Vanishing magnetic shear and electron transport barriers in the RFX-Mod reversed field pinch", Phys. Rev. Lett. **106**, 025001 (2011).

[105] D. J. Clayton, B. E. Chapman, R. O'Connell, A. F. Almagri, D. R. Burke, C. B. Forest, J. A. Goetz, M. C. Kaufman, F. Bonomo, P. Franz, M. Gobbin, and P. Piovesan, "Observation of energetic electron confinement in a largely stochastic reversed-field pinch plasma", Phys. Plasmas **17**, 012505 (2010).

[106] I. Predebon, L. Marrelli, R. B. White, and P. Martin, "Particle-transport analysis in reversed field pinch helical states", Phys. Rev. Lett. **14**, 145001 (2004).

[107] M. Gobbin, L. Marrelli, P. Martin, and R. B. White, "Ion and electron local transport inside single helicity islands in the reversed field pinch", Phys. Plasmas **14**, 072305 (2007).

[108]M. Gobbin, L. Marrelli, and R. B. White, "Numerical studies of transport mechanisms in RFX-Mod low magnetic chaos regimes", Plasma Phys. Control Fusion **51**, 056010 (2009).

[109]M. Gobbin, G. Spizzo, L. Marrelli, and R. B. White, "Neoclassical transport in the helical reversed-field pinch", Phys. Rev. Lett. **105**, 195006 (2010).

[110]W. Capecchi, J. K. Anderson, P. J. Bonofiglo, J. Kim, R. M. Magee, R. McConnell, E. Parke, and J. S. Sarff, *A measure of fast ion beta at marginal stability in the Reversed Field Pinch*, Nucl. Fusion (under review).

[111]D. D. Schnack, D. C. Barnes, Z. Mikic, D. S. Harned, and E. J. Caramana, "Semi-implicit magnetohydrodynamic calculations", J. Comput. Phys. **70**, 30 (1987).

[112]G. M. Zaslavskii and B. V. Chirikov, "Stochastic instability of non-linear oscillations", Phys. Uspekhi **14**, 549 (1972).

[113]G. Fiksel, R. D. Bengtson, M. Cekic, D. J. Den Hartog, S. C. Prager, P. Pribyl, J. Sarff, C. Sovinec, M. R. Stoneking, R. J. Taylor, P. W. Terry, G. R. Tynan, and A. J. Wootton, "Measurement of magnetic fluctuation-induced heat transport in tokamaks and RFP", Plasma Phys. Control Fusion **38**, A213 (1996).

[114]A. F. Almagri, J. T. Chapman, C. S. Chiang, D. Craig, D. J. Den Hartog, C. C. Hegna, and S. C. Prager, "Momentum transport and flow damping in the reversed-field pinch plasma", Phys. Plasmas **5**, 3982 (1998).

[115]W. W. Heidbrink and G. J. Sadler, "The behavior of fast ions in tokamak experiments", Nucl. Fusion **34**, 535 (1994).

[116]H. Kimura, Y. Kusama, M. Saigusa, G. J. Kramer, K. Tobita, M. Nemoto, T. Kondoh, T. Nishitani, O. Da Costa, T. Ozeki, et al., "Alfven eigenmode and energetic particle research in JT-60U", Nucl. Fusion **38**, 1303 (1998).

[117]A. de Chambrier, A. D. Cheetham, A. Heym, F. Hofmann, B. Joye, R. Keller, A. Lietti, J. B. Lister, and A. Pochelon, "Alfven wave coupling experiments of the TCA Tokamak", Plasma Phys. **24**, 893 (1982).

[118]W. W. Heidbrink, E. J. Strait, M. S. Chu, and A. D. Turnbull, "Observation of beta-induced Alfven eigenmodes in the DIII-D tokamak", Phys. Rev. Lett. **71**, 855 (1993).

[119]W. W. Heidbrink, E. J. Strait, E. Doyle, G. Sager, and R. T. Snider, "An investigation of beam driven Alfven instabilities in the DIII-D tokamak", Nucl. Fusion **31**, 1635 (1991).

[120]K. L. Wong, R. J. Fonck, S. F. Paul, D. R. Roberts, E. D. Fredrickson, R. Nazikian, H. K. Park, M. Bell, N. L. Bretz, R. Budny, et al., "Excitation of toroidal Alfven eigenmodes in TFTR", Phys. Rev. Lett. **66**, 1874 (1991).

[121] A. Fasoli, J. Lister, S. Sharapov, S. Ali-Arshad, G. Bosia, D. Borba, D. J. Campbell, N. Deliyanakis, J. A. Dobbing, C. Gormezano, et al., "Overview of Alfven eigenmode experiments in JET", Nucl. Fusion **35**, 1485 (1995).

[122] K. Toi, S. Ohdachi, S. Yamamoto, N. Nakajima, S. Sakakibara, K. Y. Watanabe, S. Inagaki, Y. Nagayama, Y. Narushima, H. Yamada, et al., "MHD instabilities and their effects on plasma confinement in Large Helical Device plasmas", Nucl. Fusion **44**, 217 (2004).

[123] J. J. Koliner, "Neutral Beam Excitation of Alfven Continua in the Madison Symmetric Torus Reversed Field Pinch", Ph.D. thesis (Univeristy of Wisconsin - Madison, 2013).

[124] C. Torrence and G. P. Compo, "A practical guide to wavelet analysis", Bull. Amer. Meteor. Soc. **79**, 61 (1998).

[125] E. J. Strait, W. W. Heidbrink, and A. D. Turnbull, "Doppler shift of the TAE mode frequency in DIII-D", Plasma Phys. Control Fusion **36**, 1211 (1994).

[126] J. J. Koliner, C. B. Forest, J. S. Sarff, J. K. Anderson, D. Liu, M. D. Nornberg, J. Waksman, L. Lin, D. L. Brower, W. X. Ding, and D. A. Spong, "Fast-particle-driven Alfvenic modes in a reversed field pinch", Phys. Rev. Lett. **109**, 115003 (2012).

[127] C. R. Cook, "Shear Alfven Continua and Discrete Modes in the Presence of a Magnetic Island", Ph.D. thesis (Univeristy of Wisconsin - Madison, 2015).

[128] C. R. Cook and C. C. Hegna, "Analytical theory of the shear Alfven continuum in the presence of a magnetic island", Phys. Plasmas **22**, 042517 (2015).

[129] A. Biancalani, L. Chen, F. Pegoraro, and F. Zonca, "Shear Alfven wave continuous spectrum within magnetic islands", Phys. Plasmas **17**, 122106 (2010).

[130] C. R. Cook, C. C. Hegna, J. K. Anderson, K. J. McCollam, J. Boguski, R. Feng, J. J. Koliner, D. A. Spong, and S. P. Hirshman, "Identification of island-induced Alfven eigenmodes in a reversed field pinch", Plasma Phys. Control Fusion **58**, 054004 (2016).

[131] L. Lin, W. X. Ding, D. L. Brower, J. J. Koliner, S. Eilerman, J. A. Reusch, J. K. Anderson, M. D. Nornberg, J. S. Sarff, J. Waksman, and D. Liu, "Measurement of energetic-particle-driven core magnetic fluctuations and induced fast ion transport", Phys. Plasmas **20**, 030701 (2013).

[132] L. Lin, J. K. Anderson, D. L. Brower, W. Capecchi, W. X. Ding, S. Eilerman, C. B. Forest, J. J. Koliner, D. Liu, M. D. Nornberg, J. Reusch, and J. S. Sarff, "Energetic-particle-driven instabilities and induced fast-ion transport in a reversed field pinch", Phys. Plasmas **21**, 056104 (2014).

[133] R. M. Magee, J. K. Anderson, S. Korepanov, L. Frausto, J. Boguski, P. J. Bonofiglo, J. Kim, and R. McConnell, "Measuring dynamic fast ion spatial profiles with fusion protons in the Madison Symmetric Torus", Rev. Sci. Instrum. **89**, 10I104 (2018).

[134]R. Betti and J. P. Freidberg, "Stability of Alfven gap modes in burning plasmas", Phys. Fluids B. **4**, 1465 (1992).

[135]R. R. Mett and S. M. Mahajan, "Kinetic theory of toroidicity-induced Alfven eigenmodes", Phys. Fluids B **4**, 2885 (1992).

[136]N. N. Gorelenkov and S. E. Sharapov, "On the collisional damping of TAE-modes on trapped electrons in tokamaks", Phys. Scr. **45**, 163 (1992).

[137]M. N. Rosenbluth, H. L. Berk, J. W. Van Dam, and D. M. Lindberg, "Continuum damping of high-mode-number toroidal Alfven waves", Phys. Rev. Lett. **68**, 596 (1992).

[138]R. Norval, "Plasma Neutral Interaction as an Energy Sink in the MST Edge", Ph.D. thesis (Univeristy of Wisconsin - Madison, 2019).

[139]Z. A. Xing, "Ion thermal transport and heating in reduced tearing RFP plasmas", Ph.D. thesis (Univeristy of Wisconsin - Madison, 2019).

[140]J. Boguski, "Thesis in Preperation", Ph.D. thesis (Univeristy of Wisconsin - Madison, 2019).

[141]F. L. Hinton and R. D. Hazeltine, "Theory of plasma transport in toroidal confinement systems", Rev. Mod. Phys. **48**, 239 (1976).

[142]*From doughnuts to bananas*, (2013) `https://www.euro-fusion.org/news/detail/detail/News/from-doughnuts-to-bananas/`.

[143]R. L. Boivin, S. J. Zweben, and R. B. White, "Study of stochastic toroidal field ripple losses of charged fusion products at the midplane of TFTR", Nucl. Fusion **33**, 449 (1993).

[144]R. C. White, *The Theory of Toroidally Confined Plasmas*, 2nd ed. (Imperial College Press, London, 2006).

[145]J. A. Derr and J. L. Shohet, "Superbanana orbits in stellarator geometries", Phys. Rev. Lett. **43**, 1730 (1979).

[146]A. S. Bishop and C. G. Smith, "Microscopic treatment of classical containment in the stellarator", Phys. Fluids **9**, 1380 (1966).

[147]W. Lotz and J. Nuhrenberg, "Monte Carlo computations of neoclassical transport", Phys. Fluids **31**, 2984 (1988).

[148]D. A. Gates, A. H. Boozer, T. Brown, J. Breslau, D. Curreli, M. Landreman, S. A. Lazerson, J. Lore, H. Mynick, G. H. Neilson, et al., "Recent advances in stellarator optimization", Nucl. Fusion **57**, 126064 (2017).

[149] K. Shinohara, T. Kurki-Suonio, D. Spong, O. Asunta, K. Tani, E. Strumberger, S. Briguglio, T. Koskela, G. Vlad, S. Gunter, G. Kramer, S. Putvinski, K. Hamamatsu, and ITPA Topical Group on Energetic Particles, "Effects of complex symmetry-breakings on alpha particle power loads on first wall structures and equilibrium in ITER", Nucl. Fusion **51** (2011).

[150] J. Egedal, "Drift orbit topology of fast ions in tokamaks", Nucl. Fusion **40**, 1597 (2000).

[151] J. Egedal, M. H. Redi, D. S. Darrow, and S. M. Kaye, "Efficient evaluation of beam ion confinement in spherical tokamaks", Phys. Plasmas **10**, 2372 (2003).

[152] M. A. V. Zeeland, W. W. Heidbrink, R. K. Fisher, M. Garcia Munoz, G. J. Kramer, D. C. Pace, R. B. White, S. Aekaeslompolo, M. E. Austin, J. E. Boom, et al., "Measurements and modeling of Alfven eigenmode induced fast ion transport and loss in DIII-D and ASDEX Upgrade", Phys. Plasmas **18**, 056114 (2011).

[153] J. K. Anderson, C. B. Forest, T. M. Biewer, J. S. Sarff, and J. C. Wright, "Equilibrium reconstruction in the Madison Symmetric Torus reversed field pinch", Nucl. Fusion **44**, 162 (2004).

[154] M. Landreman and P. J. Catto, "Omnigenity as generalized quasisymmetry", Phys. Plasmas **19**, 056103 (2012).

[155] D. Bonfiglio, "Progress in theoretical RFP studies: new stimulated helical regimes and similarities with tokamak and stellarator", in 26th IAEA Fusion Energy Conference (2016).

[156] J. R. Cary and S. G. Shasharina, "Omnigenity and quasihelicity in helical plasma confinement systems", Phys. Plasmas **4**, 3323 (1997).

[157] J. M. Canik, D. T. Anderson, F. S. B. Anderson, K. M. Likin, J. N. Talmadge, and K. Zhai, "Experimental demonstration of improved neoclassical transport with quasihelical symmetry", Phys. Rev. Lett. **98**, 085002 (2007).

[158] J. M. Canik, D. T. Anderson, F. S. B. Anderson, C. Clark, K. M. Likin, J. N. Talmadge, and K. Zhai, "Reduced particle and heat transport with quasisymmetry in the Helically Symmetric Experiment", Phys. Plasmas **14**, 056107 (2007).

[159] M. R. Stoneking, J. T. Chapman, D. J. Den Hartog, S. C. Prager, and J. S. Sarff, "Experimental scaling of fluctuations and confinement with Lundquist number in the reversed-field pinch", Phys. Plasmas **5**, 1004 (1998).

[160] D. Terranova, T. Bolzonella, S. Cappello, P. Innocente, L. Marrelli, and R. Pasqualotto, "Study of the scaling of magnetic fluctuations in the RFX reversed field pinch", Plasma Phys. Control Fusion **42**, 843 (2000).

[161] P. J. Fimognari, D. R. Demers, X. Chen, and P. M. Schoch, "Resolving small signal measurements in experimental plasma environments using calibrated subtraction of noise signals", Rev. Sci. Instrum. **85**, 11D849 (2014).

[162] P. J. Fimognari, T. P. Crowley, and D. R. Demers, "Development of a beam ion velocity detector for the heavy ion beam probe", Rev. Sci. Instrum. **87**, 11D414 (2016).

[163] T. P. Crowley, D. R. Demers, and P. J. Fimognari, "Control of secondary electrons from ion beam impact using a positive potential electrode", Rev. Sci. Instrum. **87**, 11D418 (2016).

[164] P. J. Fimognari, T. P. Crowley, D. R. Demers, and T. D. Kile, "Noise mitigation methods for ion detectors operating with a direct view of high temperature plasmas", Rev. Sci. Instrum. **89**, 10I108 (2018).

[165] M. Zuin, "Neutron and gamma-ray detection in reversed-field pinch deuterium plasmas in the RFX-Mod device", in 56th Annual Meeting of the APS Division of Plasma Physics Conference (2014).

[166] E. Parke, "Measurement of beam-driven Alfvenic instabilities in MST and comparison to predictions", in 59th Annual Meeting of the APS Division of Plasma Physics Conference (1980).

[167] S. Eilerman, "Ion Runaway During Magnetic Reconnection in the Reversed-Field Pinch", Ph.D. thesis (Univeristy of Wisconsin - Madison, 2014).

[168] J. K. Anderson, J. Kim, P. J. Bonofiglo, W. Capecchi, S. Eilerman, M. D. Nornberg, J. S. Sarff, and S. H. Sears, "Dynamics of a reconnection-driven runaway ion tail in a reversed field pinch plasma", Phys. Plasmas **23**, 055702 (2016).